

---

# High Frequency Cluster Radio Galaxies and the Sunyaev-Zel'dovich Effect Properties of Galaxy Clusters

Nikhel Gupta

---



Munich 2018



---

# **High Frequency Cluster Radio Galaxies and the Sunyaev-Zel'dovich Effect Properties of Galaxy Clusters**

**Nikhel Gupta**

---

Dissertation  
an der Faculty of Physics  
der Ludwig-Maximilians-Universität  
München

vorgelegt von  
Nikhel Gupta  
aus Pathankot, India

München, den 26. Januar 2018

Erstgutachter: Prof. Dr. Joseph Mohr

Zweitgutachter: Prof. Dr. Eiichiro Komatsu

Tag der mündlichen Prüfung: 2. März 2018

# Contents

<b>Zusammenfassung</b>	<b>xvii</b>
<b>Abstract</b>	<b>xviii</b>
<b>1 Introduction</b>	<b>1</b>
1.1 Cosmological Framework . . . . .	1
1.1.1 Friedman Robertson Walker Models . . . . .	1
1.1.2 Distance and Volume Measures . . . . .	4
1.1.3 Thermal History of Universe . . . . .	5
1.1.4 Structure Formation . . . . .	7
1.2 Galaxy Clusters . . . . .	10
1.2.1 Multiwavelength Observations of Galaxy Clusters . . . . .	10
1.2.2 Cluster Cosmology . . . . .	16
1.3 Thesis Motivation and Outlook . . . . .	19
<b>2 High Frequency Cluster Radio Galaxies</b>	<b>21</b>
2.1 Abstract . . . . .	22
2.2 Introduction . . . . .	22
2.3 Data and Radio Galaxy Flux Corrections . . . . .	23
2.3.1 SPT Observations . . . . .	24
2.3.2 SUMSS Catalog . . . . .	24
2.3.3 MCXC Catalog . . . . .	25
2.3.4 Catalog of Cluster Radio Galaxy Candidates . . . . .	26
2.3.5 Radio Galaxy Spectral Indices . . . . .	29
2.4 Results . . . . .	31
2.4.1 Radial Distribution of Cluster Radio Galaxies . . . . .	31
2.4.2 Cluster Radio Galaxy Luminosity Functions . . . . .	33
2.5 Radio Galaxy Contamination of Cluster SZE . . . . .	39
2.5.1 Characteristic Levels of Contamination . . . . .	39
2.5.2 Incompleteness of SPT-Like Cluster Sample . . . . .	42
2.5.3 Impact on $\zeta - M_{500}$ Scaling Relation . . . . .	44
2.5.4 Redshift Evolution of the Luminosity Function . . . . .	44
2.6 Systematics . . . . .	46

2.6.1	MCXC Cluster Mass Uncertainties . . . . .	46
2.6.2	Radio Galaxy Flux Uncertainties . . . . .	47
2.7	Conclusions . . . . .	47
<b>3</b>	<b>Redshift and Mass Trends in Cluster Radio Galaxies</b>	<b>51</b>
3.1	Abstract . . . . .	51
3.2	Introduction . . . . .	52
3.3	Data and Radio Galaxy Flux Corrections . . . . .	53
3.3.1	SPT Observations . . . . .	53
3.3.2	SUMSS Catalog . . . . .	53
3.3.3	DES-Y1 redMaPPer Catalog . . . . .	54
3.3.4	Radio Galaxy Catalog at SPT Frequencies . . . . .	55
3.4	Cluster Radio Galaxy Populations . . . . .	58
3.4.1	Radial Distribution of Cluster Radio Galaxies . . . . .	58
3.4.2	Redshift trends for Radio Galaxy Luminosity Functions . . . . .	59
3.4.3	Halo Occupation Number . . . . .	64
3.5	Radio Galaxy Contamination of Cluster SZE . . . . .	66
3.5.1	Incompleteness in SPT-SZ like Survey . . . . .	66
3.5.2	Bias in Scaling Relation Parameters . . . . .	68
3.6	Conclusions . . . . .	68
<b>4</b>	<b>SZE Observables, Pressure Profiles and Center Offsets</b>	<b>71</b>
4.1	Abstract . . . . .	71
4.2	Introduction . . . . .	72
4.3	Simulation . . . . .	74
4.3.1	Simulation Method . . . . .	74
4.3.2	Compton- $y$ Map . . . . .	76
4.3.3	Cluster Catalog . . . . .	77
4.4	Pressure Profile . . . . .	77
4.4.1	Pressure Profiles from the Simulations . . . . .	78
4.4.2	Effective Pressure $P_{\text{eff}}$ Assuming hydrostatic equilibrium (HSE) . . . . .	85
4.5	SZE Observable-Mass Relation . . . . .	88
4.5.1	Spherical $Y_{\text{sph},\Delta} - M_{\Delta}$ Relation . . . . .	88
4.5.2	Cylindrical $Y_{\text{cyl}} - M_{500c}$ Relation . . . . .	90
4.5.3	Light Cone $Y_{\text{lc}} - M_{500c}$ Relation . . . . .	91
4.5.4	Scatter about the $Y$ - $M$ Relations . . . . .	95
4.6	SZE Center Offsets . . . . .	96
4.7	Conclusions . . . . .	98
4.8	Additional pressure profile modeling . . . . .	100
4.9	Additional offset modeling . . . . .	104
	<b>Conclusions</b>	<b>107</b>





# List of Figures

1.1	The angular diameter ( $D_A$ ) and luminosity ( $D_L$ ) distances as a function of redshift. The plot is constructed using the flat cosmology with $\Omega_M = 0.3$ and $H_0 = 70 \text{ Km s}^{-1} \text{ Mpc}^{-1}$ . . . . .	4
1.2	Systematic picture of the expansion of Universe with time, temperature and energy specified in seconds, Kelvin and GeV, respectively. The information about various particles produced at different cosmic times is shown in the bottom left. The beginning of Universe started with a Big Bang followed by a brief period of inflation. At various energies, particles like protons, neutrons, electrons, positrons and neutrinos were formed and were coupled to the radiation until the era of recombination when Universe became transparent and the CMB started to propagate freely towards us. This is followed by dark ages and then re-ionization when the first stars were formed in the Universe. The tiny fluctuations in the density fields resulted in the structure that we see today shown as the stars and galaxies in the right end of the figure. Credit: Particle Data Group, LBNL. . . . .	6
1.3	The growth of dark matter (purple), baryon (green) and radiation (red) perturbations in radiation and matter dominated eras of Universe. The perturbations before entering the horizon grow similarly for all these components in radiation dominated era. After they enter the horizon, the dark matter perturbations stop to grow and baryon-photon fluid starts oscillating together. In matter dominated era, dark matter perturbations grow with scale factor while baryon-photon fluid keeps oscillating until the recombination. At recombination photons free stream and baryonic perturbations start growing with scale factor. . . . .	8
1.4	The multi-wavelength observations of Abell 1835 galaxy cluster ( $z \sim 0.25$ ) from left to right: in optical with Hubble space telescope 3.18' view (credit: NASA/STScI/WikiSky), in X-ray using <i>Chandra</i> 0.7 keV to 7.0 keV image smoothed with a 1.5'' Gaussian (Korngut et al., 2011) and in radio using MUSTANG SZE image smoothed to 18'' resolution (Korngut et al., 2011). . . . .	10

- 1.5 The match filtered mm-wavelength map of 50 deg<sup>2</sup> of SPT region showing the CMB sky. Three high signal to noise galaxy clusters are shown as black spots in contrast to the CMB in the bottom-right of map. In the bottom-left two point sources (an AGN and a dusty galaxy) are shown as shining white spots in the radio sky. Credit: SPT collaboration. . . . . 13
- 1.6 X-ray and SZE selected cluster samples: The estimated mass versus redshift for the 516 optically confirmed clusters from the SPT catalog (Bleem et al., 2015), 91 clusters from the ACT survey (Marriage et al., 2011; Hasselfield et al., 2013), 809 clusters from the Planck survey (Planck Collaboration et al., 2013a), and 740 X-ray clusters selected from the ROSAT all-sky survey (Piffaretti et al., 2011). While the SPT data provides a nearly mass-limited sample, the cluster samples selected from ROSAT and Planck data are redshift-dependent owing to cosmological dimming of X-ray emission and the dilution of the SZ signal by the large Planck beams, respectively. Credit: Bleem et al. (2015). . . . . 15
- 1.7 Left panel: Cosmological constraints at  $1 - \sigma$  and  $2 - \sigma$  levels in the plane of  $\Omega_m$  and  $\sigma_8$  from Planck CMB TT, TE, EE+lowP datasets (dashed contours) and their comparison with constraints from cluster number counts. Right panel: Comparison of the constraints on mass bias  $1 - b$  from cluster and primary CMB constraints. The solid black curve shows the posterior for the mass bias when SZE cluster and CMB datasets are combined. Credit: Planck Collaboration et al. (2015a). . . . . 18
- 2.1 Distribution of offsets between SUMSS and SPT point sources in units of the total positional uncertainty  $\sigma_P$ . Lines represent best fit level of random associations (green), Gaussian core (blue) and core plus random (orange). We limit matches to lie within  $5\sigma_P$  and estimate only 3 percent of those are random associations. . . . . 26
- 2.2 SPT 150 GHz flux versus cluster redshift (bottom) and mass (top) for SUMSS selected radio galaxies with  $S_{150} > 6$  mJy that lie in the projected  $\theta_{200}$  regions of clusters from the MCXC X-ray selected cluster catalog. Green (brown) points show fluxes before (after) SZE flux corrections. The SZE flux correction, in general, is larger for high mass and distant clusters compared to the low mass and nearby clusters, ranging between 0 and 24 mJy. Seven radio galaxies that would not have made the SPT flux cut because of the SZE flux bias from their host galaxy clusters are marked with stars. . . . . 28
- 2.3 Surface density profiles for two flux limited  $S_{150} > 6$  mJy samples of radio galaxies stacked within 139 MCXC clusters. Both samples with SZE flux corrections (red) and without (blue) are shown. The lines are the best fit NFW models (see Table 3.1). . . . . 31

- 2.4 The 150 GHz LF for sources within  $\theta_{200}$  of the centers of massive galaxy clusters. This LF is derived from the SUMSS selected sample in the SPT region with (red) and without (blue) SZE flux corrections. Lines are the best fitting LF models. The increase in LF amplitude on the high luminosity end when using the SZE flux bias corrected sample is clear. For convenience in this figure the bins containing negative values in the background subtracted counts are represented as points at the bottom of the figure. . . . . 35
- 2.5 Cluster Radio Galaxy LFs: The SUMSS based 150 GHz LF (top), which includes SZE flux bias corrections, and the SUMSS 843 MHz LF (bottom), which is constructed using MCXC clusters over the full 8100 deg<sup>2</sup> SUMSS survey region. The datasets are fitted with the AGN component of the LF by varying  $y_1$  and  $x_1$  parameters as discussed in section 3.4.2. The data points are shifted horizontally to improve visibility. Different lines indicate the best fit model LFs (see Table 2.3). In both plots, we divide the samples into two different redshift bins. However, the data are not enough to provide meaningful constraints on the redshift evolution for the 150 GHz LF. For convenience in this figure the bins containing negative values in the background subtracted counts are represented as points at the bottom of the figure. . . . . 37
- 2.6 LF fits to samples at different observing frequencies. As explained in section 3.4.2 the fit is done using an AGN fitting function (Condon et al., 2002). The filled regions show the best fit model and the  $1\sigma$  confidence regions (see Table 2.3). The curves show the decrease in the cluster radio galaxy population with increasing frequency and increasing power, and – in the 150 GHz case – the impact of the SZE flux bias correction. . . . . 38
- 2.7 Fraction of clusters contaminated above a degree of contamination  $s \geq 0.1$  for clusters as a function of mass  $M_{500}$  and redshift at 150 GHz (top panel). This shows that there is a higher probability of missing the detection of low redshift and low mass clusters. Bottom panel shows the fraction of clusters (with  $M_{500} = 3 \times 10^{14} M_{\odot}$  and  $z = 0.25$ ) above a given degree of contamination  $s$  at 95 and 150 GHz. The contamination is larger at 95 GHz, both because of the smaller SZE signature and the higher AGN fluxes at this frequency as compared to that at 150 GHz. . . . . 40
- 2.8 The estimated decrease in the observed number of galaxy clusters ( $N_{\text{Obs}}$ ) due to the point source contamination as compared to the theoretical number counts ( $N$ ) for 2500 deg<sup>2</sup> of the SPT survey with  $\xi_r \geq 4.5$ . The decrease in the observed number of clusters ( $N_{\text{Obs},z}$ ) is also shown for a possible redshift evolution of the form  $(1+z)^{2.5}$  in the number of point sources. . . . . 45
- 3.1 Distribution of redMaPPer DES-Y1 galaxy clusters as a function of mass and redshift. The color bar represents the number of clusters. The median mass and redshift of the sample is  $1.8 \times 10^{14} M_{\odot}$  and 0.46, respectively. . . 55

3.2	Radial distribution of radio sources observed at 0.843, 95, 150 and 220 GHz in the direction of redMaPPer DES-Y1 galaxy clusters. The lines are the best fit projected NFW models (see Table 3.1). At 220 GHz, the data is not enough to constrain the projected NFW profile. . . . .	57
3.3	Cluster Radio Galaxy LFs: Upper panel shows the SUMSS based 843 MHz LF, which is constructed using DES-Y1 redMaPPer galaxy clusters. The uncertainties are represented by Poisson errors here. The datasets are fitted with the LF model by varying $y$ , $x$ and $\gamma$ (density or luminosity evolution) parameters as discussed in section 3.4.2. Different lines indicate the best fit model LFs (see Table 3.2). Lower panel shows the ratio between the data points and the best fit model for first redshift bin, representing the change in the shape of LFs. We divide the samples into three different redshift bins. For convenience in this figure the bins containing negative values in the background subtracted counts are represented as points at the bottom of the figure. We show the data, best fit model and model uncertainties from Gupta et al. (2017a) in pink here. . . . .	59
3.4	Same as Fig. 3.3 but for 95 GHz observed SUMSS selected radio sources. .	60
3.5	Same as Fig. 3.3 but for 150 GHz observed SUMSS selected radio sources.	60
3.6	Same as Fig. 3.3 but for 220 GHz observed SUMSS selected radio sources. The data is not enough to provide meaningful constraints on the redshift evolution for the 220 GHz LF, thus we do not plot the ratio between the data points and best fit model as well. . . . .	61
3.7	HONs: Number of radio sources observed at 0.843, 95, 150 and 220 GHz per unit number of galaxy clusters. The dashed lines are the best fit power law models and shaded regions show $1-\sigma$ model uncertainties (see Table 3.3). The redshift dependence is marginalized here by multiplying the number of radio galaxies by $(1+z)^{-\gamma_D}$ , where $\gamma_D$ is the density evolution presented in Table 3.3 for different frequencies. . . . .	65
3.8	The estimated decrease in the observed number of galaxy clusters ( $N_{\text{Obs},z}$ ) due to the point source contamination as compared to the theoretical number counts ( $N$ ) for 2500 deg <sup>2</sup> of the SPT survey with $\xi_r \geq 5$ . The shaded green region in the lower panel shows the $1-\sigma$ model uncertainties. . . . .	68
4.1	Compton-y map from simulation . . . . .	75
4.2	The individual pressure profiles . . . . .	80
4.3	The pressure profile trends . . . . .	81
4.4	The pressure profile comparison . . . . .	83
4.5	Hydrostatic equilibrium pressure comparison . . . . .	85
4.6	$Y_{\text{lc}}$ -Mass relation . . . . .	92
4.7	Impacts of light cone on $Y$ . . . . .	92
4.8	$Y_{\text{sz}}$ residual distribution . . . . .	94

---

4.9	The distributions of central offsets between the gravitational center and the peak of the $Y_{SZE}$ signal for clusters in redshift slices (top panels) and light cones (bottom panels). The yellow and green circles mark the 68 <sup>th</sup> and 95 <sup>th</sup> percentiles of the distribution, respectively. Radial offset distributions are also shown where the red line describes the double Rayleigh fit to these distributions. The fits indicate that about 80 percent of clusters populate the narrow first component with $\sigma(\Delta r/R_{500c}) \sim 0.045$ and the remainder populate the wider component with $\sigma \sim 0.16$ (see Table 4.5). . . . .	94
4.10	The best fit parameters of the double Rayleigh function in equation (4.12) that model the radial offset distribution of the light cones for different cluster subsamples. While the fraction of large offset or disturbed clusters remains at $\sim 20$ percent for all subsamples and the characteristic offset of this sample is $\sim 0.18R_{500c}$ , the characteristic offset for the more relaxed subset is larger for lower mass systems and grows with redshift. . . . .	97
4.11	Constraints on the pressure profile . . . . .	101
4.12	The pressure profile trends . . . . .	102
4.13	Offset trends showing the consistency of the parameters with mass and redshift. . . . .	103



# List of Tables

2.1	The characteristic spectral indices and $1\sigma$ uncertainties for all SUMSS detected sources in the SPT region and a subset of these, which we denote as BCGs, that lie within $0.1 \times \theta_{200}$ of the MCXC cluster centers. Mean spectral indices are presented for pairs of frequencies constructed from 150 GHz, 95 GHz and 843 MHz. The SZE correction is applied at 95 and 150 GHz. . . . .	30
2.2	Best fit NFW model parameters for the radial profile of radio galaxies with $S_{150} \geq 6$ mJy in a stack of 139 MCXC clusters. The samples with uncorrected and SZE corrected fluxes are shown, and for each we present concentration $c$ , $N_{200}$ , background density $\Sigma_B$ , and the number of sources $\bar{N}_T$ within $\theta_{200}$ . . . . .	33
2.3	The best fit LF parameters for different samples of cluster radio galaxies. The samples of SPT fluxes at SUMSS locations (“SUMSS in SPT”) are corrected for the SZE flux bias at 95 and 150 GHz, except for “SUMSS in SPT (U)”, which denotes the sample with uncorrected fluxes. . . . .	36
3.1	Best fit projected NFW model parameters for the radial profile of radio galaxies above a flux cut (see section 3.3.4) in a stack of 7063 redMaPPer DES-Y1 galaxy clusters. The samples at 0.843, 95 and 220 GHz are shown, and for each we present concentration $c$ , the estimate of the total sample of radio galaxies within $R_{200}$ in our sample $\sum_{cl} N_{200}$ and the background density of radio galaxies $\Sigma_B$ within $\theta_{200c}$ . . . . .	57
3.2	The best fit LF parameters for different samples of cluster radio galaxies. The samples with SPT fluxes at SUMSS locations are corrected for the SZE flux bias at 95 and 150 GHz. $\gamma_D$ and $\gamma_P$ are defined as the density and luminosity redshift evolution parameters, respectively. . . . .	61
3.3	Best fit normalization $A_H$ and slope $B_H$ of the power law at 0.843, 95 and 150 GHz (see section 3.4.3). . . . .	64
4.1	<i>Magneticum</i> simulation box . . . . .	74
4.2	Constraints on GNFw Pressure Profile . . . . .	78
4.3	Ysz-mass relations in spherical case . . . . .	89
4.4	Ysz-mass relations with projection. . . . .	90

---

4.5	The best fit parameters of the double Rayleigh function (see equation 4.12) fit to the radial offset distribution between the gravitational potential center and the $Y_{\text{SZE}}$ peak for clusters in the redshift slices and in the light cones. In the last column we compare these numbers from an observational study by Saro et al. (2015). . . . .	98
4.6	Constraints on e-GNFW Pressure Profile . . . . .	104
4.7	The best fit parameters of the extended double Rayleigh function (see equation (4.15)) fit to the radial offset distribution between the gravitational potential center and the $Y_{\text{SZE}}$ peak for clusters in the in the light cones for a revised model. . . . .	104

# Zusammenfassung

Die Hochfrequenz-Millimeterwellen Durchmusterungen durch das South Pole Telescope (SPT), das Atacama Cosmology Telescope (ACT) und der ESA Satellitenmission Planck ermöglichen die Sunyaev-Zeldovitch-Effekt-Detektion (SZE) grosser Galaxienhaufenkataloge und deren Nutzung zur Bestimmung der kosmologischen Parameter. Das Verhältnis des SZE Signals zur zugrundeliegenden Halonenmasses des Galaxienhaufens - die sogenannte mass-observable relation - ist von zentraler Bedeutung für diese Untersuchungen. Die Bestimmung der kosmologischen Parameter ist insbesondere stark von der Annahme des hydrostatischen Gleichgewichts (hydrostatic equilibrium, HSE) abhängig. Mit Hilfe der hydrodynamischen Magneticum Pathfinder Simulationen bestimmen wir anhand eines simulierten Galaxienhaufenkataloges die Abhängigkeit des Druckprofils von der Halonenmasse und der Rotverschiebung des Haufens. Wir weisen nach, dass der thermische Druck nur 80% neben der mass-observable relation hängt die Bestimmung der kosmologischen Parameter durch Galaxienhaufenkataloge auch von der Selektion der Kataloge ab. Insbesondere kann die Anwesenheit von punktförmigen Radioquellen in einem Galaxienhaufen zu einer Verringerung des SZE Signals, und folglich einer Nichtdetektion, führen. Um den Einfluss dieses Effekts auf die Anzahl Haufen im SPT-Katalog zu bestimmen, untersuchen wir die Häufigkeit von punktförmigen Radioquellen in einem Röntgen- und einem optisch selektiertem Haufenkatalog. Wir bestimmen die Leuchtkraftverteilung (luminosity function) der Radioquellen, und untersuchen dessen Entwicklung mit Rotverschiebung. Die daraus folgende Anzahl nichtdetektierter Quellen ist kleiner als der Poissonfehler auf der Anzahl Haufen im SPT-Katalog, und führt somit zu keiner signifikanten Fehlbestimmung der kosmologischen Parameter. Zusammenfassend stellen wir fest, dass die Galaxienhaufenselektion durch den SZE Effekt eine ausreichende Vollständigkeit der Kataloge sicherstellt. Die Annahme von HSE führt jedoch zu einer 20-prozentigen Fehlschätzung der Halonenmassen der Haufen. Anhand unserer Arbeit kann diese Fehlschätzung kalibriert und korrigiert werden.



# Abstract

The high frequency mm-wave surveys by the South Pole Telescope (SPT), the Atacama Cosmology Telescope (ACT), and Planck have enabled the Sunyaev-Zel'dovich Effect (SZE) detection of large cluster samples and their use to constrain cosmological parameters. In these analyses the connection between the cluster SZE signature and the underlying halo mass – described by the so-called observable-mass relation – plays a central role. A calibration of this relation requires robust masses determined through the use of galaxy dynamics or weak gravitational lensing, whose biases can be calibrated using current structure formation simulations. Groups like the Planck collaboration that have attempted to employ masses derived using the assumption of Hydro-static Equilibrium (HSE) have found that their cosmological constraints are limited by the inaccuracy of this assumption. The cluster cosmology is also highly dependent on an understanding of the selection function, which in the SZE case can be impacted by radio emission from Active Galactic Nuclei (AGN) within the clusters. Although the high frequency SZE surveys listed above are working in a regime where radio AGN with sufficient flux to impact the SZE signature are rare, it is nevertheless important to study the luminosity functions of these cluster radio AGN to constrain their impact on incompleteness in SZE selected cluster samples.

To begin with, we study the overdensity of point sources in the direction of X-ray-selected galaxy clusters from the Meta-Catalog of X-ray detected Clusters of galaxies (MCXC;  $\langle z \rangle = 0.14$ ) at SPT and Sydney University Molonglo Sky Survey (SUMSS) frequencies. Flux densities at 95, 150 and 220 GHz are extracted from the 2500 deg<sup>2</sup> SPT-SZ survey maps at the locations of SUMSS sources, producing a multi-frequency catalog of radio galaxies. In the direction of massive galaxy clusters, the radio galaxy flux densities at 95 and 150 GHz are biased low by the cluster SZE signal, which is negative at these frequencies. We employ a cluster SZE model to remove the expected flux bias and then study these corrected source catalogs. We find that the high frequency radio galaxies are centrally concentrated within the clusters and that their luminosity functions (LFs) exhibit amplitudes that are characteristically an order of magnitude lower than the cluster LF at 843 MHz. We use the 150 GHz LF to estimate the impact of cluster radio galaxies on an SPT-SZ like survey. The radio galaxy flux typically produces a small bias on the SZE signal and has negligible impact on the observed scatter in the SZE mass-observable relation. If we assume there is no redshift evolution in the radio galaxy LF then  $1.8 \pm 0.7$  percent of the clusters with detection significance  $\xi \geq 4.5$  would be lost from the sample. We note that with the MCXC sample we cannot place strong constraints on the redshift evolution

of the high frequency radio galaxy LF.

The most recent catalog of galaxy clusters for this purpose is constructed from the Dark Energy Survey first year observations (DES-Y1). Thus, we study the redshift and mass trends for the radio sources in the direction of optically selected catalog of galaxy clusters from DES. We measure luminosity functions (LFs) and Halo Occupation Numbers (HONs) for these radio sources by statistically correcting for the background population and effectively placing the radio sources at the redshift of clusters for all frequencies. We find that the number of sources depend on the cluster mass as  $N \propto M^{B_H}$  with  $B_H = 0.83 \pm 0.05$ ,  $0.92 \pm 0.25$  and  $1.23 \pm 0.15$  for 0.843, 95 and 150 GHz datasets, respectively. The pure density evolution in LFs is estimated as  $(1+z)^{\gamma_D}$ , with power index  $\gamma_D = 2.32^{+0.40}_{-0.41}$ ,  $6.68^{+3.25}_{-3.54}$  and  $6.26^{+2.60}_{-2.77}$  at 0.843, 95 and 150 GHz, respectively. We repeat our exercise to estimate the sample incompleteness and bias in the observable-mass relation for 2500 deg<sup>2</sup> of SPT-SZ like survey. We find that  $10.7 \pm 2.4$  percent of the clusters would be lost from the cluster sample with detection significance  $\xi \geq 5$  and redshift range  $0.25 < z < 1.55$  due to radio source contamination. We are exploring the impact of the incompleteness on the cosmological parameters, and we expect that there could be some super-statistical shift in the best fit parameters, because the Poisson noise on the full cluster sample in the latest analysis is at the 5 percent level. We also explore the impact of the radio galaxy contamination on the observable-mass relation, finding that the shift in the parameters of the relation is well within the statistical uncertainties derived for these parameters in the most recent cosmological analysis; thus, it is not an important systematic for cosmological parameter estimation using cluster abundance. Moreover, in our cluster cosmology analysis approach we empirically calibrate the observable-mass relation, and therefore our approach is insensitive to this effect.

In the past few years a lot of attention is offered towards investigations of the galaxy cluster observable-mass scaling relations. One method is to measure the mass from X-ray observations of the ICM combined with the assumption of HSE and to calibrate the observable-mass relation using these HSE masses. However, given that galaxy clusters are young objects still actively growing through accretion, it is unlikely that HSE pertains in these systems – particularly those systems having undergone recent major mergers. Thus, using these masses will produce misleading conclusions about the observable-mass scaling relation. It is important to quantify these systematics in the framework where true mass of cluster is known. We present a detailed study of the galaxy cluster thermal SZE signal  $Y$  and pressure profiles using *Magneticum* Pathfinder hydrodynamical simulations. With a sample of 50,000 galaxy clusters ( $M_{500c} > 1.4 \times 10^{14} M_\odot$ ) out to  $z = 2$ , we find significant variations in the shape of the pressure profile with mass and redshift and present a new generalized NFW model that follows these trends. We show that the thermal pressure at  $R_{500c}$  accounts for only 80 percent of the pressure required to maintain hydrostatic equilibrium, and therefore even idealized hydrostatic mass estimates would be biased at the 20 percent level. We compare the cluster SZE signal extracted from a sphere with different virial-like radii, a virial cylinder within a narrow redshift slice and the full light cone, confirming small scatter ( $\sigma_{\ln Y} \simeq 0.087$ ) in the sphere and showing that structure immediately surrounding clusters increases the scatter and strengthens non self-similar

redshift evolution in the cylinder. Uncorrelated large scale structure along the line of sight leads to an increase in the SZE signal and scatter that is more pronounced for low mass clusters, resulting in non self-similar trends in both mass and redshift and a mass dependent scatter that is  $\sim 0.16$  at low masses. The scatter distribution is consistent with log-normal in all cases. We present a model of the offsets between the center of the gravitational potential and the SZE center that follows the variations with cluster mass and redshift.



# Chapter 1

## Introduction

This research work is dedicated to the study of galaxy clusters using observations and simulations of Universe. The main focus of this work is to study the impact of the structural properties of galaxy clusters on cluster cosmology. In the first part of the thesis, a population of high frequency cluster radio galaxies is investigated using multi-wavelength observations of galaxy clusters and in the second part, pressure profiles and mass-observable relations are studied in the framework of large hydrodynamical simulations. In this chapter, I present an overview of the standard model of Cosmology and a comprehensive description of the galaxy clusters.

### 1.1 Cosmological Framework

Cosmology is an empirical science of the Universe that describes its past, current and future state using the known physical laws and different independent observations. We have one Universe that we can observe which makes Cosmology a unique science such that the laws of physics can only be tested in one framework. Universe is governed by the two long range fundamental forces i.e gravity and electromagnetic radiation. The structure formation in Universe is a result of gravitational interaction between the visible (baryonic) and non visible (dark) matter in the Universe, where the latter forms a major part of the energy density of Universe. Almost all information that we gather from observations is in the form of electromagnetic radiation and is from the past of the Universe due to the finite speed of speed ( $c$ ). The information that we receive today from a source which is at a distance  $D$  away from us tells us the state of the source when its intrinsic age was  $D/c$ .

#### 1.1.1 Friedman Robertson Walker Models

With improved observations in the past decades, we have a good reason to believe that the cosmological principle which states that Universe is isotropic and homogeneous holds well on large scales. According to General Relativity, Einstein's field equation relates Einstein tensor to energy-momentum tensor of the matter which allows the metric tensor of space-

time manifold to determine the spatial and temporal distances as well as the geodesics. Thus the metric plays the role of gravitational potential.

In an idealized universe that follows cosmological principle, the two neighboring events in space separated by  $ds$  follows a Robertson-Walker metric (RW metric) written as

$$ds^2 = c^2 dt^2 - a^2(t)[d\chi^2 + f_K^2(\chi)(d\theta^2 + \sin^2 \theta d\phi^2)], \quad (1.1)$$

where  $t$  and  $a(t)$  are the cosmic time and scale factor, respectively.  $\theta$  and  $\phi$  are the coordinates of a unit sphere, and  $\chi$  and  $f_K(\chi)$  are the comoving radial coordinate and comoving angular diameter distance, respectively. The curvature  $K$  take value -1, 0 and 1 for negative, zero and positive curvature. One can solve the Einstein's field equation by inserting the RW metric to get the two independent Friedmann equations

$$\left(\frac{\dot{a}}{a}\right)^2 = \frac{8\pi G}{3}\rho - \frac{Kc^2}{a^2}, \quad (1.2)$$

$$\left(\frac{\ddot{a}}{a}\right) = -\frac{4\pi G}{3}\left(\rho + \frac{3p}{c^2}\right), \quad (1.3)$$

that indicates that the matter content mimics the properties of a perfect fluid with density  $\rho$  and pressure  $p$ . Here  $G$  is the Gravitational constant. The expansion rate  $\dot{a}/a = H(t)$ , where  $H(t)$  is the time-dependent Hubble constant and at present time its equivalent to  $H_0$ .

The density is defined as the sum of the densities of pressureless matter  $\rho_M(t)$ , radiation  $\rho_R(t)$  and dark energy  $\rho_\Lambda(t)$ . The time dependence of these components is estimated by employing the first law of thermodynamics that states that the change in energy  $dU$  is equivalent to  $-pdV$ , where  $V = 4\pi r^3/3$  is the volume of the sphere and  $U = 4\pi\rho c^2 r^3/3$  is the energy contained in it. Writing the comoving radius as a function of scale factor i.e.  $r(t) = a(t)x$ , the first law of thermodynamics can be written as

$$d(\rho c^2 a^3) = -p da^3. \quad (1.4)$$

For pressureless matter  $p = 0$ , thus

$$\rho_M(t) = \rho_{M,0} a^{-3}(t), \quad (1.5)$$

radiation pressure is related to density as  $p_R = \rho_R c^2/3$ , that gives

$$\rho_R(t) = \rho_{R,0} a^{-4}(t). \quad (1.6)$$

For an empty space, the vacuum energy density is independent of the cosmic time, that implies  $p_\Lambda = -\rho_\Lambda c^2$ . Thus, dark energy density is independent of time.

Using equation 1.3, the total density of Universe, assuming zero curvature ( $K = 0$ ), can be written as

$$\rho_0 = \frac{3H_0^2}{8\pi G}, \quad (1.7)$$

which is also called as the critical density of universe ( $\rho_{\text{cr}}$ ). This is used to define unit-less density parameters as

$$\Omega_{\text{M}} = \frac{\rho_{\text{M},0}}{\rho_{\text{cr}}}; \quad \Omega_{\text{R}} = \frac{\rho_{\text{R},0}}{\rho_{\text{cr}}}; \quad \Omega_{\Lambda} = \frac{\rho_{\Lambda}}{\rho_{\text{cr}}}. \quad (1.8)$$

This way the total density can be written as

$$\Omega_0 = \Omega_{\text{M}} + \Omega_{\text{R}} + \Omega_{\Lambda}. \quad (1.9)$$

Using these above mentioned equations, we can re-write equation 1.2 as

$$H^2 = H_0^2 \left[ \frac{\Omega_{\text{R}}}{a^4} + \frac{\Omega_{\text{M}}}{a^3} + \Omega_{\Lambda} - \frac{Kc^2}{a^2 H_0^2} \right], \quad (1.10)$$

and at  $a = 1$ , curvature  $K = (\Omega_{\text{M}} + \Omega_{\Lambda} - 1)H_0^2/c^2$ , thus we get

$$H^2 = H_0^2 \left[ \frac{\Omega_{\text{R}}}{a^4} + \frac{\Omega_{\text{M}}}{a^3} + \Omega_{\Lambda} + (1 - \Omega_0)a^{-2} \right], \quad (1.11)$$

Also, as Hubble constant is defined as  $H = \dot{a}/a$ , the time interval becomes  $dt = da/aH$  and the age of Universe is written as

$$t(a) = \frac{1}{H_0} \int_0^a \left[ \frac{\Omega_{\text{R}}}{a'^2} + \frac{\Omega_{\text{M}}}{a'} + \Omega_{\Lambda} a'^2 + (1 - \Omega_0) \right] da'. \quad (1.12)$$

Here, the subscript zero and the density parameters  $\Omega_{\text{M}}$ ,  $\Omega_{\text{R}}$  and  $\Omega_{\Lambda}$  refer to their values at  $a(t) = 1$ .

Electromagnetic radiation follows null geodesics, thus for them  $ds^2 = 0$  and given the isotropy of spatial metric  $\theta$  and  $\phi$  are constant for spatial projections of geodesics, thus for light rays  $cdt = -a(t)d\chi$ . Therefore, the radial coordinates of the source, whose light reaches us today (at  $t_0$ ) can be calculated as

$$\chi(t) = \int_t^{t_0} \frac{cdt'}{a(t')}. \quad (1.13)$$

If a source emits twice at times  $t$  and  $t + dt_s$  and an observer receives them at times  $t_0$  and  $t_0 + dt_0$ , then we find

$$dt_e = a(t)dt_0, \quad (1.14)$$

or in other words, due the cosmic expansion, the two emissions separated by time  $dt_s$  in the source plane are observed in a stretched interval depending on the scale factor  $a(t)$ . In terms of frequency of the emitted radiation, equation 1.14 can be translated into  $\nu_s = \nu_0/a(t)$ , which means the source is red-shifted due to the expansion of Universe, where the redshift ( $z$ ) is given as

$$(1 + z) = \frac{\nu_s}{\nu_0} = \frac{1}{a(t)}. \quad (1.15)$$

For a flat curvature ( $K$ ) today i.e. at  $a = 1$ ,  $\Omega_{\text{M}} + \Omega_{\Lambda} = 1$  (as  $\Omega_{\text{R}} \sim 0$  today) and using equation 1.11, for  $\Omega_{\text{M}} < 1$ , we find that the Universe expands for all values of  $a$ . In the limit of  $a \rightarrow 0$ , the size of the Universe is formally zero. This epoch where both matter and radiation densities diverge is know as Big Bang.

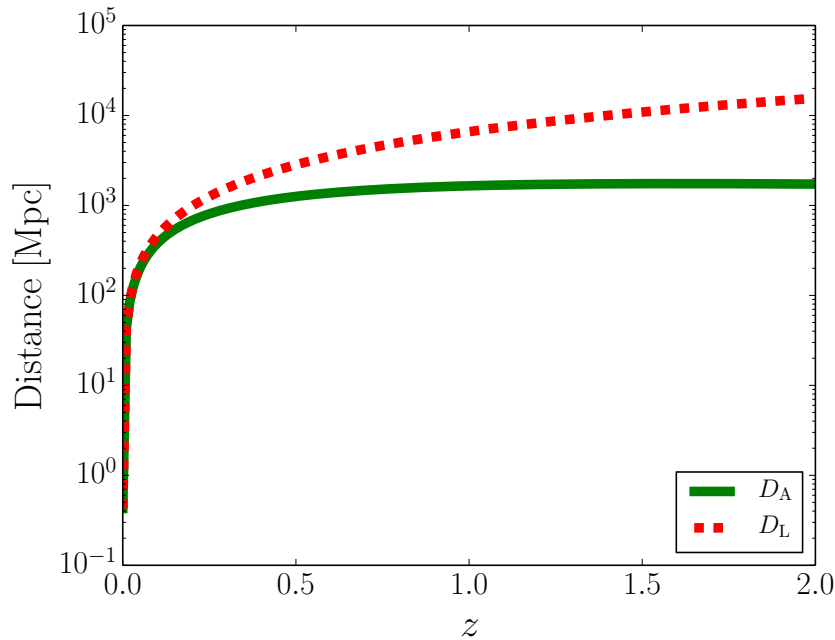


Figure 1.1: The angular diameter ( $D_A$ ) and luminosity ( $D_L$ ) distances as a function of redshift. The plot is constructed using the flat cosmology with  $\Omega_M = 0.3$  and  $H_0 = 70 \text{ Km s}^{-1} \text{ Mpc}^{-1}$ .

### 1.1.2 Distance and Volume Measures

Unlike the Euclidean preconception that there is a uniquely defined correct measure of distance between two objects, there is no unique meaning of distance in the context of spacetime. However, one can define distances by constructing methods for measuring them. The most commonly used measurements of distances in cosmology are angular diameter distance and luminosity distance.

If the physical diameter of a source is  $d$  and the angular diameter is  $\varphi$  then given the redshift  $z$  of the source, the angular diameter distance is  $D_A(z) = d/\varphi$ . In terms of the RW metric with  $\varphi = d\theta$  and  $ds = d$ , this is written as

$$D_A(z) = a(z)f_K(\chi). \quad (1.16)$$

The comoving distance between two sources defined as the spatial distance between the intersections of the worldline is written as

$$\chi(z_1, z_2) = \chi(z_2) - \chi(z_1) = \frac{c}{H_0} \int_{a(z_2)}^{a(z_1)} [a\Omega_M + a^2(1 - \Omega_M - \Omega_\Lambda) + a^4\Omega_\Lambda]^{-1/2} da. \quad (1.17)$$

This relation is obtained using equation 1.13 with  $dt = da/\dot{a} = da/aH$ , for two sources with  $z_1 < z_2$ . Thus the comoving distance from an observer at Earth is equivalent to  $\chi(z)$ . Also for a vanishing curvature  $K = 0$ ,  $f_K(\chi) = \chi$ , thus the angular diameter distance can

be written as

$$D_A(z) = a(z)\chi(z). \quad (1.18)$$

The luminosity distance relates the the flux of a source to its luminosity. For a given flux  $S$  and luminosity  $L$  of a source luminosity distance is written as

$$D_L = \sqrt{\frac{L}{4\pi S}}. \quad (1.19)$$

As mentioned before, in contrast to the Euclidean space where these two distance would yield same results. These two measurements of distances in curved spacetimes are not same and are related to each other as

$$D_L = (1 + z)^2 D_A. \quad (1.20)$$

Fig. 1.1 shows the angular diameter and luminosity distances as a function of redshift for a given cosmology. The comoving volume element of a region in sky with a solid angle  $\omega$  can be written in terms of the comoving distance as

$$dV = \chi(z)\omega \frac{d\chi}{dz} dz, \quad (1.21)$$

where the finite volumes are measured by integrating over this expression and the proper volume is  $a^3 dV$ .

### 1.1.3 Thermal History of Universe

The beginning of Universe started with a Big Bang which was followed by inflation and nucleosynthesis and Universe became transparent to the radiation after recombination when the temperature and age of the Universe were around 3000 K and  $3 \times 10^5$  years, respectively. This was followed by re-ionization era where the first stars were formed in the Universe. Fig. 1.2 shows the history of Universe as a function of time, temperature and energy at different epochs.

Cosmic expansion of the Universe preserves the photon distribution through out its history. Photons follow Planck spectrum throughout the cosmic expansion. In earlier epochs the temperature of Universe is very high and it falls with redshift as the Universe expands. If  $T_0$  is the temperature today then at a redshift  $z$  it is as high as  $T_0(1 + z)$  K. As we approach to  $a \rightarrow 0$ , the temperature tends to infinity. The particles with mass  $m$  are generated in the process of expansion if the  $T \geq mc^2$ . Assuming that the physical laws hold even in the early times, the evolution of the comic expansion can be followed using the established physics probed in accelerators like Large Hadron Collider (LHC) upto energies of  $\leq 100$  GeV.

As the Universe is expanding, the distribution of particles in equilibrium with photons is continuously changing with time. For them to remain in thermodynamic equilibrium, the reaction rates of particles must be higher than the expansion rate of Universe. As

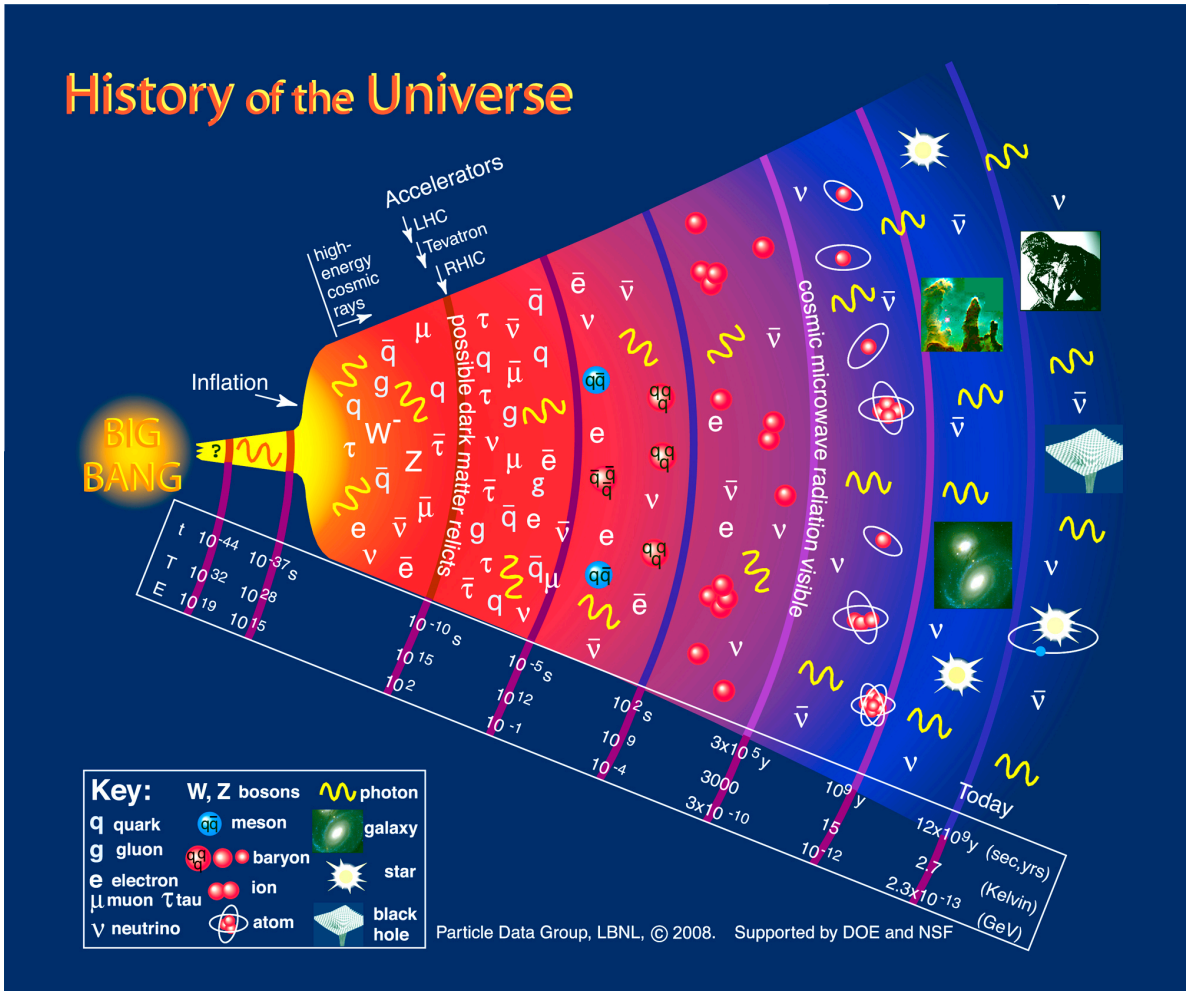


Figure 1.2: Systematic picture of the expansion of Universe with time, temperature and energy specified in seconds, Kelvin and GeV, respectively. The information about various particles produced at different cosmic times is shown in the bottom left. The beginning of Universe started with a Big Bang followed by a brief period of inflation. At various energies, particles like protons, neutrons, electrons, positrons and neutrinos were formed and were coupled to the radiation until the era of recombination when Universe became transparent and the CMB started to propagate freely towards us. This is followed by dark ages and then re-ionization when the first stars were formed in the Universe. The tiny fluctuations in the density fields resulted in the structure that we see today shown as the stars and galaxies in the right end of the figure. Credit: Particle Data Group, LBNL.

both temperature and Hubble constant are inversely proportional to the scale factor, thus this is directly linked to the temperature of the epoch. If the rate of expansion becomes larger than the rate of reaction of particles then they drop out of the equilibrium state and their formation halts. At temperatures higher than 1 GeV, protons and neutrons are produced but as the Universe cools down with its expansion these particles can no longer be produced as their rest masses are larger than 1 GeV. Thus, the abundance of these particles is smaller at later times. Similarly, at a few MeV, electrons, positrons and neutrinos are produced through the photon-photon pair creation as these particles can be in thermodynamic equilibrium with photons at these temperatures.

At  $\sim 1.4$  MeV, the reaction rates of neutrinos becomes smaller than the cosmic expansion rate and thus, they decouple from other particles and travel in an expanding Universe without any interaction. At  $\sim 0.7$  MeV, protons and neutrons are no longer in equilibrium with other particles. The pairs of  $e^+$  and  $e^-$  stop forming at  $\sim 0.5$  MeV and they rather start annihilation reactions that transfer the energy to the photons. The lightest nuclei like  $\text{He}^4$  are produced when temperature drops to  $\sim 0.1$  MeV and at 0.3 eV the baryonic content of Universe becomes neutral as electrons combine with charged atoms marking the era of recombination. At this epoch neutral hydrogen forms and photons stop interacting with the baryonic matter to propagate through the Universe forming the Cosmic Microwave Background (CMB). This is the limit of our observations as Universe is opaque before and we can only see the patterns of matter overdensities in the CMB which later on results into the structure that we see today.

### 1.1.4 Structure Formation

The structure formation in Universe is due to the tiny perturbations ( $\delta = \Delta\rho/\rho$ ) assumed to be present before the recombination era. These perturbations are presumed to be there due to quantum fluctuations from the epoch of inflation. The perturbations then grow due to the gravitational instabilities and are affected by the other effects like free streaming of the particles at different times in the process of evolution. The traces of these perturbations or inhomogeneities can be seen in the CMB radiation which shows relative temperature fluctuations with  $\Delta T/T \sim 10^{-5}$ .

Universe was dominated by the radiation in very early times. As matter starts to form, Universe proceeds toward an era of matter domination and the scale factor where these two densities cross over is denoted as  $a_{\text{eq}}$  i.e the era of matter radiation equality. The growth of dark matter perturbations depend upon the matter or radiation dominated states of Universe. Also, the rate with which these perturbations grow depends on whether the scale of inhomogeneities is smaller or larger than the horizon size given as

$$R_{\text{H}} = \frac{c}{aH(a)}. \quad (1.22)$$

If the size of perturbations is much larger than the size of horizon then the perturbations are called as superhorizon perturbations otherwise, if the horizon size is much larger, then they are called as subhorizon perturbations. In radiation dominated era with  $a \ll a_{\text{eq}}$ ,

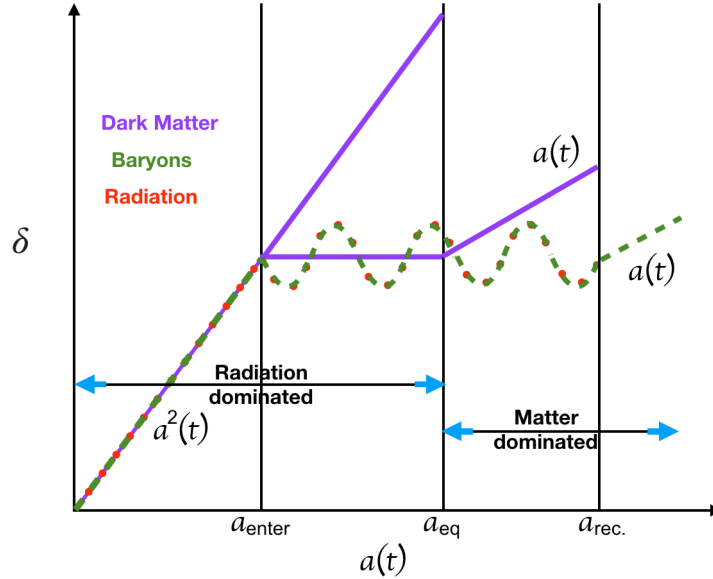


Figure 1.3: The growth of dark matter (purple), baryon (green) and radiation (red) perturbations in radiation and matter dominated eras of Universe. The perturbations before entering the horizon grow similarly for all these components in radiation dominated era. After they enter the horizon, the dark matter perturbations stop to grow and baryon-photon fluid starts oscillating together. In matter dominated era, dark matter perturbations grow with scale factor while baryon-photon fluid keeps oscillating until the recombination. At recombination photons free stream and baryonic perturbations start growing with scale factor.

the superhorizon perturbations grow as  $\delta \propto a^2$  and perturbations inside the horizon i.e. subhorizon perturbations do not grow at all. In matter dominated Universe with  $a \gg a_{\text{eq}}$ , both super and sub horizon perturbations grow as  $\delta \propto a$ .

The horizon size is not constant and grows as a function of scale factor. At some point of time, when the Universe is still dominated by radiation, some perturbations enter the horizon i.e the size of horizon becomes larger than the length of perturbations. This time is denoted as  $a_{\text{ent}}$  in terms of scale factor. The perturbations which enter the horizon behave like subhorizon perturbations and stop to grow. Also, if perturbations enter the horizon in matter dominated era, then there is no change in their growth rate as both super and sub horizon perturbations grow with scale factor in matter dominated Universe.

The radiation and baryon fluid is coupled to each other in the era before recombination occurs. Their superhorizon perturbations in radiation dominated era grows like dark matter perturbations as  $a^2$ . The baryon-photon fluid however, begins to oscillate when perturbations enter the horizon in radiation dominated era due to radiation pressure. These oscillations also continue in matter dominated era until the recombination era where baryons decouple with photons. After recombination, baryons are no longer oscillating and they continue to grow in a similar way as dark matter i.e. with  $\delta \propto a$ , which results into the visible Universe that we see today along with underlying dark matter. Fig. 1.3

summarizes the growth of perturbations in matter and radiation dominated era for dark matter, baryon and radiation.

The density fluctuations grow differently depending upon when they enter the horizon as discussed above. The growth of small scale perturbations which enter the horizon in radiation dominated era is suppressed as compared to those which enter the horizon in matter dominated era. This effect can be quantified as the scale dependent Transfer functions  $T(k)$ , where  $k$  is the wavenumber related to the scale of perturbations. Considering the scale of density perturbations  $k$  and  $k_s$ , such that, the latter entered the horizon in matter dominated era. The superhorizon perturbations at a very early time with scale factor  $a_i$  and at present with  $a = 1$ , can be denoted for scales  $k$  as  $\delta_i(k)$  and  $\delta_0(k)$  and as  $\delta_i(k_s)$  and  $\delta_0(k_s)$  for scales  $k_s$ , respectively. Then the ratio of fluctuation amplitudes for different scales or wavenumbers is defined as

$$T(k) = \frac{\delta_0(k) \delta_i(k_s)}{\delta_0(k_s) \delta_i(k)}. \quad (1.23)$$

These ratios also take the free streaming particles into account i.e. the relativistic particles that can erase their own density perturbations as soon as they enter the horizon. In a Cold Dark Matter (CDM) scenario, the particles become non-relativistic (except neutrinos) well before  $a_{\text{eq}}$ , thus the small scale perturbations survive and  $T(k) < 1$ . If the Universe is dominated by Hot Dark Matter (HDM) then small scale structures are erased due to free streaming and only large scale perturbations survive as the HDM particles are still relativistic at  $a_{\text{eq}}$ . Thus, one can constrain the density of HDM and mass of neutrinos by constraining the suppression at small scales.

In order to get the current density fluctuations, one needs to know the initial fluctuation field. This can be done by predicting the statistical properties of initial density fluctuation field i.e. the initial power spectrum ( $P(k)$ ). The power spectrum of the density fluctuations in Universe is given as

$$P(k) = Ak^{n_s}T^2(k), \quad (1.24)$$

where  $A$  is the amplitude of the initial perturbations and  $n_s$  is the spectral index. If  $n_s = 1$ , then the perturbations which enter the horizon independent of the era, always have same amplitude. We know that the superhorizon fluctuations existed in the early Universe as we see the temperature fluctuations in CMB sky on angular scales much larger than a degree. In the framework of standard Friedmann-Lemaitre expansion, Universe has never been in causal contact on large scales before recombination. However, inflationary theories suggest that the superhorizon fluctuations can be produced as during the exponential growth of Universe small quantum fluctuations were inflated to large scales. This leads to the conclusion that the initial power spectrum was indeed a power law with spectral index slightly smaller than one.

In a matter dominated Universe, perturbations grow as a function of the grown factor  $D(a)$  and the power spectrum is given as

$$P(k, a) = P(k)D^2(a), \quad (1.25)$$

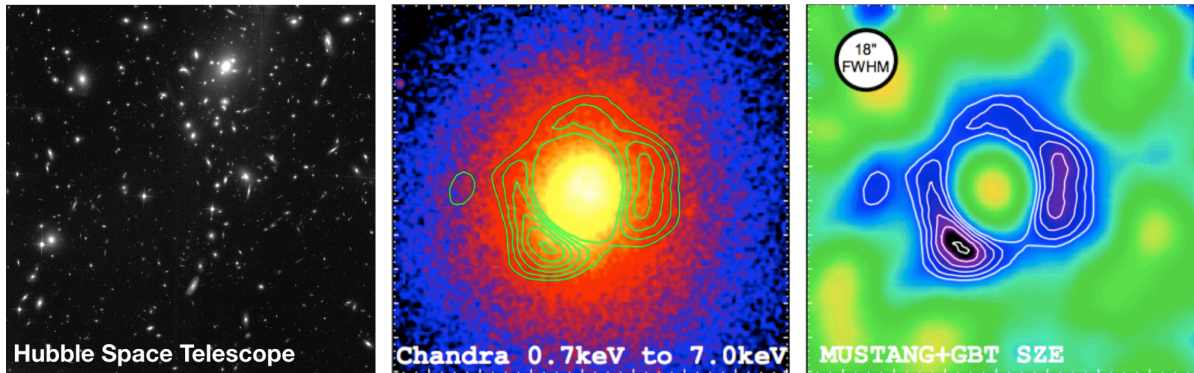


Figure 1.4: The multi-wavelength observations of Abell 1835 galaxy cluster ( $z \sim 0.25$ ) from left to right: in optical with Hubble space telescope  $3.18'$  view (credit: NASA/STScI/WikiSky), in X-ray using *Chandra* 0.7 keV to 7.0 keV image smoothed with a  $1.5''$  Gaussian (Korngut et al., 2011) and in radio using MUSTANG SZE image smoothed to  $18''$  resolution (Korngut et al., 2011).

in the limit of linearly growing fluctuations. At sufficiently small scales, the linear theory breaks down and the evolution of power spectrum can be estimated using numerical methods.

## 1.2 Galaxy Clusters

Galaxy clusters reside in the most massive gravitationally bound halos in the cosmic web of large scale structure (LSS). These halos are produced by coherent infall of galaxies and hierarchical merging through the cosmic history of Universe. Galaxy clusters mainly consist of galaxies, gas, dark matter and a population of relativistic particles. Galaxy clusters can be observed across the electromagnetic spectrum. In optical and near-Infrared wavebands clusters emit stellar light from galaxies. The thermal bremsstrahlung from Intra Cluster Medium (ICM) and line emission from ionized plasma helps their detection in X-rays. Sunyaev-Zel'dovich Effect (SZE) facilitates their detection in mm-wavelength (radio) CMB sky. Fig. 1.4 shows the Abell 1835 cluster with  $z \sim 0.25$  observed in optical, X-ray and mm-wavelengths.

### 1.2.1 Multiwavelength Observations of Galaxy Clusters

In this section I will briefly describe the observations of galaxy clusters in optical, X-ray and radio wavelengths. As this thesis is dedicated to the SZE detected clusters, thus I will put more emphasis on SZE numerical framework.

#### Optical and Infrared Observations

The emission in the various wavebands of the optical and near-infrared regimes of the electromagnetic spectrum is dominated by the stars in galaxies (see Fig. 1.4, left panel). The

central regions of galaxy clusters are dominated by the early type elliptical and lenticular galaxies (e.g. Hennig et al., 2016), which are the most luminous and largest sources and are also known as Brightest Cluster Galaxies (BCGs). The main observable as a proxy for mass for optically detected clusters is richness  $\lambda$  (e.g. Saro et al., 2015; Melchior et al., 2017) that describes the number of galaxies in an aperture.

In the recently completed Sloan Digital Sky Survey (SDSS),  $\sim 13,800$  maxBCG clusters are observed with  $\lambda \geq 10$  and redshift range  $0.1 < z < 0.3$  (Koester et al., 2007b). The maxBCG is a red sequence identification method where the objects with  $i$ -band magnitude larger than  $0.4 L_*$  are selected and information about the spatial clustering of red-sequence galaxies, brightest cluster galaxies and multiple colors is added to refine the cluster search (Koester et al., 2007a). In the ongoing Dark Energy Survey (DES), red-sequence Matched-filter Probabilistic Percolation algorithm (redMaPPer; Rykoff et al., 2014) is employed to detect the clusters. The redMaPPer algorithm detects clusters as over-densities of red-sequence galaxies. Precisely, the algorithm estimates the probability of a red galaxy to be the cluster member using a matched filter and then measures the richness by summing up the membership probabilities of galaxies in the cluster region.

The cosmological constraints from SDSS maxBCG sample are presented in Rozo et al. (2010). The constraints from optical cluster surveys are limited by the mass-observable relations which are affected by the cluster selection effects, for e.g. the effects like projection of line of sight structures and groups. The individual cluster mass is estimated through the dynamical mass measurements assuming that the cluster is in dynamical equilibrium. The dynamical mass is estimated within the cluster virial region using the Jeans equation which requires the information about galaxy number density, velocity anisotropy and three dimensional velocity dispersion profiles, where the latter is estimated from projected galaxy number density and velocity dispersion profiles under the different model assumptions.

## X-ray Observations

The galaxy clusters shine bright in X-rays due to the gas which (unlike in the field) is thermally heated to temperatures as high as  $10^8$  K due to the gravitational contraction. Clusters appear as luminous and extended sources in X-ray sky (see Fig. 1.4, middle panel). There are mainly three emission mechanism in X-rays: free-free emission (thermal bremsstrahlung), bound-bound emission (line emission) and free-bound emission (recombination). The electron density in galaxy clusters varies from  $0.1 \text{ cm}^{-3}$  to  $10^{-5} \text{ cm}^{-3}$  from cluster's cool cores to their outskirts.

The X-ray cluster catalogs are mostly built using the data from ROSAT satellite which includes 6 months of observations of ROSAT All Sky Survey (RASS) followed by 8 years of pointed observations, where the latter although cover much smaller area but is twice as deep as RASS. A Meta-Catalog of X-ray detected Clusters of galaxies (MCXC, Piffaretti et al., 2011) is compiled from the publicly available RASS based catalogs, such as, NORAS (Böhringer et al., 2000), REFLEX (Böhringer et al., 2004), BCS (Ebeling et al., 1998, 2000), SGP (Craddace et al., 2002), NEP (Henry et al., 2006), MACS (Ebeling et al., 2001), CIZA (Ebeling et al., 2002; Kocevski et al., 2007) and serendipitous catalogs from

pointed observations such as, 160SD (Mullis et al., 2003), 400SD (Burenin et al., 2007), SHARC (Romer et al., 2000), WARPS (Perlman et al., 2002; Horner et al., 2008), and EMSS (Gioia & Luppino, 1994; Henry, 2004). The catalog contains a total of 1,743 clusters in the whole sky.

X-ray observations facilitate direct measurements of cluster masses assuming the hydrostatic equilibrium (HSE). The precisely determined spatially resolved spectra of clusters allows us to measure the density and temperature profiles of the ICM. Given the density and temperature profiles, the mass of a spherically symmetric cluster in HSE can be deduced in the relaxed state of the cluster. Another way to estimate HSE mass for relaxed clusters is by using the pressure profiles (e.g. Arnaud et al., 2010). Given the density profile, the pressure gradient is proportional to the cluster mass. For merging systems, HSE stops to pertain and a bias gets introduced in the HSE assumed cluster masses. This bias is difficult to estimate as it depends on the dynamical state of cluster and can differ with non-thermal pressure from cluster to cluster (for e.g. Nagai et al., 2007).

## SZE Observations

A number of secondary anisotropies are introduced into the CMB radiation as it travels through the Universe from the last scattering surface towards us. As it passes through the galaxy clusters, highly energetic electrons raise the energy of non-negligible number of CMB photons through inverse Compton scattering, resulting into a shift in the frequency spectra of CMB. A quantitative description of this effect is given by Rashid Sunyaev and Yakov Zel'dovich (Sunyaev & Zel'dovich, 1972). The galaxy clusters have hot ionized gas at temperatures of 1-10 KeV with electron number density  $\lesssim 0.1$  particle/cm<sup>3</sup>. The mass of this ionized plasma is in the range of  $10^{13} - 10^{14} M_{\odot}$  and as many as 1-2 percent of the incoming CMB photons are scattered by cluster's energetic electrons. The energy of a particle is related to its mass and momentum via relativistic formula

$$E^2 = (Pc)^2 + m^2c^4, \quad (1.26)$$

where  $E$ ,  $P$ ,  $m$  are the energy, momentum and rest mass of a particle, respectively. For photons, rest mass is zero, thus  $E = Pc$ . Energy is related to frequency  $\nu$  as  $E = h\nu$ , where  $h$  is the Planck's constant. Thus momentum is related to wavelength  $\lambda$  as  $P = h/\lambda$ . The shift in wavelength is a result of the single electron imparting momentum to a single photon, thus laws of conservation of momentum are imposed.

When a photon of energy  $E_i$  and momentum  $P_i$  collides with an electron having rest mass  $mc^2$ , the electron recoils with energy  $E_r$  and momentum  $P_r$  leaving photon with energy  $E_f$  and momentum  $P_f$ . Applying conservation laws, we have

$$h(\nu_f - \nu_i) = (m_0 - m_r)c^2, \quad (1.27)$$

$$P_i = P_f + P_r, \quad (1.28)$$

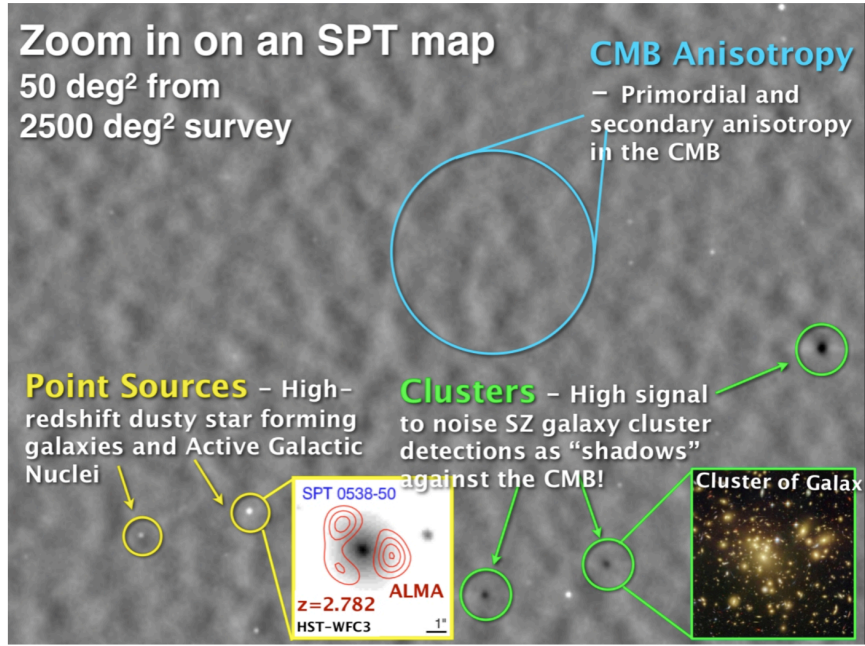


Figure 1.5: The match filtered mm-wavelength map of  $50 \text{ deg}^2$  of SPT region showing the CMB sky. Three high signal to noise galaxy clusters are shown as black spots in contrast to the CMB in the bottom-right of map. In the bottom-left two point sources (an AGN and a dusty galaxy) are shown as shining white spots in the radio sky. Credit: SPT collaboration.

with momentum along X-axes

$$h/\lambda_i = h/\lambda_f \cos \theta + m_r v_r \cos \phi, \quad (1.29)$$

and Y-axes

$$h/\lambda_f \sin \theta = m_r v_r \sin \phi, \quad (1.30)$$

and combining these we get the change in wavelength from Compton scattering as

$$\lambda_f - \lambda_i = \Delta \lambda = \frac{h}{m_0 c} (1 - \cos \theta). \quad (1.31)$$

Thus the change in wavelength of a photon depends on the rest mass of the counterpart and the deflection angle of the photon.

Inverse Compton effect as the name suggests is just the opposite of Compton effect. Highly energetic electrons originated from various sources in clusters like Supernova explosions, when interact with low energy CMB photons then through this scattering the average energy of photons increase. This results in a spectral distortion of CMB in a characteristic manner such that, a fraction of photons move from the Rayleigh-Jean's to the Wein's side of the Planck spectrum. The spectral signature shows a decrease in CMB intensity at frequencies lower than 218 GHz and an increase at higher frequencies. A key feature of this effect is that the SZE surface brightness is insensitive to the redshift of cluster. This is simply because a clump of gas with a given temperature and number density

transforms the CMB spectrum in a similar way regardless of its redshift. This makes SZE an important tool for the detection of clusters at unprecedented high redshifts because the only important parameter that sets the detection limit is the mass of cluster. Fig. 1.5 shows a zoom in version of SPT map of CMB sky, where galaxy clusters with detection limit greater than SPT threshold appear as black spots.

The non-relativistic calculations of SZE yield a simple expression for the change of CMB intensity  $I_{SZ}$  induced by scattering of CMB by electrons

$$\Delta I_{SZ} = g_\nu I_0 y, \quad (1.32)$$

where  $I_0 = 2(K_B T_{CMB})^3 / (hc)^2$  and  $y$  is comptonization parameter written as

$$y = \int \frac{n_e k_B T_e \sigma_T}{m_e c^2} dl, \quad (1.33)$$

where  $\sigma_T$  is Thomson cross-section and  $n_e$ ,  $m_e$  and  $T_e$  are the electron number density, rest mass and temperature, respectively. The frequency dependence is given as

$$g_\nu = x \coth\left(\frac{x}{2}\right) - 4, \quad (1.34)$$

with  $x = h\nu / k_B T_{CMB} \simeq \nu / (56.78 \text{ GHz})$  for  $T_{CMB} = 2.725 \text{ K}$ . The SZE spectral distortion can also be expressed in terms of change in temperature as

$$\frac{\Delta T_{SZ}(\theta)}{T_{CMB}} = g_\nu \frac{\sigma_T}{m_e c^2} \int_{-\ell_{out}}^{\ell_{out}} P_e \left( \sqrt{\ell^2 + \theta^2 D_A^2} \right) d\ell, \quad (1.35)$$

where  $\theta$  is the angular distance from the center of the galaxy cluster,  $\ell$  is the radial coordinate from the cluster center along the line of sight,  $P_e(r)$  is the electron pressure profile. Further, equation (1.35) can be expressed as

$$\Delta T_{SZ}(\theta) = 273 \mu\text{K} g_\nu \left[ \frac{P_e^{2d}(\theta)}{25 \text{ eV cm}^{-3} \text{ Mpc}} \right]. \quad (1.36)$$

Here  $P_e^{2d}(\theta) = \int_{-\ell_{out}}^{\ell_{out}} P_e \left( \sqrt{\ell^2 + \theta^2 D_A^2} \right) d\ell$  is the projected electron pressure profile with  $\ell_{out}$  equivalent to  $\sqrt{r_{out}^2 - \theta^2 D_A^2}$ , such that, the pressure profile is truncated at  $r_{out} = 6R_{500}$ . For the electron pressure profile, we considered a generalized NFW model (Nagai et al., 2007)

$$P(x) = \frac{P_0}{(c_{500} x)^\gamma [1 + (c_{500} x)^\alpha]^{(\beta-\gamma)/\alpha}}, \quad (1.37)$$

where the parameters  $\gamma$ ,  $\alpha$ , and  $\beta$  are the central ( $r \ll r_s$ ), intermediate ( $r \sim r_s$ ), and outer slopes ( $r \gg r_s$ ). Also here  $x = r/R_{500}$  and  $c_{500}$  is the concentration index. Arnaud et al.

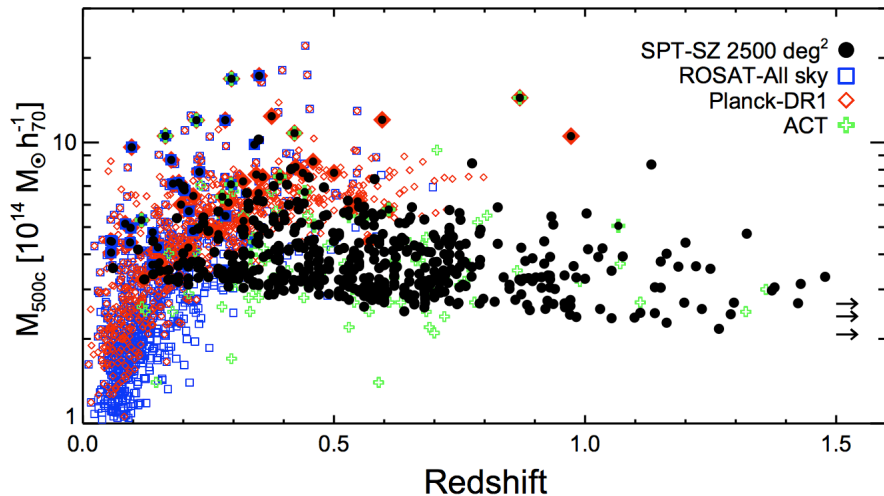


Figure 1.6: X-ray and SZE selected cluster samples: The estimated mass versus redshift for the 516 optically confirmed clusters from the SPT catalog (Bleem et al., 2015), 91 clusters from the ACT survey (Marriage et al., 2011; Hasselfield et al., 2013), 809 clusters from the Planck survey (Planck Collaboration et al., 2013a), and 740 X-ray clusters selected from the ROSAT all-sky survey (Piffaretti et al., 2011). While the SPT data provides a nearly mass-limited sample, the cluster samples selected from ROSAT and Planck data are redshift-dependent owing to cosmological dimming of X-ray emission and the dilution of the SZ signal by the large Planck beams, respectively. Credit: Bleem et al. (2015).

(2010) estimated the parameters of this generalized NFW profile by fitting the observed average scaled profile in the radial range  $[0.03 - 1]R_{500}$ , combined with the average simulation profile beyond  $R_{500}$ . Their best fitting parameters are tabled as

$$[P_0, c_{500}, \gamma, \alpha, \beta] = [8.403h_{70}^{-3/2}, 1.177, 0.3081, 1.0510, 5.4905],$$

and the pressure profile as a function of radius is written as

$$P_e(r) = 1.65 \times 10^{-3} E(z)^{8/3} \left[ \frac{M_{500}}{3 \times 10^{14} h_{70}^{-1} M_{\odot}} \right]^{2/3 + \alpha_P} \times P(x) h_{70}^2 \text{ keV cm}^{-3}, \quad (1.38)$$

where  $\alpha_P \simeq 0.12$  is the slope of the relation. Combining equations (1.35) - (1.38) a redshift dependent relation between  $\Delta T_{SZ}(\theta)$  and  $M_{500}$  is obtained.

The first galaxy cluster sample selected through the Sunyaev-Zel'dovich Effect (SZE; Sunyaev & Zel'dovich, 1972) emerged in the last decade (Staniszewski et al., 2009); since then, high frequency mm-wave surveys by the South Pole Telescope (SPT; Carlstrom et al., 2011), the Atacama Cosmology Telescope (ACT; Fowler et al., 2007), and Planck (Planck Collaboration et al., 2011) have enabled the SZE selection of large cluster samples and their use to constrain cosmological parameters (Vanderlinde et al., 2010; Sehgal et al., 2011; Benson et al., 2013; Reichardt et al., 2013; Hasselfield et al., 2013; Bocquet et al., 2015; Planck Collaboration et al., 2015a; de Haan et al., 2016).

Fig. 1.6 shows a comparison between the mass and redshift distributions for X-ray and SZE selected galaxy clusters from various surveys. The mass threshold of SPT sample declines slowly with redshift which is due to the higher temperatures for same mass clusters. Also, at lower redshifts increased power of primary CMB fluctuations at large angular scales and atmospheric noise raises the mass threshold. The cosmological dimming of the X-ray emission increases the mass threshold for X-ray samples at higher redshifts. The large beam size for Planck causes the dilution of small angular scale SZE signal at high redshifts and only high mass objects are observable.

### High frequency Radio galaxies

At millimeter wavelengths we observe extragalactic sources that can be separated into two categories: Active Galactic Nuclei (AGN) and dust enshrouded star-forming galaxies (DSFGs; e.g. Vieira et al., 2010). AGN emit synchrotron radiation from the relativistic electrons in galaxies and have flat or decreasing flux with increasing frequency (flat and steep spectrum AGN). The main difference between the steep and flat spectrum AGN is the close alignment of the relativistic jet to the line of sight in the latter. The flat spectrum originates from the superposition of different self-absorbed components of radio jets; such AGN are collectively known as blazars. The blazars are further classified as BL Lacs and flat spectrum radio quasars (FSRQs) where the latter are more distant, more luminous, and have stronger emission lines (Ostriker & Vietri, 1990). The steep spectrum AGN with side-on emission from the extended radio lobes are mainly associated with elliptical and lenticular galaxies, and most of the radio sources in galaxy clusters have steep spectra (Coble et al., 2007; Tucci et al., 2011). DSFGs exhibit an increase in flux with frequency in the mm regime, and their emission comes from dust grains as a result of the re-emission of absorbed radiation (see Massardi et al., 2008; De Zotti et al., 2010, for further details).

### 1.2.2 Cluster Cosmology

The clusters have emerged as one of the most important and independent tools to put competitive constraints on the cosmological models. It is unique in a way that the degeneracies of key cosmological parameters ( $\Omega_M$  and  $\sigma_8$ ) are found to be almost orthogonal to their degeneracies from CMB probes. Thus together with CMB, clusters have enabled us to get the tightest constraints on fundamental theories of cosmology. In this section I will briefly present the methodology behind cluster cosmology and current constraints on cosmological parameters from SZE cluster survey.

#### Halo mass function and SZE observable

Dark matter halos are the most dense regions of the cosmic matter distribution in universe. The mass ( $M$ ) and radius ( $R$ ) of a halo is characterized by the definition of spherical overdensity ( $\Delta$ ), such that,  $M_\Delta$  is defined as the mass enclosed in a sphere where the mean

density is  $\Delta$ -times the critical density ( $\rho_{\text{crit}}$ ) of universe at the redshift of halo

$$M_{\Delta} = \frac{4}{3}\pi(\Delta\rho_{\text{crit}})R_{\Delta}^3. \quad (1.39)$$

Halo mass function ( $dn/dM(M, z)$ ) describes the halo abundance per unit volume and per unit mass as a function of redshift. The functional form of mass function given by Tinker et al. (2008) is most widely accepted, where it is deduced from the dark matter simulations. In these simulations, the center of halo is characterized as density peak and a sphere is drawn around it with radius  $R_{\Delta}$ .

To compare the theoretical mass function with the observations we need to scale the mass of clusters with their observable quantity. The observable for SZ effect is integrated  $Y_{500}$  parameter (or signal to noise ( $\zeta$ ) (e.g. Bocquet et al., 2015; de Haan et al., 2016)). We take the scaling relation between the mean SZE signal  $\bar{Y}_{500}$  and mass of cluster as described in Planck Collaboration et al. (2013b, 2016b)

$$E^{-\beta}(z) \left[ \frac{D_A^2(z)\bar{Y}_{500}}{10^{-4}\text{Mpc}^2} \right] = Y_* \left[ \frac{h}{0.7} \right]^{-2+\alpha} \left[ \frac{(1-b)M_{500}}{6 \times 10^{14}M_{\odot}} \right]^{\alpha}, \quad (1.40)$$

where  $E(z) \equiv H(z)/H_0$  with slope  $\beta$ ,  $D_A(z)$  is the angular diameter distance and  $b$  is the mean bias between the hydro-dynamical and true mass of the cluster.  $Y_*$  and  $\alpha$  are the normalization and slope of the relation, respectively. The scaling relation has an intrinsic scatter of  $\sigma_{\ln Y} = 0.123 \pm 0.023$ , which is assumed to be constant as a function of mass and redshift. As a standard practice the mass function is transformed from its theoretical space of mass and redshift to observable space as

$$\frac{dN}{dY_{500}dz} = \int_{M_L(z)}^{\infty} dM_{500} \frac{dn}{dM_{500}} \frac{dV(z)}{dz} \otimes P(Y_{500}|M_{500}, z), \quad (1.41)$$

where  $dV(z)/dz$  is the comoving volume in redshift bins.  $M_L(z)$  is the limiting mass for an SZE survey. The mass function is convolved with the probability distribution function  $P(Y_{500}|M_{500}, z)$  which describes the relation between mass and scaling relation, takes account of the intrinsic and observational uncertainties and is assumed to be log-normal.

## Cosmological Constraints

The base cosmological model which is tested extensively in the framework of various independent observations of Universe arises from the cold dark matter picture of Universe. We have established that Universe is expanding but the rate of expansion can either be linked to the cosmological constant  $\Lambda$  which motivates the  $\Lambda$ CDM model of Universe or the Universe can have a different expansion rate which can be tested in the framework of  $w$ CDM models, where  $w$  is the equation of state of dark energy. For  $w_0 = -1$ , the two models converge and one can ascertain that the nature of dark energy is that of the cosmological constant. The beauty of  $\Lambda$ CDM model is that it can be represented by just 6 parameters.

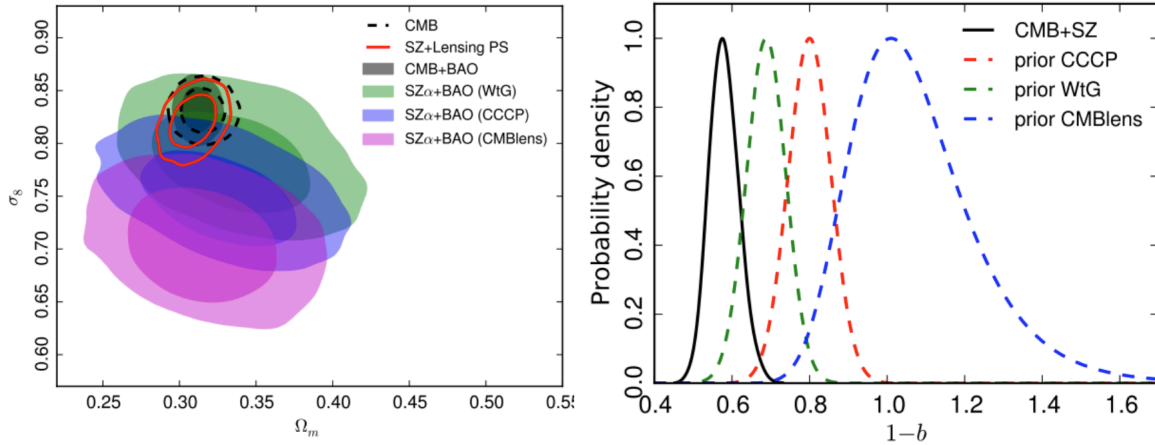


Figure 1.7: Left panel: Cosmological constraints at  $1 - \sigma$  and  $2 - \sigma$  levels in the plane of  $\Omega_m$  and  $\sigma_8$  from Planck CMB TT, TE, EE+lowP datasets (dashed contours) and their comparison with constraints from cluster number counts. Right panel: Comparison of the constraints on mass bias  $1 - b$  from cluster and primary CMB constraints. The solid black curve shows the posterior for the mass bias when SZE cluster and CMB datasets are combined. Credit: Planck Collaboration et al. (2015a).

These parameters are: matter density  $\Omega_M$ , baryon density  $\Omega_B$ , Hubble constant  $H_0$ , normalization of power spectrum  $\sigma_8$ , slope of the power spectrum  $n_s$  and reionization optical depth  $\tau$ . An additional parameter  $w_0$  can be added to test the  $w$ CDM cosmology. The cluster cosmology is mostly sensitive to  $\Omega_M$ ,  $\sigma_8$  and  $w_0$  parameters and is currently limited by the uncertainty in observable-mass scaling relation.

The recent cosmological constraints from an SZE detected cluster sample are shown in Fig. 1.7, where the left panel shows constraints at  $1 - \sigma$  and  $2 - \sigma$  levels in the plane of  $\Omega_m$  and  $\sigma_8$  from Planck CMB TT, TE, EE+lowP datasets (dashed contours) and their comparison with constraints from cluster number counts. The green, blue and violet contours give the constraints for the Weighting the Giants (WtG; von der Linden et al., 2014a), Canadian Cluster Cosmology Project (CCCP Hoekstra et al., 2015), and CMB lensing (Planck Collaboration et al., 2016a) cluster mass calibrations, respectively. The red contours give results from a joint analysis of the cluster counts, primary CMB and the Planck lensing power spectrum. Right panel shows a comparison of the constraints on mass bias  $1 - b$  from cluster and primary CMB datasets. The solid black curve shows the posterior for the mass bias when SZE cluster and CMB datasets are combined. The colored dashed curves show the three prior distributions on the mass bias.

More recent cluster cosmology is presented in a work by SPT collaboration (de Haan et al., 2016), where 377 cluster candidates identified at  $z > 0.25$  with a detection significance greater than five are used to estimate cosmological parameters using the cluster abundance measurements. This includes mass calibration from Chandra X-ray data for 82 clusters and a weak lensing-based prior on the normalization of the mass-observable scaling relations. The  $\Omega_M$  and  $\sigma_8$  are constrained to the values of  $0.289 \pm 0.042$  and  $0.784 \pm 0.039$ , respectively in the framework of  $\Lambda$ CDM cosmology. The equation of state of dark energy

$w$  is constrained by 14 percent when cluster data is combined with constraints from the external datasets.

### 1.3 Thesis Motivation and Outlook

As shown in Fig. 1.7 and discussed in section 1.2.2, the tightest constraints from galaxy clusters are highly sensitive to the mass bias due to the assumption of HSE used in the estimation of cluster masses. Assuming that the CMB cosmology from Planck is completely independent of any unknown systematics, there are two main possibilities that can result into the bias in the normalization of power spectrum  $\sigma_8$ .

Firstly, higher value of  $\sigma_8$  would theoretically mean larger sample of clusters. Thus, there is a possibility that the cluster selection is dominated by systematics. In other words, we may not be observing a complete sample of galaxy clusters that is resulting into a lower value of  $\sigma_8$  from cluster abundance analysis as compared to that from CMB measurements. Assuming that the mass bias  $1 - b$  is not as high as predicted by joint SZE and CMB analysis as shown in Fig. 1.7, one scenario that I tested in the current work is regarding the contribution of cluster radio galaxies to reduce the detection efficiency of SZE clusters. As SZE detection is based on the suppression of CMB intensity at frequencies lower than 218 GHz thus, the flux from radio sources in clusters can play an important role by raising the flux at these frequencies that can partially or completely erase the SZE signal in CMB sky.

Secondly, I studied the HSE bias  $1 - b$  in the framework of galaxy clusters from a large hydrodynamical simulation. As different observations point to different HSE bias (as shown in right panel of Fig. 1.7), thus it is important to study the contribution of non-thermal pressure in galaxy clusters more extensively in the framework of simulations. In the past few years a lot of attention is offered towards investigations of the galaxy cluster observable-mass scaling relations, where the SZE signature is proportional to the total thermal energy of the ICM. One method is to measure the mass from X-ray observations of the ICM combined with the assumption of HSE and to calibrate the observable-mass relation using these HSE masses. However, it is unlikely that HSE pertains for all systems— particularly those systems having undergone recent major mergers. Indeed, the high fraction of clusters exhibiting merger signatures in the galaxy distribution (Geller & Beers, 1982), the galaxy kinematics (Dressler & Shectman, 1988) and the X-ray emission (Mohr et al., 1995) together with our understanding from simulations of structure formation that galaxy clusters are continually undergoing accretion of new material, suggest that only a small fraction of clusters are in HSE. Some simulation studies suggest that HSE mass measurements are likely to underestimate the true mass by 10-15 percent (e.g. Nagai et al., 2007; Meneghetti et al., 2010). Thus, using these masses will produce misleading conclusions about the observable-mass scaling relation.

Combining these two systematics may shed light on the inconsistency in the cosmology deduced from independent cluster and CMB datasets. Along with these two results, I have presented many other statistical and structural properties of galaxy clusters in the

following three chapters. In the first chapter, I present a study of radio cluster galaxies at unprecedented frequencies to study the incompleteness in SPT-like SZE survey. The cluster sample used for this study spanned low redshift range  $\langle z \rangle = 0.1$ , which made it impossible to study the trends in cluster radio sources with redshift and therefore, its impact on the SZE detection at higher redshifts. In chapter two, I present the mass and redshift trends using most recent sample of galaxy clusters observed in the first year observations of Dark Energy Survey (DES). These trends are further used to study the incompleteness in SZE detected samples. In the third chapter, I present the mass and redshift trends in the cluster pressure profiles along with a universal model that contains these trends with some extra parameters compared to the parametrization described in equations 1.37 and 1.38 by Arnaud et al. (2010). This is done in the framework of large hydrodynamical simulations. The HSE bias is also studied for a large number of simulated clusters. In this chapter, I also present the projection effects in SZE observable-mass relations and provide a first study of the mass and redshift trends in the cluster central offsets.

# Chapter 2

## High Frequency Cluster Radio Galaxies: Luminosity Functions and Implications for SZE Selected Cluster Samples

N. Gupta<sup>1,2,3</sup>, A. Saro<sup>1,2</sup>, J. J. Mohr<sup>1,2,3</sup>, B. A. Benson<sup>4,5,6</sup>, S. Bocquet<sup>5,7,1,2</sup>, R. Capasso<sup>1,2</sup>, J. E. Carlstrom<sup>4,5,7,12,13</sup>, I. Chiu<sup>1,2,14</sup>, T. M. Crawford<sup>4,5</sup>, T. de Haan<sup>8,9</sup>, J. P. Dietrich<sup>1,2</sup>, C. Gangkofner<sup>1,2</sup>, W. L. Holzapfel<sup>8</sup>, M. McDonald<sup>10</sup>, D. Rapetti<sup>1,2</sup>, C. L. Reichardt<sup>11</sup>

<sup>1</sup>Faculty of Physics, Ludwig-Maximilians-Universität, Scheinerstr. 1, 81679 Munich, Germany

<sup>2</sup>Excellence Cluster Universe, Boltzmannstr. 2, 85748 Garching, Germany

<sup>3</sup>Max Planck Institute for Extraterrestrial Physics, Giessenbachstr. 85748 Garching, Germany

<sup>4</sup>Department of Astronomy and Astrophysics, University of Chicago, 5640 South Ellis Avenue, Chicago, IL 60637

<sup>5</sup>Kavli Institute for Cosmological Physics, University of Chicago, 5640 South Ellis Avenue, Chicago, IL 60637

<sup>6</sup>Center for Particle Astrophysics, Fermi National Accelerator Laboratory, Batavia, IL, USA 60510

<sup>7</sup>Argonne National Laboratory, 9700 S. Cass Avenue, Argonne, IL, USA 60439

<sup>8</sup>Department of Physics, University of California, Berkeley, CA 94720

<sup>9</sup>Department of Physics, McGill University, 3600 Rue University, Montreal, Quebec H3A 2T8, Canada

<sup>10</sup>Kavli Institute for Astrophysics and Space Research, Massachusetts Institute of Technology, 77 Massachusetts Avenue, Cambridge, MA 02139

<sup>11</sup>School of Physics, University of Melbourne, Parkville, VIC 3010, Australia

<sup>12</sup>Enrico Fermi Institute, University of Chicago, 5640 South Ellis Avenue, Chicago, IL

60637

<sup>13</sup>Department of Physics, University of Chicago, 5640 South Ellis Avenue, Chicago, IL 60637

<sup>14</sup>Academia Sinica Institute of Astronomy and Astrophysics, Taipei 10617, Taiwan

## 2.1 Abstract

We study the overdensity of point sources in the direction of X-ray-selected galaxy clusters from the Meta-Catalog of X-ray detected Clusters of galaxies (MCXC;  $\langle z \rangle = 0.14$ ) at South Pole Telescope (SPT) and Sydney University Molonglo Sky Survey (SUMSS) frequencies. Flux densities at 95, 150 and 220 GHz are extracted from the 2500 deg<sup>2</sup> SPT-SZ survey maps at the locations of SUMSS sources, producing a multi-frequency catalog of radio galaxies. In the direction of massive galaxy clusters, the radio galaxy flux densities at 95 and 150 GHz are biased low by the cluster Sunyaev-Zel'dovich Effect (SZE) signal, which is negative at these frequencies. We employ a cluster SZE model to remove the expected flux bias and then study these corrected source catalogs. We find that the high frequency radio galaxies are centrally concentrated within the clusters and that their luminosity functions (LFs) exhibit amplitudes that are characteristically an order of magnitude lower than the cluster LF at 843 MHz. We use the 150 GHz LF to estimate the impact of cluster radio galaxies on an SPT-SZ like survey. The radio galaxy flux typically produces a small bias on the SZE signal and has negligible impact on the observed scatter in the SZE mass-observable relation. If we assume there is no redshift evolution in the radio galaxy LF then  $1.8 \pm 0.7$  percent of the clusters with detection significance  $\xi \geq 4.5$  would be lost from the sample. Allowing for redshift evolution of the form  $(1+z)^{2.5}$  increases the incompleteness to  $5.6 \pm 1.0$  percent. Improved constraints on the evolution of the cluster radio galaxy LF require a larger cluster sample extending to higher redshift.

## 2.2 Introduction

The first galaxy cluster sample selected through the Sunyaev-Zel'dovich Effect (SZE; Sunyaev & Zel'dovich, 1972) emerged in the last decade (Staniszewski et al., 2009); since then, high frequency mm-wave surveys by the South Pole Telescope (SPT; Carlstrom et al., 2011), the Atacama Cosmology Telescope (ACT; Fowler et al., 2007), and Planck (Planck Collaboration et al., 2011) have enabled the SZE selection of large cluster samples and their use to constrain cosmological parameters (Vanderlinde et al., 2010; Sehgal et al., 2011; Benson et al., 2013; Reichardt et al., 2013; Hasselfield et al., 2013; Bocquet et al., 2015; Planck Collaboration et al., 2015a; de Haan et al., 2016). In these analyses the connection between the cluster SZE signature and the underlying halo mass – the so-called mass-observable relation – plays a central role. Emission from cluster radio galaxies will contaminate the cluster SZE signature at some level, resulting in incompleteness in the SZE selected cluster samples and contributing to the scatter in the SZE mass-observable relation. Although

previous studies indicate that these effects are small at high frequencies (Lin & Mohr, 2007; Lin et al., 2009; Sehgal et al., 2010; Lin et al., 2015), these studies all rely to some degree on extrapolations from the properties of radio galaxies at low frequencies.

One way to study this phenomenon more directly is to statistically examine the radio galaxy population using a cluster sample selected in a manner that would be unaffected by galaxy radio emission. In this work we carry out the first such study at high frequencies, constructing the cluster radio galaxy luminosity function (LF) from the overdensity of point sources in the SPT-SZ survey (Carlstrom et al., 2011; Bleem et al., 2015) and the Sydney University Molonglo Sky Survey (SUMSS Bock et al., 1999; Mauch et al., 2003; Murphy et al., 2007) toward galaxy clusters in the Meta-Catalog of X-ray detected Clusters of galaxies (MCXC, Piffaretti et al., 2011).

The measurement of the LF is not straightforward at the 95 and 150 GHz SPT observing frequencies, because of the presence of the negative SZE signature at these frequencies. The cluster SZE signature biases our radio galaxy flux measurements, and could indeed remove point sources from a high frequency selected sample. Thus, to estimate the true underlying radio galaxy flux, one must estimate the cluster SZE flux at the positions of these point sources and then use that to correct the radio galaxy fluxes. These corrections will lead to additional point sources in a flux limited sample and are therefore crucial for the LF analysis. We use the SUMSS radio galaxies, observed at 843 MHz, to enable this correction and the construction of unbiased radio galaxy samples. Specifically, we measure the SPT point source fluxes at the locations of all SUMSS radio galaxies and apply an estimated SZE correction. Using this corrected catalog we then measure the LFs and use that information to estimate the impact of the cluster radio galaxies on cluster samples selected using high frequency observations of the SZE.

The plan of the paper is as follows: In section 3.3, we discuss the observations and the data used in this work and describe the corrections applied to the point source catalogs at 95 and 150 GHz. Section 3.4 is dedicated to the studies of surface density profiles and the LFs. In section 3.5 we estimate the contamination by radio galaxies in SZE cluster surveys. Section 2.6 describes the effect of cluster mass and point source flux uncertainties on our results. We conclude in section 4.7. Throughout this paper we assume a flat  $\Lambda$ CDM cosmology with matter density parameter  $\Omega_M = 0.3$  and Hubble constant  $H_0 = 70 \text{ km s}^{-1} \text{ Mpc}^{-1}$ . We take the normalization of the matter power spectrum to be  $\sigma_8 = 0.83$ .

## 2.3 Data and Radio Galaxy Flux Corrections

We study the overdensity of radio point sources in the direction of galaxy clusters in the MCXC. The radio sources are selected from the SUMSS catalog observed at 843 MHz and SPT observations are used to measure the source fluxes at higher frequencies. We discuss these observations in the following sections. At 95 and 150 GHz frequencies, the source fluxes in clusters can be biased by their SZE flux. Taking this into account we construct an unbiased catalog of SUMSS sources at high frequencies using the independently detected SPT point source catalog as well as SPT-SZ maps, as described in section 3.3.4.

### 2.3.1 SPT Observations

The South Pole Telescope (SPT) is a 10-meter telescope located at the Amundsen-Scott South Pole station in Antarctica (Carlstrom et al., 2011). The 2500 deg<sup>2</sup> SPT-SZ survey has coverage in multiple frequency bands centered around 95, 150 and 220 GHz, corresponding to wavelengths of 3.2, 2.0 and 1.4 mm, respectively. The SPT angular resolution at these three frequencies is approximately 1.6, 1.1 and 1.0 arcmin, and the survey depths are approximately 40, 18 and 70  $\mu$ K-arcmin, respectively.

The data reduction procedure for SPT is described in detail elsewhere (Staniszewski et al., 2009; Vieira et al., 2010; Schaffer et al., 2011; Mocanu et al., 2013). To increase the signal-to-noise ratio ( $S/N$ ) of unresolved objects a matched filter  $\psi$  (Tegmark & de Oliveira-Costa, 1998) of the following form is generated

$$\psi \equiv \frac{\tau^T N^{-1}}{\sqrt{\tau^T N^{-1} \tau}}, \quad (2.1)$$

where  $\tau$  is the source shape, which is a function of the beam and filtering, and  $N$  is the noise covariance matrix, which also includes astrophysical contaminants like primary CMB anisotropy along with the instrument and atmospheric noise. The purpose of this filtering is to increase the sensitivity of the beam size objects by down-weighting signal from larger and smaller scales where the  $S/N$  is small.

Sources in the filtered SPT-SZ maps were identified using the CLEAN algorithm (Högbom, 1974). We again refer the reader to Vieira et al. (2010) and Mocanu et al. (2013) for details about the implementation of the CLEAN algorithm to the SPT maps. The flux of the identified sources is calculated from the filtered maps by converting the value of the brightest pixel across the sources from the units of CMB fluctuation temperature to the flux as follows

$$S[\text{Jy}] = T_{\text{peak}} \cdot \Delta\Omega_f \cdot 10^{26} \cdot \frac{2k_B}{c^2} \left( \frac{k_B T_{\text{CMB}}}{h} \right)^2 \frac{x^4 e^x}{(e^x - 1)^2}, \quad (2.2)$$

where  $x = h\nu/(k_B T_{\text{CMB}})$ ,  $T_{\text{peak}}$  is the peak temperature in a pixel,  $k_B$  is the Boltzmann constant,  $c$  is the velocity of light,  $T_{\text{CMB}}$  is the present CMB temperature,  $h$  is the Planck constant and  $\Delta\Omega_f$  is the effective solid angle under the source template. There are 4841 point sources detected by SPT above a  $S/N$  of 4.5 in any of the three frequency bands (Everett et al. in, prep). Of these, we expect  $\sim 80$  percent to have synchrotron dominated emission and the rest to be dusty galaxies, consistent with the findings in the analysis of 771 deg<sup>2</sup> of the SPT-SZ survey (Mocanu et al., 2013).

### 2.3.2 SUMSS Catalog

The Sydney University Molonglo Sky Survey (SUMSS, Bock et al., 1999; Mauch et al., 2003; Murphy et al., 2007) imaged the southern radio sky at 843 MHz with a characteristic angular resolution of  $\sim 45''$  using the Molonglo Observatory Synthesis Telescope (MOST, Mills, 1981; Robertson, 1991). The survey was completed in early 2007 and covers 8100

deg<sup>2</sup> of sky with  $\delta \leq -30^\circ$  and  $|b| \geq 10^\circ$ . The catalog contains 210,412 radio sources to a limiting peak brightness of 6 mJy beam<sup>-1</sup> at  $\delta \leq -50^\circ$  and 10 mJy beam<sup>-1</sup> at  $\delta > -50^\circ$ . At the SUMSS selection frequency, we expect nearly all sources above the flux selection threshold to be synchrotron dominated (de Zotti et al., 2005). The position uncertainties in the catalog are always better than 10". In fact, for sources with peak brightness  $A_{843} \geq 20$  mJy beam<sup>-1</sup>, the accuracy is in the range 1" to 2". The flux measurements are accurate to within 3 percent. The catalog is complete to 8 mJy at  $\delta \leq -50^\circ$  and to 18 mJy at  $\delta > -50^\circ$ . There are approximately 56,000 SUMSS sources in the SPT region at 100 percent completeness. As shown by Mocaanu et al. (2013) in an analysis of 720 deg<sup>2</sup> of the SPT region, only  $\sim 4$  percent of synchrotron dominated SUMSS sources are extended at the SPT angular resolution. At the SUMSS frequency, approximately 10 percent of the sources exhibit extent along one axis (Mauch et al., 2003).

### 2.3.3 MCXC Catalog

For our analysis, we use the Meta-Catalog of X-ray detected Clusters of galaxies (MCXC, Piffaretti et al., 2011), which is compiled from the publicly available ROSAT All Sky Survey-based catalogs, such as, NORAS (Böhringer et al., 2000), REFLEX (Böhringer et al., 2004), BCS (Ebeling et al., 1998, 2000), SGP (Cruddace et al., 2002), NEP (Henry et al., 2006), MACS (Ebeling et al., 2001), CIZA (Ebeling et al., 2002; Kocevski et al., 2007) and serendipitous catalogs such as, 160SD (Mullis et al., 2003), 400SD (Burenin et al., 2007), SHARC (Romer et al., 2000), WARPS (Perlman et al., 2002; Horner et al., 2008), and EMSS (Gioia & Luppino, 1994; Henry, 2004). The catalog contains a total of 1,743 clusters in the whole sky. The cluster coordinates are those of the cluster centroid determined from X-ray data (apart from the 47 clusters in the sub-catalog EMSS (Gioia & Luppino, 1994) which have the coordinates of the cluster optical position). The masses are estimated from the homogenized luminosities using the power law relation described in Piffaretti et al. (2011). The redshift range of the MCXC catalog spans from 0.003 to 1.26 with a median of 0.14, and the mass range is  $9.6 \times 10^{11} M_\odot \leq M_{500} \leq 2.2 \times 10^{15} M_\odot$  with a median mass of  $1.76 \times 10^{14} M_\odot$ . Here  $M_{500}$  describes the mass of the cluster within the sphere where the density is 500 times the critical density of the Universe. We use an NFW profile with the expected concentration from large scale structure simulations to convert from  $M_{500}$  to  $M_{200}$  (Duffy et al., 2008; Navarro et al., 1997).

There are 139 and 333 MCXC clusters in the SPT-SZ and SUMSS regions, respectively. In the SPT-SZ region these systems span a mass range  $6.5 \times 10^{12} M_\odot \leq M_{500} \leq 1.2 \times 10^{15} M_\odot$  with a median mass of  $1.5 \times 10^{14} M_\odot$ . In the SUMSS region the corresponding mass range and median mass are  $6.5 \times 10^{12} M_\odot \leq M_{500} \leq 1.2 \times 10^{15} M_\odot$  and  $1.8 \times 10^{14} M_\odot$ , respectively. The median redshift for both samples is  $z \sim 0.1$ , and the highest redshift system is at  $z = 0.686$ . So, using the MCXC cluster sample to identify cluster radio galaxies allows us to examine primary low redshift systems that cover the mass range from groups to clusters.

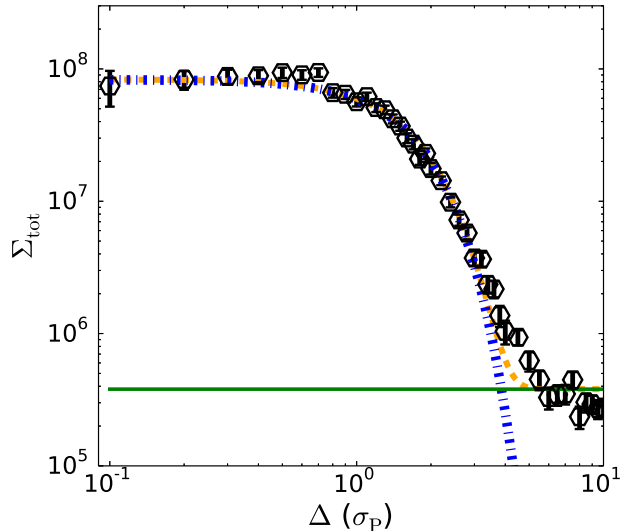


Figure 2.1: Distribution of offsets between SUMSS and SPT point sources in units of the total positional uncertainty  $\sigma_P$ . Lines represent best fit level of random associations (green), Gaussian core (blue) and core plus random (orange). We limit matches to lie within  $5\sigma_P$  and estimate only 3 percent of those are random associations.

### 2.3.4 Catalog of Cluster Radio Galaxy Candidates

The intrinsic flux of a point source residing along the line of sight to a galaxy cluster is biased by the cluster SZE flux. The SZE flux corrections are expected to be small for non-central sources, but when one defines a radio galaxy sample using a flux limit the presence of this SZE flux bias inevitably means that some sources that should be in the flux limited catalog will drop out of it. Thus, we employ the SUMSS catalog in building a catalog of high frequency radio galaxies.

As described in the following sections, this requires matching the SUMSS and SPT catalogs for the subset of radio galaxies that are bright enough to have made it into the SPT catalog and extracting a flux measurement directly from the appropriately filtered SPT maps for the rest of the sources. We describe here the results of the catalog matching, the SZE flux bias correction and then the characteristics of the final analysis-ready SUMSS selected catalog at SPT frequencies.

#### Matching SUMSS and SPT Sources

The  $S/N$  and fluxes of 4,841 SPT detected point sources are measured at 95, 150 and 220 GHz with the methodology described in section 3.3.1. The positional uncertainty  $\sigma_{\text{SPT}}$  along one dimension of these point sources depends upon the  $S/N$  of the sources as well

as the beam size  $\sigma_F$  (Ivison et al., 2007), where  $\text{FWHM} = \sqrt{8 \ln 2} \sigma_F$ , and is given by

$$\sigma_{\text{SPT}} = \sqrt{2} \frac{\sigma_F}{S/N}. \quad (2.3)$$

We choose the smallest value of  $\sigma_{\text{SPT}}$  out of the three SPT bands as the positional uncertainty of each point source.

To select the radio galaxy population, we look for the SUMSS counterparts within a region of radius  $5\sigma_p$  around the SPT selected point sources, where  $\sigma_p$  is the quadrature sum of the SPT and SUMSS positional uncertainties

$$\sigma_p^2 = \sigma_{\text{SPT}}^2 + \sigma_{\text{SUMSS}}^2. \quad (2.4)$$

We choose the  $5\sigma_p$  limit to search for SUMSS counterparts, because the surface density of the SUMSS sources within distance  $\Delta\sigma_p$  of SPT point sources drop to a uniform background level at  $\Delta\sigma_p \sim 5$  (see Fig. 2.1). We find 3,558 (72 percent) of the SPT detected point sources to have SUMSS counterparts. This fraction is similar to the 71 percent of sources with SUMSS counterparts found by Mocanu et al. (2013) in the first 771 deg<sup>2</sup> of the SPT-SZ region.

We fit a Gaussian model along with a constant background to the surface density profile of SUMSS sources in SPT as shown in Fig. 2.1. Using this fit we estimate that the purity of the sample selected within  $5\sigma_p$  is 97 percent.

### SZE Flux Bias and Correction

The flux of sources in the direction of galaxy clusters is suppressed by the negative SZE signature. Thus, to recover the true flux we need to correct for the SZE flux bias. To do this, we first create an SZE map of the overlapping cluster using a circularly symmetric Compton  $Y$  profile (Arnaud et al., 2010) extending to a radius  $5R_{200}$ , appropriate for a cluster of the mass given in the MCXC catalog. Specifically, SZE maps with the same pixel size as the SPT maps are created by scaling the  $Y$  signal in a pixel by the pixel area. We then filter these cluster maps using the matched filter technique for unresolved sources as discussed in section 3.3.1.

The filtered mock SZE maps of the galaxy clusters give us the peak temperature of an unresolved source as a function of position within the cluster. We translate this into the flux using equation (2.2). The SZE flux extracted from the filtered mock maps is then used to boost the observed point source flux. This flux correction depends upon the position of the point source in the cluster as well as the mass and the redshift of the cluster.

As the angular size of a cluster decreases with redshift, a larger fraction of its SZE signature lies within a single SPT beam, and the angular distance of a cluster radio galaxy from the cluster center decreases. For both these reasons the SZE flux bias correction tends to grow with redshift. For example, two clusters with masses  $M_{500} \sim 4.3 \times 10^{14} M_\odot$  that are at redshifts  $z = 0.075$  and  $z = 0.175$  have 150 GHz SZE flux corrections of 6.41 mJy and 8.61 mJy, respectively, for a point source residing at their centers. This flux is 1.2 percent and 7.3 percent of the total SZE flux in their  $\theta_{500}$  regions.

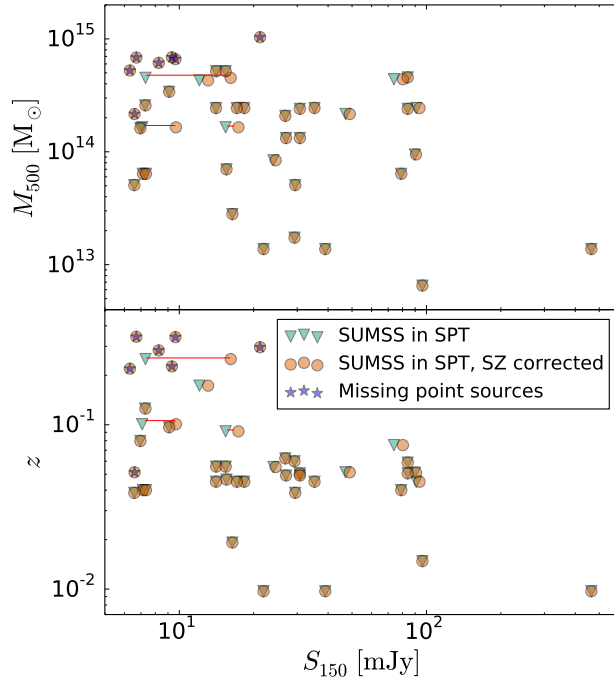


Figure 2.2: SPT 150 GHz flux versus cluster redshift (bottom) and mass (top) for SUMSS selected radio galaxies with  $S_{150} > 6$  mJy that lie in the projected  $\theta_{200}$  regions of clusters from the MCXC X-ray selected cluster catalog. Green (brown) points show fluxes before (after) SZE flux corrections. The SZE flux correction, in general, is larger for high mass and distant clusters compared to the low mass and nearby clusters, ranging between 0 and 24 mJy. Seven radio galaxies that would not have made the SPT flux cut because of the SZE flux bias from their host galaxy clusters are marked with stars.

It is important to note that the correction is only an approximation to the true flux bias, because there will in general be departures between the true (unobserved) Compton  $Y$  profile of the cluster and the model we employ. Nevertheless, because the true observed Compton  $Y$  profiles of clusters have been shown to be in reasonably good agreement with the X-ray derived profiles (Plagge et al., 2010), this correction should be approximately correct in the mean as applied to an ensemble of cluster radio galaxies for a statistical study. We will discuss the systematics of this flux correction more in section 2.6.2.

We note that as a result of the frequency dependent factor in equation (2.2), the SZE flux corrections at 150 GHz are 1.8 times larger than those at 95 GHz, for a fixed solid angle. However, the SZE flux corrections to the point sources at 95 GHz are found to be on average larger than the corrections at 150 GHz. This is due to the larger beam size at 95 GHz, which results in a 2.2 times larger effective solid angle for point sources ( $\Delta\Omega_f$  in equation 2.2) at 95 GHz than at 150 GHz.

### SUMSS Based SPT 6 mJy Flux Limited Sample

We focus on the locations of the SUMSS sources in the SPT 95, 150 and 220 GHz maps. To build a flux limited radio galaxy catalog at SPT observing frequencies, we first check for a counterpart in the SPT detected point source sample using the method described in section 2.3.4. Because both position and flux were determined simultaneously for the SPT detected point sources, the SPT fluxes must be corrected to account for the resulting flux bias as

$$S \text{ [mJy]} = \sigma_N \sqrt{\xi^2 - 2}, \quad (2.5)$$

where  $\sigma_N$  is the noise in the map and peak  $\xi$  is the filtered  $S/N$  measured at the SPT location of the source. If there is no counterpart in the SPT selected sample, we go to the CLEANed SPT maps and estimate the SPT flux at the position of the SUMSS source. The CLEANed SPT maps are those where all sources with  $S/N$  ( $\xi$ ) greater than 4.5 have been removed. These maps are less affected by artifacts associated with bright point sources.

In the SPT region, our sample contains 55,884 SUMSS sources above the completeness limits presented in section 3.3.2. Above a flux limit of 6 mJy at 150 GHz, we find 2,970 sources in the SPT point source catalog, but after the flux debiasing we find 2,693 SPT counterparts of SUMSS sources above 6 mJy. There are 37 sources above a flux limit of 6 mJy in the SPT detected catalog within the  $\theta_{200}$  of the MCXC clusters. In the SUMSS selected catalog there are 36 sources with flux above 6 mJy overlapping the MCXC clusters. The SPT selected sample has a single extra point source, which lies just outside the cluster  $\theta_{200}$  boundary according to its SUMSS position but just inside according to the SPT position. Interestingly, this point source also has larger flux at 150 GHz as compared to 95 GHz and 843 MHz observing frequencies, indicating that it is possibly an SFG.

We then apply the SZE flux corrections at 95 and 150 GHz for all the sources which are inside the MCXC clusters, using the method described in the last sub-section. The number of candidate cluster radio galaxies increases to 43 after the SZE flux correction. Thus, we recover 7 additional sources, which were otherwise missing due to the SZE flux bias at 150 GHz. Having a closer look at these sources, we find that all but one of these sources have negative fluxes before the SZE flux correction and are present in the central pixels of massive MCXC clusters, which are also counterparts of SPT confirmed galaxy clusters. One of the sources residing in a low redshift cluster has an SZE flux correction of around 4 mJy, which boosts it into the 6 mJy sample. These 43 SUMSS sources recovered in SPT maps at 150 GHz are shown in Fig. 2.2 with the mass and redshift information of the host clusters. Each point with its uncorrected flux is shown in green and with its corrected flux in brown. The seven point sources recovered from the SUMSS catalog after the SZE flux correction are marked with a star, and in these cases we do not show the uncorrected flux.

### 2.3.5 Radio Galaxy Spectral Indices

Following the technique in Saro et al. (2014), we use a maximum likelihood analysis to estimate the spectral index ( $\alpha$ ) of different samples of radio galaxies using different com-

Table 2.1: The characteristic spectral indices and  $1\sigma$  uncertainties for all SUMSS detected sources in the SPT region and a subset of these, which we denote as BCGs, that lie within  $0.1 \times \theta_{200}$  of the MCXC cluster centers. Mean spectral indices are presented for pairs of frequencies constructed from 150 GHz, 95 GHz and 843 MHz. The SZE correction is applied at 95 and 150 GHz.

Dataset	$\alpha_{0.843}^{150}$	$\alpha_{0.843}^{95}$	$\alpha_{95}^{150}$
SUMSS	$-0.38^{+0.28}_{-0.29}$	$-0.38^{+0.28}_{-0.31}$	$-0.50^{+0.24}_{-0.23}$
SUMSS BCGs	$-0.63^{+0.34}_{-0.29}$	$-0.64^{+0.33}_{-0.40}$	$-0.77^{+0.32}_{-0.31}$

binations of fluxes  $S$  as

$$\mathcal{L}(\alpha) \propto \prod_{i=1}^{N_{\text{source}}} \exp \left( -\frac{1}{2} \frac{\left( S_{\nu_1}^{(i)} R(\alpha) - S_{\nu_2}^{(i)} \right)^2}{\left( \Delta S_{\nu_1}^{(i)} R(\alpha) \right)^2 + \left( \Delta S_{\nu_2}^{(i)} \right)^2} \right), \quad (2.6)$$

where  $S_{\nu_1}^{(i)}$  ( $\Delta S_{\nu_1}^{(i)}$ ) and  $S_{\nu_2}^{(i)}$  ( $\Delta S_{\nu_2}^{(i)}$ ) is the flux (flux uncertainty) of the  $i^{\text{th}}$  source at 0.843 and 95 GHz, respectively, for the estimation of  $\alpha_{0.843}^{95}$  (similarly for  $\alpha_{0.843}^{150}$  and  $\alpha_{95}^{150}$ ).  $R(\alpha)$  is given by

$$R(\alpha_{\nu_1}^{\nu_2}) = \left( \frac{\nu_2}{\nu_1} \right)^{\alpha_{\nu_1}^{\nu_2}}. \quad (2.7)$$

As already mentioned in section 3.3.2, 90 and 96 percent of sources are unresolved at SUMSS and SPT frequencies, respectively. For the remaining sources, our spectral index measurements could be affected by additional systematic uncertainties.

The most likely values of  $\alpha_{0.843}^{95}$ ,  $\alpha_{0.843}^{150}$  and  $\alpha_{95}^{150}$  are listed in Table 2.1 for all SUMSS sources in the SPT-SZ region and for sources projected near the centers of the MCXC clusters, which we term BCGs (Brightest Cluster Galaxies). The SZE flux correction is applied to the source fluxes at 95 and 150 GHz. There is a tendency for the spectra to steepen with frequency, and the central sources (BCGs) tend to exhibit steeper spectra than the typical radio galaxies in the field.

Similar spectral indices (within our quoted error bars for central sources/BCGs in MCXC clusters) were found by Lin & Mohr (2007) where they used the NRAO VLA Sky Survey (NVSS, Condon et al., 1998) 1.4 GHz data together with the 4.85 GHz data from the GB6 (Green Bank 6 cm survey, Gregory et al., 1996) and PMN (Parkes-MIT-NRAO survey, Griffith & Wright, 1993). They reported  $\alpha_{1.4}^{4.85} = -0.51$  for most of the sources in the cluster, and they also found steeper spectra for BCGs in their sample. Our results are also consistent with other previous analyses (Condon, 1992; Cooray et al., 1998; Coble et al., 2007).

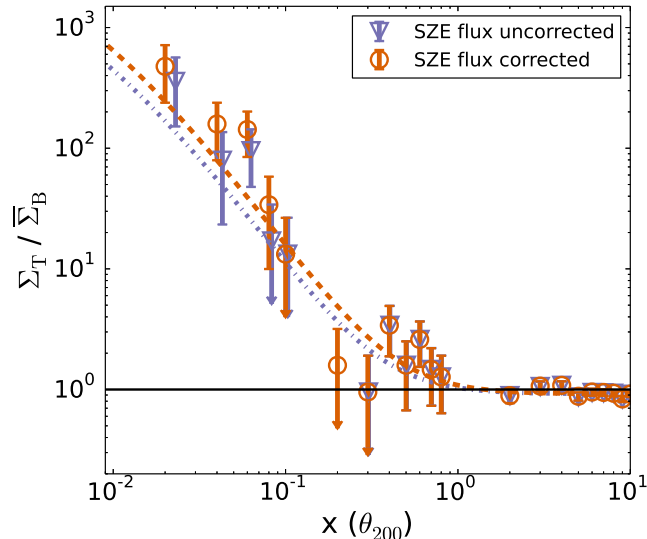


Figure 2.3: Surface density profiles for two flux limited  $S_{150} > 6$  mJy samples of radio galaxies stacked within 139 MCXC clusters. Both samples with SZE flux corrections (red) and without (blue) are shown. The lines are the best fit NFW models (see Table 3.1).

## 2.4 Results

In this section we use the flux limited samples of radio point sources to first study the radial profile of high frequency cluster radio galaxies and to then study the LF. A radial profile is needed for the deprojection of the measured LF into the cluster virial volume.

### 2.4.1 Radial Distribution of Cluster Radio Galaxies

We examine the distribution of radio galaxies in the cluster virial region by stacking all radio galaxies overlapping the MCXC sample in the coordinate  $\theta/\theta_{200}$ . We use the projected NFW profile (Navarro et al., 1997) as a fitting function for the radial distribution, where the projected profile can be written as (Bartelmann, 1996):

$$\Sigma(x) = \frac{2\rho_s r_s}{x^2 - 1} f(x), \quad (2.8)$$

with  $\rho_s = \rho_c \delta_c$  (where  $\rho_c$  is the critical density of the Universe and  $\delta_c$  is a characteristic density contrast),  $r_s$  is the typical profile scale radius and  $f(x)$  is given by

$$f(x) = \begin{cases} 1 - \frac{2}{\sqrt{x^2-1}} \arctan \sqrt{\frac{x-1}{x+1}} & \text{if } x > 1, \\ 1 - \frac{2}{\sqrt{1-x^2}} \operatorname{arctanh} \sqrt{\frac{1-x}{x+1}} & \text{if } x < 1, \\ 1/3 & \text{if } x = 1. \end{cases}$$

Here  $x = r/r_s$  and  $r_s = R_{200}/c$ , where  $c$  is the concentration parameter. Following Lin et al. (2004), we remodel the projected NFW profile by integrating over equation (2.8) and

get the projected number of galaxies

$$N(x) = \frac{N_{200}}{g(c)}g(x), \quad (2.9)$$

where the normalization  $N_{200}$  is the number of galaxies projected in the cluster virial radius  $R_{200}$  and  $g(x)$  is given as

$$g(x) = \int_0^x \frac{x' f(x')}{(x'^2 - 1)} dx', \quad (2.10)$$

where  $x$  is equivalent to  $c$  for  $r = R_{200}$  to give  $g(c)$ . This reduces the covariance between the normalization and concentration parameters of the NFW profile.

The surface density of the clusters can have both cluster and background components and is written as

$$\Sigma_T = \Sigma(x) + \Sigma_B, \quad (2.11)$$

and in terms of the number of galaxies as

$$N_T = N(x) + \Sigma_B A, \quad (2.12)$$

where  $A$  is the solid angle of the annulus or bin. Thus we fit our stacked distribution of radio galaxies to a model with three parameters:  $c$ ,  $N_{200}$  and  $\Sigma_B$ . We stack radio galaxies out to  $10 \times \theta_{200}$  to allow for a good constraint on the background density  $\Sigma_B$ .

We employ the Cash (1979) statistic

$$C = \sum_i (N_{T,i}^d \ln(N_{T,i}^m) - N_{T,i}^m - N_{T,i}^d \ln(N_{T,i}^d) + N_{T,i}^d), \quad (2.13)$$

in this fit, where  $N_{T,i}^m$  is the total number of galaxies from the model as in equation (3.3) and  $N_{T,i}^d$  is the total number of galaxies in the observed data in the  $i^{\text{th}}$  angular bin. This is just the difference in  $N(x)$  evaluated at the outer and inner boundaries of each bin.

We use the Markov Chain Monte Carlo (MCMC) code, **emcee** (a Python implementation of an affine invariant ensemble sampler; Foreman-Mackey et al., 2013) to fit the model to the data for two different datasets: (1) the SUMSS based sample of radio galaxies with uncorrected fluxes, and (2) the sample with SZE flux corrections. In the fitting we adopt a bin size corresponding to  $\theta_{200}/1000$  and fit over the region extending to  $10\theta_{200}$ . The concentration parameter is sampled in log space during the fit.

The best fit values and uncertainties of the parameters for different datasets are given in Table 3.1. The background subtracted number of galaxies  $N_{200}$  in the stack of 139 galaxy clusters is  $\sim 30$  ( $\sim 20$ ) in the SZE flux corrected (uncorrected) sample. There is an increase in the normalization  $N_{200}$  in going from the sample with uncorrected fluxes to the SZE bias corrected sample of approximately 50 percent, because the SZE flux bias correction only affects sources lying projected onto the cluster virial region, and the additional sources that come into the flux limited sample are predominantly cluster radio galaxies.

$\Sigma_B$  is the background density [ $\text{deg}^{-2}$ ] which can be multiplied by the total solid angle ( $\simeq 20.5 \text{ deg}^2$ ) of the cluster stack within  $\theta_{200}$  to get an estimate of the number of background

Table 2.2: Best fit NFW model parameters for the radial profile of radio galaxies with  $S_{150} \geq 6$  mJy in a stack of 139 MCXC clusters. The samples with uncorrected and SZE corrected fluxes are shown, and for each we present concentration  $c$ ,  $N_{200}$ , background density  $\Sigma_B$ , and the number of sources  $\bar{N}_T$  within  $\theta_{200}$ .

Dataset	$c$	$N_{200}$	$\Sigma_B$ [deg $^{-2}$ ]	$\bar{N}_T$
Flux uncorrected	$107_{-51}^{+277}$	$19.7_{-4.8}^{+5.7}$	$0.94 \pm 0.02$	36
Flux corrected	$108_{-48}^{+107}$	$28.7_{-5.6}^{+6.2}$	$0.94 \pm 0.02$	43

galaxies.  $\bar{N}_T$  is the total number of galaxies within  $\theta_{200}$  of the stacked clusters above our flux limit of 6 mJy, and this is close to the sum of  $N_{200}$  and the number of background galaxies obtained from the fit. Because  $N_{200}$  is evaluated from a stack of clusters, we have between 0.15 and 0.20 radio galaxies per cluster. If we sum the virial masses of the MCXC clusters we then have between 0.5 and 0.75 radio galaxies per  $10^{15}M_\odot$  of cluster mass. The profile is strongly centrally concentrated with  $c \sim 100$ , indicating that the radial distribution of cluster radio galaxies is consistent with a power law distribution  $n(r) \propto r^{-3}$ . We use this behavior in the next section to correct the projected LF to the LF within the cluster virial region defined by  $r_{200}$ .

In Fig. 3.2 we show the best fit surface density profiles and data for each of the two datasets. To create these plots we combined many bins to reduce the noise in the measured radial profile. We normalize the  $y$ -axes of this plot with the annulus area in each angular bin and the background level density or the mean number density of sources ( $\bar{\Sigma}_B$ ) in the SPT region so that we can compare the surface density profiles from the two datasets. It is worth noting that  $\bar{\Sigma}_B$  is not same as the background density ( $\Sigma_B$ ), where the latter is one of the fit parameters. However, Fig. 3.2 shows that the mean survey density is a good estimation of the background number density of the clusters, as  $\Sigma_T/\bar{\Sigma}_B$  is consistent with 1 outside of the cluster.

## 2.4.2 Cluster Radio Galaxy Luminosity Functions

In this section, we construct radio LFs using the excess of radio sources toward galaxy clusters and assigning those excess sources to the cluster redshift (following Lin et al., 2004). We calculate the LFs not only for the SPT bands but also for the SUMSS band. We compute the radio luminosity of the SUMSS point sources overlapping the MCXC galaxy clusters using the observed fluxes (before and after SZE correction) and the redshift of the respective cluster. In the luminosity calculations we apply the redshift dependent  $k$ -correction in an attempt to estimate the luminosity at the same rest frame frequency for all redshifts. Thus the radio source luminosity is given by:

$$P_{\nu_s} = (4\pi D_L^2) S_{\nu_s} \frac{k(z)}{(1+z)}, \quad (2.14)$$

where  $D_L$  is the luminosity distance to the redshift  $z$  of the cluster,  $S_{\nu_S}$  is radio source flux at frequency  $\nu_S$  and  $k(z)$  is the  $k$ -correction given by  $(1+z)^{-\alpha}$ . We choose a spectral index  $\alpha = -0.8$  for the 843 MHz analysis and an  $\alpha = -0.5$  for the higher frequency analyses (see Table 2.1 for results at higher frequency). We notice that the choice of spectral index has insignificant impact on the luminosity measurements and confirm that the modeling of LFs will be independent of the choice of  $\alpha$ .

### LF Fitting Method

To construct the LF we consider all the MCXC clusters that lie in the SPT (or SUMSS) region, adding up the number of point sources within  $\theta_{200}$  in different logarithmic luminosity bins (effectively placing all radio galaxies at the redshift of the cluster). For each luminosity bin, we estimate the background counts from the population of observed sources in the SPT (or the SUMSS) region, in the corresponding bins in  $\log N - \log S$  space, where we use the cluster redshift to transform from radio galaxy flux to luminosity. These background counts are corrected for the surface area of all the clusters in our sample. We also keep track of the total mass  $\Sigma M_{200}$  of the clusters, which are contributing to each of the luminosity bins. We use this vector of total masses to normalize our LF, allowing us to account for the fact that with a particular flux limit the high redshift cluster radio galaxies do not extend to as faint a luminosity as those in the low redshift clusters. Another way is to normalize it with the total volume of these clusters. However, doing so introduces a redshift dependence in the LF as we define the virial region  $\theta_{200}$  as the region with an overdensity of 200 times the critical density of the universe at that redshift, and the critical density scales as  $E^2(z)$ . Thus, normalizing by total mass is a good choice, because if the AGN activity were independent of redshift we would expect to see the same LF defined as the number of galaxies per unit mass at all redshifts. In addition, this normalization facilitates comparison of the field and cluster LFs to determine whether AGN activity depends on environment.

To fit the LF we again use MCMC analysis with the Cash statistic as described in equation 3.4. We first attempt to fit a Schechter function (Schechter, 1976), but this is a poor fit to the data. Thus we take the functional form used in Condon et al. (2002) for our fits. The LF model is

$$\log \left( \frac{dn}{d \log P} \right) = y - \left[ b^2 + \left( \frac{\log P - x}{w} \right)^2 \right]^{1/2} - 1.5 \log P, \quad (2.15)$$

where the parameters  $b$ ,  $x$  and  $w$ , control the shape of the LF and  $y$  is its amplitude. The LF shape parameters are determined in Condon et al. (2002) for AGN and star forming galaxies (SFGs) at low frequency and for the field population. The shape parameters are  $(b_1, x_1, w_1) = (2.4, 25.8, 0.78)$  for the AGN and  $(b_2, x_2, w_2) = (1.9, 22.35, 0.67)$  for the SFGs. To evaluate the likelihood of a given model, we take the LF model and scale by the total mass of the sample of clusters contributing to each luminosity bin and then add the background number of galaxies determined from the data for that bin. That is, we do

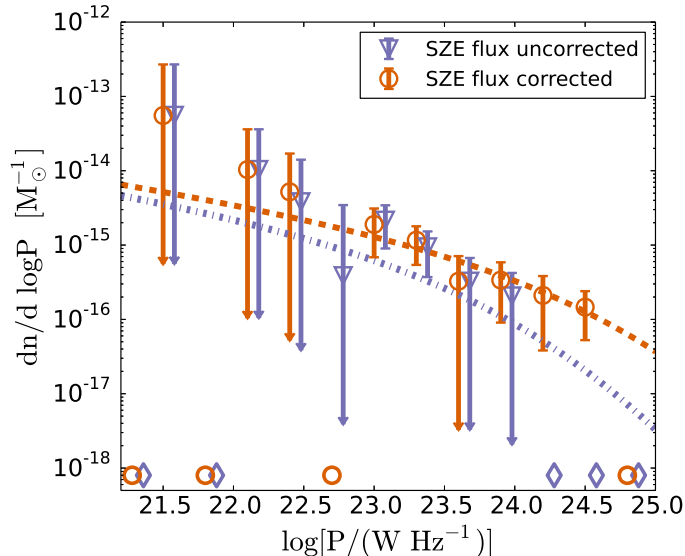


Figure 2.4: The 150 GHz LF for sources within  $\theta_{200}$  of the centers of massive galaxy clusters. This LF is derived from the SUMSS selected sample in the SPT region with (red) and without (blue) SZE flux corrections. Lines are the best fitting LF models. The increase in LF amplitude on the high luminosity end when using the SZE flux bias corrected sample is clear. For convenience in this figure the bins containing negative values in the background subtracted counts are represented as points at the bottom of the figure.

not fit to the background subtracted counts. We validate our code by analyzing simulated samples created using the best fit LFs reported below, demonstrating that we recover the input parameters.

We scale the LF amplitude to account for cluster radio galaxies projected onto the virial cylinder but not lying in the virial sphere; this deprojection correction  $D_{\text{prj}}$  has a very small impact for the radio galaxy case, because the radial distributions are so centrally concentrated. Specifically,  $D_{\text{prj}} = 0.92$  for an NFW concentration of 108, which is the best fit value listed in Table 3.1. The  $2\text{-}\sigma$  excursion from the mean concentration to lower (34) and upper (460) values correspond to deprojection values of 0.9 and 0.94, respectively, and thus the uncertainty on the concentration does not impact our LF measurements significantly.

Following Lin & Mohr (2007), we first fit the sum of the AGN and SFGs Condon et al. (2002) models to the SUMSS data above the completeness limits at 843 MHz by allowing the amplitudes ( $y_1$  and  $y_2$ ) and x-axis scales ( $x_1$  and  $x_2$ ) to vary, while fixing the other shape parameters of the function. We find that SFG population is not large enough to get meaningful constraints on the SFG part of the function. This is expected, because at the SUMSS depths and frequency 843 MHz we are probing well the more luminous AGN population but not the fainter SFG population. In addition, in clusters we would expect the SFG population to be suppressed, making it even harder to constrain. Thus, we fit just for the AGN part of the LF by varying  $x_1$  and  $y_1$  parameters in the MCMC chain

Table 2.3: The best fit LF parameters for different samples of cluster radio galaxies. The samples of SPT fluxes at SUMSS locations “SUMSS in SPT”) are corrected for the SZE flux bias at 95 and 150 GHz, except for “SUMSS in SPT (U)”, which denotes the sample with uncorrected fluxes.

Dataset	$\nu$ (GHz)	$y_1$	$x_1$
SUMSS	0.843	$25.90^{+0.19}_{-0.18}$	$26.81^{+0.20}_{-0.18}$
$z < 0.1$	0.843	$26.10^{+0.40}_{-0.31}$	$27.02^{+0.38}_{-0.30}$
$z > 0.1$	0.843	$25.88^{+0.28}_{-0.27}$	$26.86^{+0.30}_{-0.29}$
SUMSS in SPT	95	$23.89^{+0.46}_{-0.37}$	$25.57^{+0.51}_{-0.44}$
SUMSS in SPT (U)	150	$22.47^{+0.70}_{-1.62}$	$24.62^{+2.53}_{-0.89}$
SUMSS in SPT	150	$23.46^{+0.62}_{-0.46}$	$25.34^{+0.74}_{-0.57}$
SUMSS in SPT	220	$22.58^{+0.33}_{-1.06}$	$24.27^{+1.06}_{-0.77}$

(while keeping other shape parameters for the AGN part of the LF fixed to Condon et al., 2002). We adopt this fitting approach of ignoring the SFG contribution also for the high frequency LFs.

We also validate our fitting code using a much larger sample of radio-loud AGN to construct the field LF (Best & Heckman, 2012). Fitting their dataset (see table 2 of their paper) using the LF described in equation (3.5), we find  $(y_1, b_1, x_1, w_1) = (33.79^{+0.51}_{-0.37}, 1.88^{+0.5}_{-0.4}, 25.48^{+0.08}_{-0.07}, 0.74^{+0.04}_{-0.04})$ , in good agreement with Condon et al. (2002). We see only small differences in our results if we keep  $b_1$  and  $w_1$  fixed to either Condon et al. (2002) or Best & Heckman (2012) values. Thus, we see no sensitivity of our fitting parameters to the decision of whether to adopt Condon et al. (2002) or Best & Heckman (2012) shape parameters.

## LF Measurements

The 150 GHz LFs are shown in Fig. 2.4 for the SUMSS based sample of radio galaxies with uncorrected fluxes, and the sample with SZE flux corrections. In this figure as in all other LF figures, we show the background subtracted observed counts binned within much larger luminosity bins to improve the signal to noise. These figures do not properly represent the LF fitting method described above, but are convenient for showing comparisons of data and best fit models.

The LF has higher amplitude at high luminosities after the SZE flux correction. This increase is due to the additional sources that come into the sample once the bias corrections are applied. While these are low flux sources, the SZE corrections are larger at higher redshifts, so they have a larger impact on the high luminosity radio galaxy population. In Table 2.3 the datasets are listed in the first column followed by the frequency of the

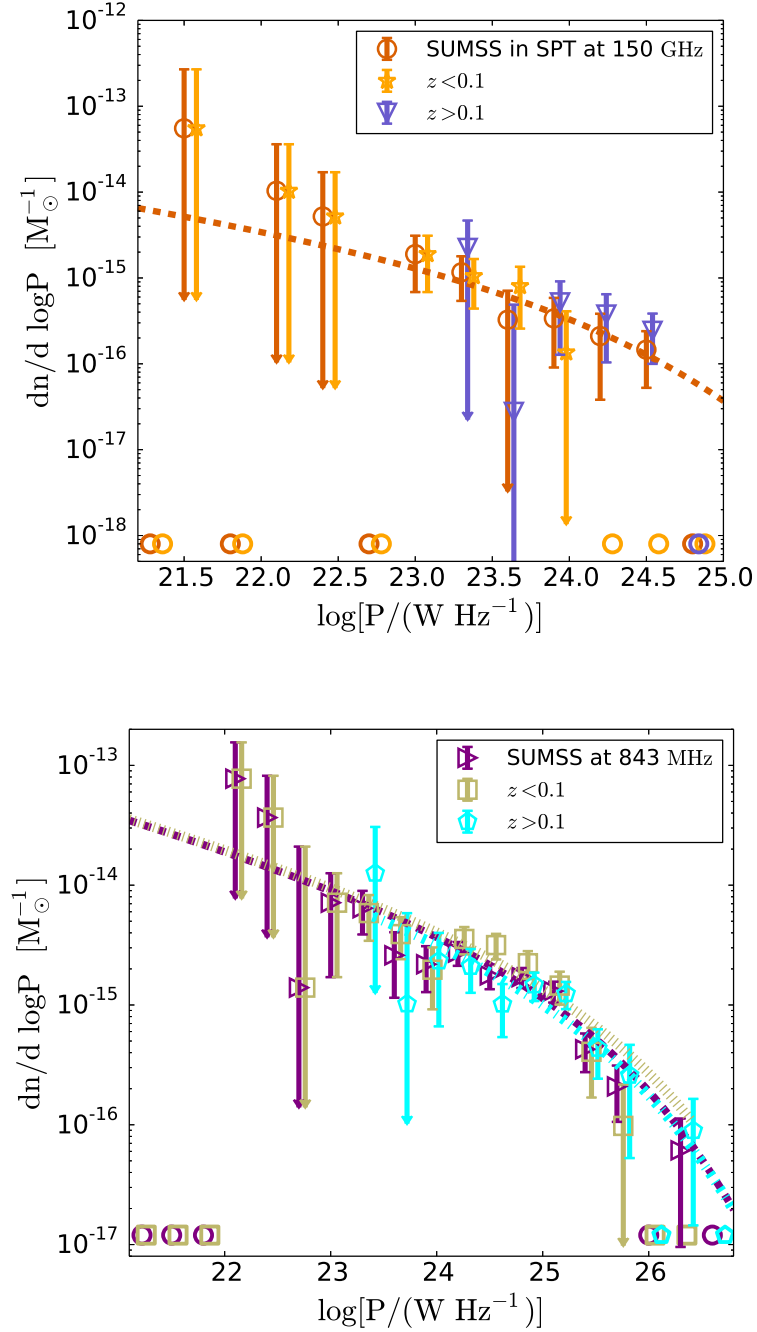


Figure 2.5: Cluster Radio Galaxy LFs: The SUMSS based 150 GHz LF (top), which includes SZE flux bias corrections, and the SUMSS 843 MHz LF (bottom), which is constructed using MCXC clusters over the full 8100 deg<sup>2</sup> SUMSS survey region. The datasets are fitted with the AGN component of the LF by varying  $y_1$  and  $x_1$  parameters as discussed in section 3.4.2. The data points are shifted horizontally to improve visibility. Different lines indicate the best fit model LFs (see Table 2.3). In both plots, we divide the samples into two different redshift bins. However, the data are not enough to provide meaningful constraints on the redshift evolution for the 150 GHz LF. For convenience in this figure the bins containing negative values in the background subtracted counts are represented as points at the bottom of the figure.

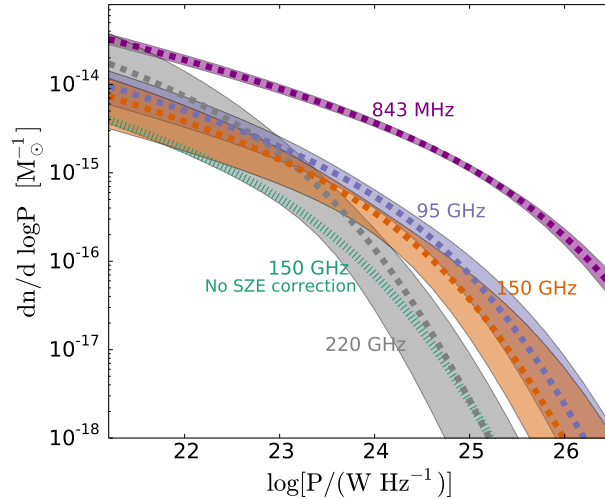


Figure 2.6: LF fits to samples at different observing frequencies. As explained in section 3.4.2 the fit is done using an AGN fitting function (Condon et al., 2002). The filled regions show the best fit model and the  $1\sigma$  confidence regions (see Table 2.3). The curves show the decrease in the cluster radio galaxy population with increasing frequency and increasing power, and – in the 150 GHz case – the impact of the SZE flux bias correction.

sample and then the two LF parameters  $y_1$  and  $x_1$ . The best-fit parameters for the 150 GHz luminosity function before and after SZE correction are different, but given the uncertainties, the differences are not statistically significant.

Next we construct the LF of SUMSS sources at 843 MHz within the  $\theta_{200}$  of MCXC clusters as shown in the right panel of Fig. 2.5. Because the SZE flux is negligible at 843 MHz, no correction is required in the flux measurements of the SUMSS sources. We choose the flux cut at the 100 percent completeness limits of the SUMSS catalog described in section 3.3.2.

We probe for changes with redshift by measuring the LFs in two different redshift bins. To do this, we separate our MCXC cluster population into two redshift bins having similar numbers of galaxy clusters. Given the low redshift nature of the MCXC sample we split at redshift  $z = 0.1$ . In the SUMSS region, we divide the cluster sample into two parts with 159 (174) clusters over  $8100 \text{ deg}^2$  at  $z \leq 0.1$  ( $z \geq 0.1$ ), and construct the LF for these samples (see the right panel of Fig. 2.5). We see no evidence of redshift evolution of the LF, and indeed the measurements that we list in Table 2.3 reflect this lack of evolution.

For the SUMSS based sources with fluxes measured in the SPT maps, the low luminosity end of the LF at 150 GHz mainly consists of galaxy clusters stacked at  $z \leq 0.1$ , as shown in the left panel of Fig. 2.5. At this frequency, there are only 10 SUMSS detected sources within the  $\theta_{200}$  of the galaxy clusters above  $z \geq 0.1$ , and 6 of them are there because of the SZE flux correction. Thus, there are not enough data to constrain the redshift evolution, but certainly in Fig. 2.5 the two subsamples do not appear to be different. We do not present the best fit parameters of the two fits in Table 2.3.

Finally in Fig. 2.6 we plot the best fit LFs at 0.843, 95, 150 and 220 GHz observing frequencies. For comparison we include the 150 GHz LF before SZE flux bias corrections are applied, whereas for 95 GHz only the SZE flux bias corrected LF is shown. As discussed earlier, we fit these LFs using only an AGN component (equation 3.5) with varying  $x1$  and  $y1$  with the other parameters fixed. These LFs are constructed using data that are 100 percent complete at 843 MHz and with a flux cut of 6 mJy at 95, 150 and 220 GHz frequencies to enable a comparison of the radio galaxy populations to the same flux limit. We investigated the impact of faint steep spectrum sources by using much smaller flux cut to construct LFs and confirmed the statistical consistency between the two cases. The number of candidate sources in clusters at 95, 150 and 220 GHz is 65 (34.7), 43 (22.1) and 64 (16.8) before (after) background subtraction, respectively. These numbers are small, and therefore it is not possible to make precise comparisons between the LFs. Nevertheless, it is evident from this plot that the amplitude of the 843 MHz LF is approximately one order of magnitude higher than the amplitude of the high frequency LFs. We show the 150 GHz LF before and after the SZE correction, indicating the significance of accounting for the cluster SZE bias at this frequency. The best fit parameters for the Condon et al. (2002) fitting function are given in Table 2.3 at different frequencies and for the different datasets.

## 2.5 Radio Galaxy Contamination of Cluster SZE

The LFs presented in the last section describe the number of radio galaxies inside a galaxy cluster of a given mass and redshift. The collective flux of these cluster radio galaxies can contaminate the SZE signature of a galaxy cluster, potentially affecting the observability of the cluster and the accuracy of the derived virial mass estimate. To quantify these effects for an SPT-SZ like SZE cluster survey we use the LFs derived from the SUMSS based measurements at 95 and 150 GHz in the SPT maps. These measurements include the SZE flux bias corrections and therefore are our best available estimates of the true underlying 95 and 150 GHz cluster radio galaxy LFs over the mass and redshift ranges of the MCXC sample.

### 2.5.1 Characteristic Levels of Contamination

To estimate the cluster population of radio galaxies, we multiply the LF with the mass of the cluster of interest and integrate it in the luminosity range of  $10^{21}$  to  $10^{27}$   $\text{WHz}^{-1}$ , producing an expectation value  $\langle N_A \rangle$  for the expected number of cluster radio galaxies in this luminosity range.

To model the effects of radio galaxies in a way that accounts for the cluster to cluster variations of the population, we randomly sample a Poisson distribution with mean  $\langle N_A \rangle$  to determine the number  $N_R$  of radio galaxies for a cluster of particular mass and redshift. For each radio galaxy we then assign a flux using the LF at that frequency as the probability distribution function and then sum the fluxes from the  $N_R$  cluster radio galaxies to get the total contaminating cluster radio galaxy flux  $S_A$  in that cluster. We define the degree of

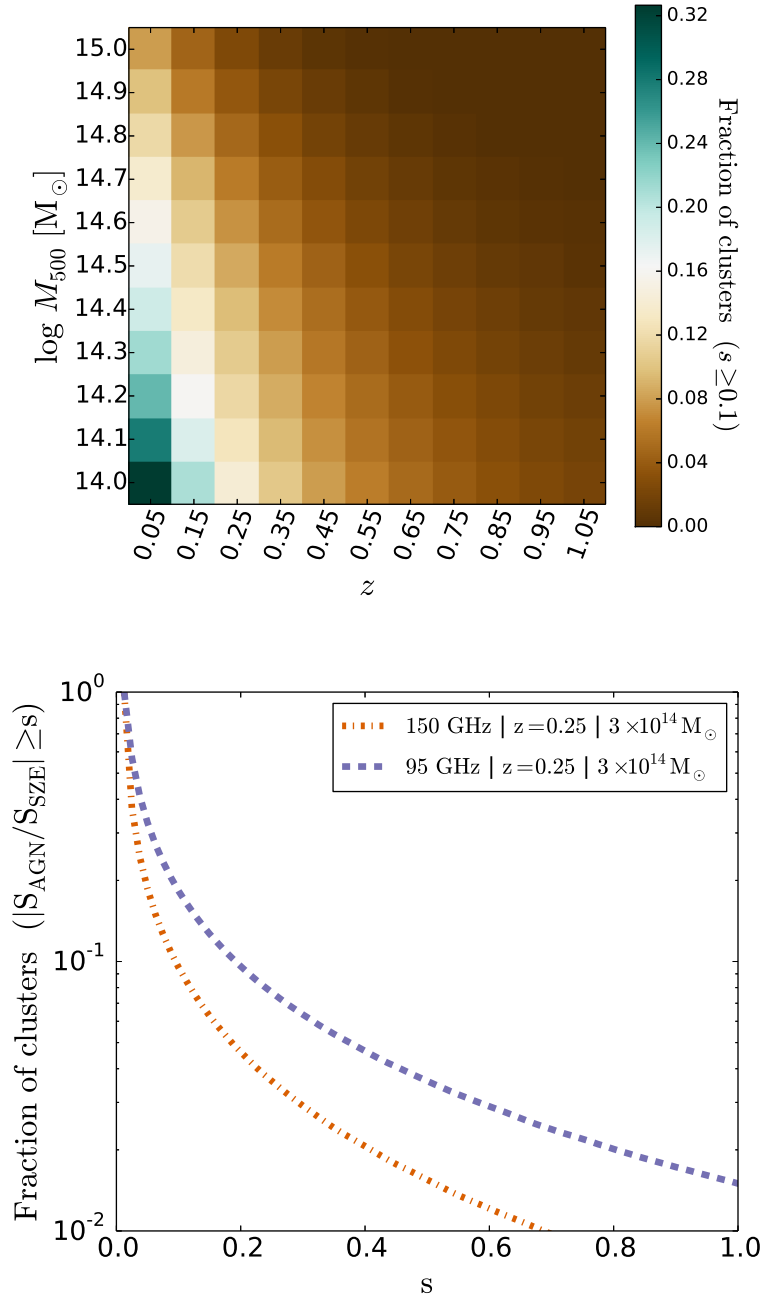


Figure 2.7: Fraction of clusters contaminated above a degree of contamination  $s \geq 0.1$  for clusters as a function of mass  $M_{500}$  and redshift at 150 GHz (top panel). This shows that there is a higher probability of missing the detection of low redshift and low mass clusters. Bottom panel shows the fraction of clusters (with  $M_{500} = 3 \times 10^{14} M_{\odot}$  and  $z = 0.25$ ) above a given degree of contamination  $s$  at 95 and 150 GHz. The contamination is larger at 95 GHz, both because of the smaller SZE signature and the higher AGN fluxes at this frequency as compared to that at 150 GHz.

contamination to be

$$s = \left| \frac{S_A}{S_{\text{SZE}}} \right|, \quad (2.16)$$

where the total cluster radio galaxy flux is  $S_A$  and the total (negative) cluster SZE flux within  $\theta_{200}$  is  $S_{\text{SZE}}$ . The SZE flux of the cluster is derived from the integrated  $Y_{\text{SZ}}$  parameter, using the pressure profiles as described in Arnaud et al. (2010) and is converted into the same units as the cluster radio galaxy flux

$$S_{\text{SZE}} = g_\nu f_\nu I_0 Y_{\text{SZE}}, \quad (2.17)$$

where  $I_0$  is equivalent to  $2(K_B T_{\text{CMB}})^3 / (hc)^2 \simeq 2.7033 \times 10^8$  Jy/sr,  $Y_{\text{SZ}}$  has units of steradian,  $g_\nu$  and  $f_\nu$  give the frequency dependence of the survey such that

$$g_\nu = x \coth\left(\frac{x}{2}\right) - 4, \quad (2.18)$$

$$f_\nu = \frac{x^4 e^x}{(e^x - 1)^2}, \quad (2.19)$$

where  $x = h\nu/k_B T_{\text{CMB}} \simeq \nu / (56.78 \text{ GHz})$  for  $T_{\text{CMB}} = 2.725$  K.

To determine the distribution of contamination  $s$  we iterate this procedure  $10^6$  times for a given cluster mass and redshift and obtain the fraction of clusters above a given value of  $s$ , as plotted in Fig. 2.7. The color plot in the left panel shows the fraction of clusters with  $s \geq 0.1$  for different cluster masses and redshifts. One can see the contamination – at any fixed redshift – is highest for low mass clusters. This is simply because we have modeled our LF as  $M_{500}^{-1}$ , implying that the total flux of expected radio galaxies  $S_A$  will scale linearly with the mass of the cluster. On the other hand, the SZE signature scales as  $S_{\text{SZE}} \propto M_{500}^{5/3}$ . Thus the contamination  $s$  in equation (2.16) scales approximately as  $s \propto M_{500}^{-2/3}$ . Also, note that at a fixed mass  $M_{500}$ , the impact of the radio galaxies is highest at low redshift. This follows because in our preferred model the LF does not evolve with redshift (see discussion of the impact of evolution in section 2.5.4 below), and the SZE flux is approximately constant with redshift (see discussion in Majumdar & Mohr, 2003) while the flux of a source of given luminosity falls as  $d_L^{-2}(z)$  where  $d_L$  is the luminosity distance.

The plot on the right in Fig. 2.7 shows the fraction of clusters contaminated above a given value of  $s$  for the two frequencies relevant for SZE selection at a specific mass and redshift ( $M_{500} = 3 \times 10^{14} M_\odot$  and  $z = 0.25$ , which correspond approximately to the lower mass and redshift limits for the SZ-SPT survey). The contamination is higher at 95 GHz due to the smaller SZE flux at 95 GHz as compared to 150 GHz and the typically higher radio galaxy luminosity at 95 GHz than at 150 GHz.

As the degree of contamination  $s$  reaches unity, the cluster – if unresolved in the SZE maps – exhibits no net SZE signature. We calculate that at redshift  $z = 0.25$  a fraction 0.5 (1.4) percent of clusters with mass  $M_{500} = 3 \times 10^{14} M_\odot$  have no net SZE signature in observations at 150 (95) GHz.

Lin & Mohr (2007) found a much larger contamination by a factor of  $\sim 6$  at mass  $M_{200} = 2 \times 10^{14} M_{\odot}$  and  $z = 0.6$ . This discrepancy is rooted in the fact that, as they emphasized, their results involve an extrapolation of the 1.4 GHz LF to 150 GHz using the distribution of spectral indices measured between 1.4 GHz and 4.85 GHz together with an additional break of 0.5 in  $\alpha$  at 100 GHz. With this approach, the rather small fraction of radio galaxies with positive  $\alpha$  end up populating a high luminosity portion ( $P > 10^{26} \text{ W Hz}^{-1}$ ) of the LF that we do not observe in our high frequency sample.

In a more recent study of 139 cluster radio sources selected at 1.4 GHz and observed at 4.9, 8.5, 22 and 43 GHz with the Very Large Array (VLA) (Lin et al., 2009), the LFs are extrapolated by using spectral indices extracted from  $1.4 \rightarrow 4.9 \rightarrow 8.5 \rightarrow 22 \rightarrow 43 \rightarrow 145$  GHz. The 145 GHz LF is consistent with our 150 GHz LF within the  $1\text{-}\sigma$  model uncertainties. In addition, their estimates for the fraction of missing clusters are similar to our own. Sehgal et al. (2010) analyzed a full-sky, half-arcminute resolution simulations of the microwave sky matched to the observations from ACT to study the correlation of radio galaxies with SZE clusters. Their study suggests that at 148 GHz (90 GHz), for clusters with  $M_{200} > 10^{14} M_{\odot}$ , less than 3 (4) per cent of the clusters have their SZE decrements biased by 20 per cent or more.

### 2.5.2 Incompleteness of SPT-Like Cluster Sample

To estimate the scale of the effect of cluster radio galaxy contamination on the cluster sample detected in the 2500 deg<sup>2</sup> SPT-SZ survey, we first construct the distributions of fractional contamination  $s$  at different cluster masses and redshifts. Then we sample from the halo mass function (Tinker et al., 2008; Eisenstein & Hu, 1998) and use the mass-observable relations to predict the SZE observable with and without the radio galaxy flux biases. The SZE observable is the detection significance  $\xi$ , which is related to the halo mass through a two step process. First,  $\xi$  is biased through the multi-scale matched-filter extraction (Melin et al., 2006), specifically through the selection of the maximum value as a function of position and scale. Thus, it is related to an unbiased SZE significance  $\zeta$  (Vanderlinde et al., 2010), which is the signal-to-noise at the true, underlying cluster position and the filter scale. The relation between  $\xi$  and  $\zeta$  is

$$\zeta = \sqrt{\langle \xi \rangle^2 - 3}. \quad (2.20)$$

Second, the unbiased significance  $\zeta$  is related to mass  $M_{500}$  as

$$\zeta = A_{\text{SZ}} \left( \frac{M_{500}}{3 \times 10^{14} M_{\odot} h^{-1}} \right)^{B_{\text{SZ}}} \left( \frac{E(z)}{E(0.6)} \right)^{C_{\text{SZ}}}, \quad (2.21)$$

where  $A_{\text{SZ}}$  is the normalization,  $B_{\text{SZ}}$  is the mass power law index,  $C_{\text{SZ}}$  is the redshift evolution parameter and  $E(z) \equiv H(z)/H_0$ . For our calculation we adopt the published values for these parameters (Bleem et al., 2015). The fractional intrinsic scatter in the  $\zeta$ -mass relation, which is assumed to be log-normal and constant as a function of mass and redshift is given as  $D_{\text{SZ}} \sim 0.22$ . Rather than modeling the individual subfields within

the SPT-SZ survey, we use a single field with a mean depth scale factor of 1.13 for  $A_{\text{SZ}}$  (see section 2.1 in Bleem et al., 2015, for details about SPT-SZ subfields).

To select clusters from the mass function, we first integrate the halo mass function over a mass range  $10^{14}M_{\odot} \leq M_{500} \leq 10^{16}M_{\odot}$  and redshift in bins of  $\Delta z = 0.1$  in a redshift range of 0.25 to 1.55 to obtain the expected number of clusters  $\langle N_{\text{C}}(z_i) \rangle$  in each redshift bin  $z_i$ . We then Poisson sample the number of clusters  $N_{\text{C}}$  in each bin, and for each of these we assign the mass by sampling the mass function. Given the mass and redshift, we use the  $\zeta$ -mass relation as in equation (3.10) and the log-normal scatter to calculate the  $\zeta$  for each cluster. We then transform from  $\zeta$  to  $\xi$  using equation (3.9) and a normal distribution with standard deviation of unity, which represents the observational noise on the quantity  $\xi$ . In the end we apply a  $\xi$  based selection exactly as it is done within the real SPT-SZ analysis; we examine here the threshold  $\xi \geq 4.5$ .

To study the effect of cluster radio galaxies on the cluster number counts, we adopt the same procedure but introduce a random contaminating flux appropriate for the cluster mass and redshift. Specifically, we derive the contaminated SZE significance  $\zeta_{\text{c}}$  as

$$\zeta_{\text{c}} = \zeta(1 - s_{\text{r}}), \quad (2.22)$$

where  $s_{\text{r}}$  is a randomly selected value of the radio galaxy contamination  $s$  drawn from the calculated distribution of  $s$  for the given cluster mass and redshift. Here the  $s$  distribution not only accounts for the cluster to cluster variation, but also takes into account the uncertainties in the best fit LF parameters. We then calculate  $\xi$  from  $\zeta_{\text{c}}$  as described above. After applying the same selection threshold  $\xi \geq 4.5$ , we find that there is a  $1.8 \pm 0.7$  percent reduction in the number of galaxy clusters over the redshift range  $0.25 \leq z \leq 1.55$  in a  $2500 \text{ deg}^2$  SPT-like SZE survey. The error bars are evaluated by generating 100 realizations of the survey and sampling the  $s$  distributions as previously described. The decrease in the number counts as a function of redshift is shown in Fig. 2.8 for one of the realizations. The ratio of the recovered number of clusters after contamination  $N_{\text{Obs}}$  to the number expected without contamination  $N$  for these  $\xi > 4.5$  samples varies from  $\sim 0.96$  at  $z = 0.3$  to  $\sim 0.99$  at  $z = 1.5$ . Given the size of the current SPT sample (Bleem et al., 2015) the scale of this systematic is small compared to the Poisson sampling noise and therefore not important for recent cosmological studies (e.g. Bocquet et al., 2015; de Haan et al., 2016).

Note that the level of incompleteness presented here is only due to the radio AGN in clusters. In principle, dusty galaxies could also affect the SZE signal. However, we expect the contamination due to dusty galaxies to be minor for clusters in the mass range probed by SPT-SZ, because the galaxy populations are dominated by red sequence galaxies (Hennig et al., 2016), and in general the number of dusty galaxies identified at the 95 and 150 GHz frequencies within SPT-SZ data is smaller by a factor of  $\sim 4$  (Mocanu et al., 2013). In fact, the majority of these dusty sources are lensed background sources (see Vieira et al., 2010; Mocanu et al., 2013, and references there in) because dusty star forming galaxies are very rare within cluster populations.

There are two other comments of note. First, gravitational lensing of sources behind the cluster increases their observed flux, making it more likely that they appear in a flux

limited sample. We do not expect this to have any measurable impact on our measured LFs (see, e.g., Chiu et al., 2016), and therefore we do not apply any correction. Second, the mock SPT-SZ survey described here is modeled with cluster selection at 150 GHz only, which differs from the real SPT-SZ survey where information is incorporated from both 95 and 150 GHz. Thus, we expect the contamination in the real SPT-SZ survey to be slightly higher than (but within the error bars) the results presented here.

### 2.5.3 Impact on $\zeta - M_{500}$ Scaling Relation

#### Scaling Relation Parameters

We examine the bias in the parameters of the  $\zeta$ -mass relation as described in equation (3.10), caused by AGN contamination in clusters. For this purpose, we take all clusters with  $\xi \geq 4.5$  in a redshift range of 0.25 to 1.55. Using an MCMC and assuming the fixed cosmology used throughout this work, we fit the scaling relation for the  $\zeta$  and  $\zeta_c$  distributions of these clusters to get the best fit parameter values and uncertainties. We find that the shift in the best fit parameters obtained from the uncontaminated signal ( $\zeta$ ) and the AGN contaminated signal ( $\zeta_c$ ) is small and is well within the  $1-\sigma$  statistical parameter uncertainties in the two cases. These shifts are of the order of 1%, 2% and 12% for  $A_{SZ}$ ,  $B_{SZ}$  and  $C_{SZ}$ , respectively.

In the cosmological analyses presented by the SPT collaboration, we do not assume a perfect knowledge of the  $\zeta$ -mass scaling relations, but vary these parameters using Gaussian priors. Therefore, a particular bias on the SZE signal caused by radio sources is only important if that bias is large compared to the width of our priors on the scaling relation parameters. The bias we evaluate here is much smaller than the priors we assume in our most recent cosmological analysis (de Haan et al., 2016).

#### Scatter

We also examine the contribution of the cluster radio galaxies to the intrinsic scatter in the  $\zeta$ -mass relation. We calculate the scatter  $\sigma_{\text{ins}}$  in the  $\zeta_c/\zeta$  (note that  $\zeta_c/\zeta \simeq 1 - s_r$ ) distribution for clusters with  $\xi \geq 4.5$  at different redshifts. The combined distribution in a redshift range of 0.25 to 1.55 has  $\sigma_{\text{ins}} \sim 0.028 \pm 0.004$ . As noted previously, the calibrated total intrinsic scatter is 22 percent in the  $\zeta$ -mass relation, and therefore this contribution from cluster radio galaxy contamination plays no significant role in explaining the total observed scatter in the mass-observable relation we employ for the SPT-SZ sample.

### 2.5.4 Redshift Evolution of the Luminosity Function

So far in our analysis for contamination, we have assumed that the LF at 150 GHz does not evolve with redshift. Our analysis (see right panel of Fig. 2.5) supports this assumption at lower observing frequency. The limited sample of galaxy clusters we have in the SPT region with a low median redshift of 0.1 makes it difficult to probe for evolution to higher redshift. This non-evolution, however, is very well supported by a number of previous

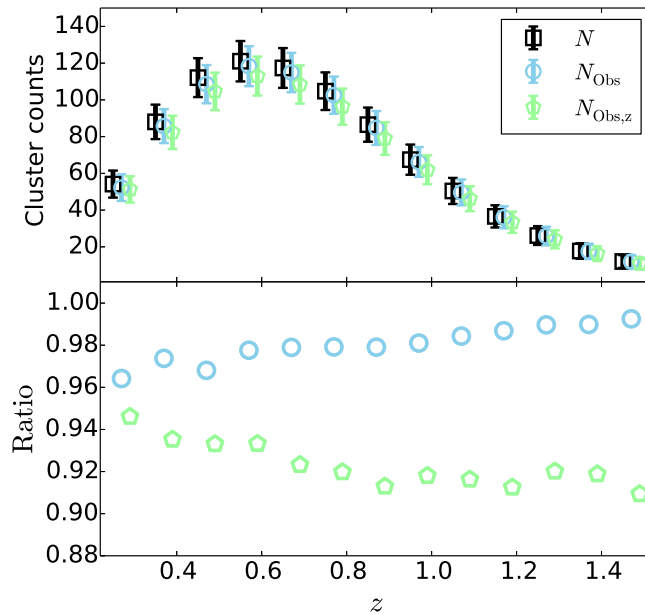


Figure 2.8: The estimated decrease in the observed number of galaxy clusters ( $N_{\text{Obs}}$ ) due to the point source contamination as compared to the theoretical number counts ( $N$ ) for  $2500 \text{ deg}^2$  of the SPT survey with  $\xi_r \geq 4.5$ . The decrease in the observed number of clusters ( $N_{\text{Obs},z}$ ) is also shown for a possible redshift evolution of the form  $(1+z)^{2.5}$  in the number of point sources.

studies. For example, Stocke et al. (1999) compared the 1.4 GHz observations of 19 X-ray selected galaxy clusters in the redshift range of 0.3 to 0.8, with nearby clusters from Ledlow & Owen (1996) and found no evidence of evolution. Similar results were obtained by Branchesi et al. (2006) for a sample of 18 X-ray selected galaxy clusters in the same redshift range. Gralla et al. (2011) constrain the evolution of the bright central radio source population in galaxy clusters from redshift 0.35 to 0.95 by statistically matching FIRST radio sources (Becker et al., 1995) with 618 galaxy clusters from a uniformly, optically selected sample RCS1 (Gladders & Yee, 2005) and find  $0.14 \pm 0.02$  and  $0.10 \pm 0.02$  radio sources per cluster in the range of  $0.35 < z < 0.65$  and  $0.65 < z < 0.95$ , respectively. Fassbender et al. (2011) study a sample of 22 clusters at  $0.9 < z < 1.6$  and show that 30 per cent of them have a central 1.4 GHz radio source. Given the small sample used in this study, the results are consistent with those from the more comprehensive studies already mentioned.

In a recent study, Pracy et al. (2016) derived 1.4 GHz LFs for radio AGN separated into Low Excitation Radio Galaxies (LERGs) and High Excitation Radio Galaxies (HERGs), in the three redshift bins  $0.005 < z < 0.3$ ,  $0.3 < z < 0.5$  and  $0.5 < z < 0.75$ . They found that the LERG population displays little or no evolution  $(1+z)^{0.06^{+0.16}_{-0.18}}$  over this redshift range, while the HERG population evolves more rapidly as  $(1+z)^{2.93^{+0.46}_{-0.47}}$  (assuming pure density evolution in both cases). HERGs have bluer color and lower 4000 Å breaks, which are indications of ongoing star formation activity. LERGs, however, appear to be preferentially

located at the centers of groups or clusters and are fueled by accretion from their hot gas haloes (Kauffmann et al., 2008; Lin et al., 2010; Best & Heckman, 2012). Thus, the LFs presented in our work are presumably dominated by the LERG population and would therefore not be expected to evolve strongly with redshift.

Directly constraining the redshift evolution of the cluster radio galaxy LF at high frequency will require a larger sample of clusters extending to high redshift. In the current analysis we simply bracket the range of possible redshift evolution by examining incompleteness in the case where the radio galaxy number density increases with redshift as  $\phi \propto (1+z)^{2.5}$ . We find that in this case there are  $5.6 \pm 1$  percent of the clusters in the  $2500 \text{ deg}^2$  of the SPT survey at 150 GHz that would be expected to fall out of the  $\xi > 4.5$  selected sample. Our estimated change in the number of galaxy clusters with this kind of extreme evolution model is also shown in Fig. 2.8 in different redshift bins, along with the change we calculate with no redshift evolution.

In this evolutionary scenario we find that the shift in the best fit parameters of the  $\zeta$ –mass relation, obtained by comparing uncontaminated signal ( $\zeta$ ) and contaminated signal ( $\zeta_c$ ) is within the  $1\text{-}\sigma$  parameter constraints for  $B_{\text{SZ}}$  and  $C_{\text{SZ}}$ . The best fit value of  $A_{\text{SZ}}$  is however biased low by 3 percent in the AGN contaminated case. We also calculate that  $4.8 \pm 0.5$  percent of the scatter in the  $\zeta$ –mass relation would come from the cluster to cluster variation in contamination due to cluster radio galaxies. This is still small compared to the empirically constrained scatter of 22 percent.

## 2.6 Systematics

In this section, we discuss the impact of systematic uncertainties in the cluster masses and the radio galaxy fluxes on our results.

### 2.6.1 MCXC Cluster Mass Uncertainties

Because MCXC is a heterogeneous catalog compiled from different ROSAT X-ray Sky Survey-based catalogs (see section 2.3.3), we do not have the information about the mass uncertainties of these clusters. However it is known that the X-ray luminosity–mass relation exhibits a scatter on the order of 40 percent (Vikhlinin et al., 2009; Mantz et al., 2010). Moreover, there is ongoing discussion in the literature about the difference between X-ray hydrostatic masses and other mass estimates, including velocity dispersions, weak gravitational lensing and calibration through the cluster mass function (see Bocquet et al., 2015). Thus we construct our LFs by increasing and decreasing the masses of all clusters by 50 percent to see the maximum impact on our results. The 50 percent decrease in cluster masses affects the LF in three ways: (1) there are fewer sources inside the clusters because the virial radius is smaller, (2) the SZE flux correction for the point sources inside clusters is smaller by  $\approx 50$  percent and (3) the normalization of the LF rises as we scale the observed population as  $M_{500}^{-1}$ . We find that the best fit LFs produced by increasing and decreasing cluster masses are within the  $2\sigma$  model uncertainties of the best fit LF constructed from

the central estimates of the cluster masses. Accordingly, LFs from a 50 percent increase and decrease in the masses are found to lead to incompleteness in an SPT-like sample of  $1.4 \pm 0.8$  percent and  $3.0 \pm 0.7$  percent, respectively, in a redshift range of 0.25 to 1.55. This compares to the  $1.8 \pm 0.7$  percent incompleteness using the published MCXC masses.

### 2.6.2 Radio Galaxy Flux Uncertainties

To fit the luminosity function we compare the observations to the model to determine the likelihood without taking into account the uncertainties in the point source fluxes. To account for the flux uncertainties we compare the observations to the LF model after convolving it with the appropriate flux uncertainties. Because each source has a different flux uncertainty (corresponding to the uncertainty in the luminosity) this is done by taking a Gaussian weighted average over the relevant part of the model (i.e we extracted a convolved value of the model) only for the luminosity bins where there are measured galaxies. For the empty bins we convolve the model with the luminosity uncertainty equivalent to the maximum uncertainty from any source. We see a small difference in the best fit parameters for the LF, which is consistent within the  $1\text{-}\sigma$  parameter uncertainties from the LF of the unconvolved model.

In addition, the radio galaxy source counts are a steep function of flux and the uncertainties in flux could potentially lead to some bias in the LF measurements. Following Mortonson et al. (2011), we estimate this bias at the flux cut to be much smaller than the statistical errors on the LFs; thus this effect has no impact on the contamination estimates.

## 2.7 Conclusions

We use the MCXC catalog of galaxy clusters, the SUMSS catalog of radio galaxies, and the SPT-SZ survey maps to measure the overdensity of radio galaxies associated with clusters. We construct radio galaxy LFs and radial profiles at 843 MHz, 95 GHz, 150 GHz and 220 GHz. The MCXC systems in the SPT-SZ and SUMSS regions have a median redshift  $z \sim 0.1$ , and the highest redshift system is at  $z = 0.686$ . There are 139 MCXC objects in the SPT-SZ region and 333 in the SUMSS region; they span the mass range from groups to clusters with a median mass  $M_{500} = 1.5 \times 10^{14} M_{\odot}$  and  $M_{500} = 1.7 \times 10^{14} M_{\odot}$  in the SPT-SZ and SUMSS regions, respectively.

To construct LFs at high frequencies, we examine SPT maps at the locations of SUMSS sources, extracting the high frequency fluxes and correcting for the cluster SZE flux at 95 and 150 GHz. We compare this sample with the 150 GHz sample with uncorrected fluxes to examine the impact of SZE flux biases, showing that they are significant – especially for high redshift clusters that are more compact on the sky and for higher mass clusters that have stronger SZE signatures. In essence, it is more challenging to find cluster radio galaxies at high frequency in high redshift and high mass clusters, because the SZE signature is biasing their fluxes low.

We use the SUMSS selected sources with fluxes measured at SPT frequencies and

correct for SZE flux bias (at 95 and 150 GHz) to construct the cluster radio galaxy sample for further analysis. We find that the radial profile is centrally concentrated, consistent with an NFW model with concentration  $c = 108_{-48}^{+107}$ . We examine the spectral indices of the radio galaxy population, finding that the spectral index  $\alpha$  measured between 95 and 150 GHz is steeper than that measured between 843 MHz and these high frequencies. We construct the LFs and find best fit parametrizations within the context of Condon et al. (2002) models. In doing so, we assume the overdensity of radio galaxies toward a cluster is at the redshift of the cluster, and we apply a  $k$ -correction using the spectral indices extracted from the sample. Above a luminosity of  $10^{21}$  W Hz $^{-1}$  the 150 GHz LF has roughly half the amplitude of the 95 GHz LF (see Table 2.3 and Fig. 2.6). The amplitude of the 843 MHz LF is approximately one order of magnitude higher than the amplitude of the high frequency LFs. Our high frequency radio galaxy sample is not large enough to constrain redshift or mass trends in the radio galaxy LF.

We use the measured high frequency cluster radio galaxy LFs to examine the effect of the contaminating flux on the SZE signatures of galaxy clusters. To do that, we use the LF for a given cluster mass and redshift to obtain the number and flux of cluster radio galaxies, sampling  $10^6$  times to recover the full range of behavior of the cluster radio galaxies within the clusters. We define a quantity called the contamination  $s$ , which is the absolute value of the ratio of the total cluster radio galaxy flux from all the radio galaxies with power  $> 10^{21}$  W Hz $^{-1}$  to the total SZE flux of that cluster within  $r_{200}$ . With this information we calculate the fraction of clusters with  $s \simeq 1$ , where the total cluster radio galaxy flux in a cluster is equivalent to the negative SZE flux. We find that 0.5 and 1.4 percent of clusters meet this criterion for cluster mass  $M_{500} = 3 \times 10^{14} M_{\odot}$  and redshift  $z = 0.25$  at 150 and 95 GHz, respectively.

To estimate the impact of cluster radio galaxies on the cluster sample from the SPT-SZ 2500 deg $^2$  survey at 150 GHz, we use the theoretically predicted mass function to produce 100 mock cluster samples. We then compare the  $\xi > 4.5$  cluster samples with and without cluster radio galaxies. We find that around  $1.8 \pm 0.7$  percent of clusters would be lost from the sample in a redshift range of 0.25 to 1.55 in the 2500 deg $^2$  SPT-SZ survey.

We evaluate the bias in the parameters of the  $\zeta$ -mass relation caused by radio galaxy contamination and find a small shift in the mean parameter values which is well within the current  $1\text{-}\sigma$  parameter constraints. We also calculate the contribution of the cluster radio galaxy contamination to the intrinsic scatter in the  $\zeta$ -mass relation for the observed clusters, finding that cluster radio galaxies contribute a scatter of  $2.8 \pm 0.4$  percent out of a total empirically calibrated  $\sim 22$  percent scatter.

Finally, we note that with the MCXC sample we cannot place strong constraints on the redshift evolution of the high frequency radio galaxy LF. We review previous findings at 1.4 GHz, none of which provide evidence for strong redshift evolution of the cluster radio galaxy LF. We attempt to bracket the impact of possible redshift evolution by adopting a radio galaxy LF evolution in the number of point sources of the form  $(1+z)^{2.5}$ , showing that at 150 GHz there could be a  $5.6 \pm 1$  percent incompleteness in a  $\xi > 4.5$  SPT-SZ like SZE selected cluster sample.

It has been noted that in the SPT and Planck SZE selected cluster samples there is a

preference for higher cluster masses when these masses are calibrated in conjunction with external cosmological constraints (e.g. Planck Collaboration et al., 2015b) in comparison to direct calibration using weak lensing, velocity dispersions, CMB lensing or X-ray hydrostatic masses (see fig. 2 and fig. 8, respectively, in Bocquet et al., 2015; Planck Collaboration et al., 2015a). Incompleteness in the SZE selected cluster samples is one of several possible effects, including systematic mass biases or even biases in the adopted theoretical mass function (see Bocquet et al., 2016a) that could contribute to this preference. Given the results of our high frequency cluster radio galaxy study, it appears that incompleteness in SZE selected cluster samples due to radio AGN is too small to be playing an important role.

Clearly, a larger sample of non-SZE selected clusters with accurate mass estimates and spanning a larger redshift range is needed to resolve the issues of redshift evolution of the radio galaxy LF and to improve the constraints on the LFs at 150 and 95 GHz. More precise measurements of high frequency radio galaxy LFs will also help us to accurately estimate the incompleteness in the ongoing or upcoming SZE surveys like SPTpol (Bleem et al., 2012), SPT-3G (Benson et al., 2014) and CMB-S4 (Abazajian et al., 2015), which are all expected to be sensitive to lower mass clusters. We are exploring such samples using the Dark Energy Survey (DES Collaboration, 2005) today and are looking forward to the opportunity to examine this population of galaxies in the upcoming eROSITA X-ray survey (Merloni et al., 2012; Predehl et al., 2014).

## Acknowledgements

We acknowledge the support of the International Max Planck Research School on Astrophysics of the Ludwig-Maximilians-Universität, the Max-Planck-Gesellschaft Faculty Fellowship program at the Max Planck Institute for Extraterrestrial Physics, the DFG Cluster of Excellence “Origin and Structure of the Universe”, the Transregio program TR33 “The Dark Universe” and the Ludwig-Maximilians-Universität. The data processing has been carried out on the computing facilities of the Computational Center for Particle and Astrophysics (C2PAP), located at the Leibniz Supercomputer Center (LRZ).

The South Pole Telescope is supported by the National Science Foundation through grant PLR-1248097. Partial support is also provided by the NSF Physics Frontier Center grant PHY-1125897 to the Kavli Institute of Cosmological Physics at the University of Chicago, the Kavli Foundation and the Gordon and Betty Moore Foundation grant GBMF 947. B. A. Benson is supported by the Fermi Research Alliance, LLC under Contract No. De-AC02-07CH11359 with the United States Department of Energy.



# Chapter 3

## Redshift and Mass Trends for High Frequency Cluster Radio Galaxies and Implications for SZE Selected Cluster Samples

N. Gupta<sup>1,2,3</sup>, SPT, DES

<sup>1</sup>Faculty of Physics, Ludwig-Maximilians-Universität, Scheinerstr. 1, 81679 Munich, Germany

<sup>2</sup>Excellence Cluster Universe, Boltzmannstr. 2, 85748 Garching, Germany

<sup>3</sup>Max Planck Institute for Extraterrestrial Physics, Giessenbachstr. 85748 Garching, Germany

### 3.1 Abstract

We study the redshift and mass trends for the radio sources at South Pole Telescope (SPT) and Sydney University Molonglo Sky Survey (SUMSS) frequencies in the direction of optically selected RedMaPPer galaxy clusters from the Dark Energy Survey first year observations (DES-Y1). The radio sources are selected from the SUMSS catalog observed at 843 MHz and SPT-SZ survey maps are used to get the flux densities at 95, 150 and 220 GHz at SUMSS source locations. We show that the radio sources are highly concentrated at the center of clusters by fitting projected Navarro Frank & White (NFW) profiles to their radial distributions. We measure luminosity functions (LFs) and Halo Occupation Numbers (HONs) for these radio sources by statistically correcting for the background population and using the richness–mass–redshift relation calibrated elsewhere. We find that the number of sources depend on the cluster mass as  $N \propto M^{B_H}$  with  $B_H = 0.83 \pm 0.05$ ,  $0.92 \pm 0.25$  and  $1.23 \pm 0.15$  for the 0.843, 95 and 150 GHz datasets, respectively. The pure density

evolution in LFs is estimated as  $(1+z)^{\gamma_D}$ , with power index  $\gamma_D = 2.32^{+0.40}_{-0.41}$ ,  $6.68^{+3.25}_{-3.54}$  and  $6.26^{+2.60}_{-2.77}$  at 0.843, 95 and 150 GHz, respectively. We use LF measurements at 150 GHz to estimate the sample incompleteness and bias in the observable-mass relation for an SPT-SZ like survey. We find that  $(10.7 \pm 2.4)\%$  of clusters would be lost from the cluster sample with detection significance  $\xi \geq 5$  in the redshift range  $0.25 < z < 1.55$  due to radio source contamination, and that the effect is greater at higher redshift. However, we find that the shift in the parameters of observable-mass relation due to this contamination is well within the Gaussian posteriors derived for these parameters in cosmological analyses and thus it is not an important systematic for cosmological parameter estimation using cluster abundance evolution.

## 3.2 Introduction

In the recent years galaxy cluster detection through the Sunyaev-Zel'dovich Effect (SZE; Sunyaev & Zel'dovich, 1972) has enabled us to put competitive constraints on cosmological parameters (Vanderlinde et al., 2010; Sehgal et al., 2011; Benson et al., 2013; Reichardt et al., 2013; Hasselfield et al., 2013; Bocquet et al., 2015; Planck Collaboration et al., 2015a; de Haan et al., 2016). A large sample of clusters is observed by the mm-wave surveys like South Pole Telescope (SPT; Carlstrom et al., 2011), the Atacama Cosmology Telescope (ACT; Fowler et al., 2007) and Planck (Planck Collaboration et al., 2011).

The cluster cosmology is most sensitive to the selection of the clusters as well as the mass-observable relation. Both of these can be affected by the emissions from the cluster radio galaxies that contaminates the SZE signature. Previous studies, which either rely on the extrapolations from the low frequency radio source properties (Lin & Mohr, 2007; Lin et al., 2009; Sehgal et al., 2010; Lin et al., 2015) or having insufficient data at concerned frequencies to constrain the trends in cluster radio sources with redshift (Gupta et al., 2017a), indicate rather small levels of contamination to the SZE signal from clusters.

A number of recent studies have shown that the radio galaxies strongly evolve with redshift in clusters (Sommer et al., 2011; Birzan et al., 2017; Lin et al., 2017) as well as in field (Machalski & Godlowski, 2000; Brown et al., 2001; Strazzullo et al., 2010; McAlpine et al., 2013). However, these studies are all conducted at lower frequencies where the SZE flux is insignificant.

In this paper, we present the redshift and mass trends in the properties of cluster radio galaxies in the 0.843, 95, 150 and 220 GHz frequency bands. We use the Sydney University Molonglo Sky Survey (SUMSS; Bock et al., 1999; Mauch et al., 2003; Murphy et al., 2007) selected radio source catalog observed at 843 MHz along with appropriately filtered SPT-SZ maps at 95, 150 and 220 GHz to measure the Halo Occupation Number (HON) of cluster radio galaxies and the luminosity functions (LFs) of optically selected galaxy clusters from the Dark Energy Survey year one observations (DES-Y1; Rykoff et al., 2016; Rykoff et al. in, prep). We present first constraints on the redshift trends of cluster radio galaxy LFs at 95 and 150 GHz frequencies. We use best fit LF parameters and uncertainties at 150 GHz to estimate the incompleteness as well as the bias in the SZE observable-mass relation in

an SPT-SZ like survey.

The plan of the paper is as follows: In Section 3.3, we discuss the observations and the data used in this work and describe the corrections applied to the point source catalogs at 95 and 150 GHz. Section 3.4 is dedicated to the studies of surface density profiles, Halo Occupation Numbers and LFs. In Section 3.5 we estimate the impact of contamination by high frequency radio galaxies in SZE cluster surveys. We conclude our results in Section 4.7. Throughout this paper we assume a flat  $\Lambda$ CDM cosmology with matter density parameter  $\Omega_M = 0.3$  and Hubble constant  $H_0 = 70 \text{ km s}^{-1} \text{ Mpc}^{-1}$ . We take the normalization of the matter power spectrum to be  $\sigma_8 = 0.83$ .

### 3.3 Data and Radio Galaxy Flux Corrections

We study the overdensity of radio point sources in the direction of galaxy clusters in the Dark Energy Survey first year data of science observations. The radio source catalog is described in (Gupta et al., 2017a). Briefly, the sources are selected from the SUMSS catalog observed at 843 MHz and SPT observations at 95, 150 and 220 GHz are used to measure the source fluxes at SUMSS positions. At 95 and 150 GHz frequencies, the source fluxes are corrected for the SZE flux from galaxy clusters.

#### 3.3.1 SPT Observations

The South Pole Telescope (SPT) is a 10-meter telescope located at the Amundsen-Scott South Pole station in Antarctica (Carlstrom et al., 2011). The 2500 deg<sup>2</sup> SPT-SZ survey has coverage in multiple frequency bands centered around 95, 150 and 220 GHz, corresponding to wavelengths of 3.2, 2.0 and 1.4 mm, respectively. The SPT angular resolution at these three frequencies is approximately 1.6, 1.1 and 1.0 arcmin, and the survey depths are approximately 40, 18 and 70  $\mu\text{K}$ -arcmin, respectively.

The data reduction procedure for SPT is described in detail elsewhere (Staniszewski et al., 2009; Vieira et al., 2010; Schaffer et al., 2011; Mocanu et al., 2013). To increase the signal-to-noise ratio ( $S/N$ ) of unresolved objects a matched filter (Tegmark & de Oliveira-Costa, 1998) is generated. The purpose of this filtering is to increase the sensitivity of the beam size objects by down-weighting signal from larger and smaller scales where the  $S/N$  is small.

Sources in the filtered SPT-SZ maps were identified using the CLEAN algorithm (Högbom, 1974). The flux of the identified sources is calculated from the filtered maps by converting the value of the brightest pixel across the sources from the units of CMB fluctuation temperature to the flux (see Mocanu et al., 2013; Gupta et al., 2017a).

#### 3.3.2 SUMSS Catalog

The Sydney University Molonglo Sky Survey (SUMSS; Bock et al., 1999; Mauch et al., 2003; Murphy et al., 2007) imaged the southern radio sky at 843 MHz with a characteristic

angular resolution of  $\sim 45''$  using the Molonglo Observatory Synthesis Telescope (MOST, Mills, 1981; Robertson, 1991). The survey was completed in early 2007 and covers  $8100 \text{ deg}^2$  of sky with  $\delta \leq -30^\circ$  and  $|b| \geq 10^\circ$ . The catalog contains 210,412 radio sources to a limiting peak brightness of  $6 \text{ mJy beam}^{-1}$  at  $\delta \leq -50^\circ$  and  $10 \text{ mJy beam}^{-1}$  at  $\delta > -50^\circ$ . At the SUMSS selection frequency, we expect nearly all sources above the flux selection threshold to be synchrotron dominated (de Zotti et al., 2005). The position uncertainties in the catalog are always better than  $10''$ . In fact, for sources with peak brightness  $A_{843} \geq 20 \text{ mJy beam}^{-1}$ , the accuracy is in the range  $1''$  to  $2''$ . The flux measurements are accurate to within 3 percent. The catalog is complete to  $8 \text{ mJy}$  at  $\delta \leq -50^\circ$  and to  $18 \text{ mJy}$  at  $\delta > -50^\circ$ . There are approximately 56,000 SUMSS sources in the SPT region at 100 percent completeness (Gupta et al., 2017a). As shown by Mocanu et al. (2013) in an analysis of  $720 \text{ deg}^2$  of the SPT region, all SUMSS sources above  $z \sim 0.05$  are expected to appear pointlike at the SPT angular resolution. At the SUMSS frequency, approximately 10 percent of the sources exhibit extent along one axis (Mauch et al., 2003).

### 3.3.3 DES-Y1 redMaPPer Catalog

For this analysis we use the optically selected galaxy clusters located with red-sequence Matched-filter Probabilistic Percolation algorithm (redMaPPer; Rykoff et al., 2014) from the Dark Energy Survey data from the SPT region of the first year of science observations performed between 31 August 2013 and 9 February 2014. As the name suggests, redMaPPer detects clusters as over-densities of red-sequence galaxies. Precisely, the algorithm estimates the probability of a red galaxy to be the cluster member using a match filter and then measures the richness by summing up the membership probabilities of galaxies in the cluster region. RM has been shown to provide excellent photometric redshifts, richness estimates ( $\lambda$ ), completeness and purity (Rozo & Rykoff, 2014a; Rozo et al., 2014a,b) when applied to Sloan Digital Sky Survey (SDSS) Stripe 82 data (Annis et al., 2014), to the eighth SDSS data release (DR8 Aihara et al., 2011) and to the DES-Y1 and science verification (DES-SV) data (Rykoff et al., 2016; Soergel et al., 2016).

The DES-Y1 redMaPPer catalog (Rykoff et al. in prep) is computed with a brighter luminosity threshold of  $0.4 L^*$  rather than the minimum scatter luminosity threshold of  $0.2 L^*$  (Rykoff et al., 2012) to get a clean volume limited sample of clusters. The center of the cluster is taken to be the position of brightest cluster galaxy (BCG). There are 7,063 galaxy clusters with  $\lambda \geq 20$  in the redshift range of  $0.1 \leq z \leq 0.78$  and a median redshift of 0.46. We compute the masses for these clusters using the best fit  $\lambda$ -mass scaling relation from Capasso et al. in (prep), where mass is defined as

$$M_{200c} = A_\lambda \left( \frac{\lambda}{\lambda_P} \right)^{B_\lambda} \left( \frac{1+z}{1+z_P} \right)^{C_\lambda}, \quad (3.1)$$

with  $A_\lambda = (2.70 \pm 0.03) \times 10^{14}$ ,  $B_\lambda = 1.02 \pm 0.02$  and  $C_\lambda = 0.78 \pm 0.13$ . The pivot richness ( $\lambda_P$ ) and redshift ( $z_P$ ) are given as 41 and 0.18, respectively.

We correct for the Eddington bias in the cluster masses using the formulation in Mortonson et al. (2011).  $M_{200c}$  is in the range of  $1.07 \times 10^{14}$  to  $1.6 \times 10^{15} M_\odot$  with a median

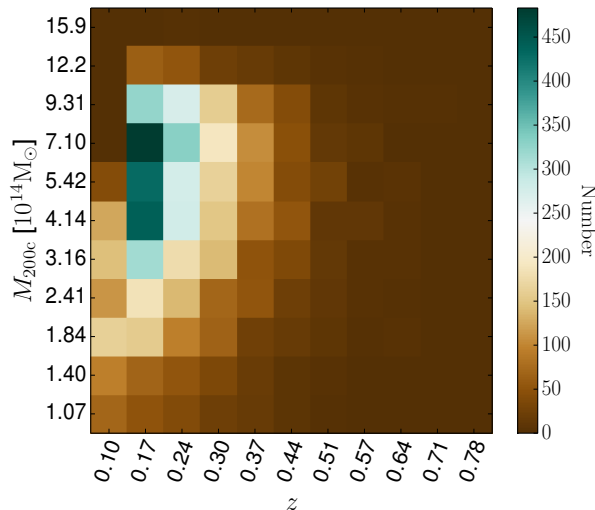


Figure 3.1: Distribution of redMaPPer DES-Y1 galaxy clusters as a function of mass and redshift. The color bar represents the number of clusters. The median mass and redshift of the sample is  $1.8 \times 10^{14} M_{\odot}$  and 0.46, respectively.

value of  $1.8 \times 10^{14} M_{\odot}$ , where  $M_{200c}$  is defined as the mass of the cluster within a sphere where the density is 200 times the critical density of the Universe. Fig. 3.1 shows the mass and redshift distribution of clusters, where the color bar shows the number of clusters in each mass and redshift bin.

### 3.3.4 Radio Galaxy Catalog at SPT Frequencies

As described in detail in Gupta et al. (2017a), the intrinsic flux of a point source residing along the line of sight to a galaxy cluster is biased by the cluster SZE flux which partially or completely obscure the fluxes of sources if detected at 95 and 150 GHz. Thus, we employ the 100 percent complete SUMSS catalog in building the catalogs of high frequency radio galaxies.

This is done by first matching the SUMSS and SPT detected catalogs for the subset of radio galaxies that are bright enough to have made it into the SPT catalog and then by extracting a flux measurement directly from the appropriately filtered CLEANed SPT maps for the rest of the sources (see sections 2.4.1 and 2.4.3 in Gupta et al., 2017a). The CLEANed SPT maps are those where all source above  $S/N > 4.5$  are removed and are thus less affected by the artifacts associated with bright point sources. We describe here the SZE flux bias correction and then the characteristics of the final analysis-ready SUMSS selected catalog at SPT frequencies.

### SZE Flux Bias Correction

To recover the true flux of radio sources at 95 and 150 GHz, we first create SZE maps of the overlapping redMaPPer clusters using a circularly symmetric Compton  $Y$  profile (Arnaud et al., 2010) extending to a radius  $5R_{500c}$ . These maps have same pixel size as the SPT maps and are created by scaling the  $Y$  signal in a pixel by pixel area. We then filter these cluster maps using the matched filter technique for unresolved sources as mentioned in section 3.3.1 to get the peak temperature and flux of an unresolved source as a function of position within the cluster. The SZE flux extracted from the filtered mock maps is then used to boost the observed point source flux.

This flux correction depends upon the position of the point source in the cluster as well as the mass and the redshift of the cluster (Gupta et al., 2017a). As an example, for a cluster with  $M_{200c}$  of  $1.26 \times 10^{15} M_{\odot}$  and redshift of 0.6, a point source in the central pixel (0.04 arcmin from the BCG center) has SZE flux bias of  $\sim 16$  mJy. If not corrected for SZE flux bias this source would be completely obscured in the radio sky at 150 GHz. There are 312 and 266 sources in the line of sight of 7,063 DES-Y1 redMaPPer clusters which are completely obscured without the SZE flux bias corrections at 95 and 150 GHz, respectively. The total number of sources with fluxes greater than zero in the direction of these clusters after the correction are 1174 and 1186 at these frequencies.

### Flux Limited Sample

For our analysis of high frequency radio sources, we select 100 percent complete SUMSS catalog and get the fluxes at 95, 150 and 220 GHz from CLEANed SPT maps. At these frequencies the fainter sources are dominated by the noise, thus we chose only high  $S/N$  sources and correct for the Eddington bias in their flux estimation. To obtain a pure sample we first fit a polynomial function to the observed  $\log N - \log S$  distribution of sources. The best fit polynomial is then numerically convolved with a Gaussian using the noise in the map ( $\sigma_N$ ) and forward modeling is applied to it to get the true underlying distribution of sources. The ratio of true and observed distribution of sources is used to correct for the Eddington bias which is done by scaling the number of radio sources as a function of their flux. We chose 7.5, 4 and 13 mJy flux cuts where the Eddington bias is  $\sim 25$  percent at 95, 150 and 220 GHz frequencies, respectively. The bias decreases rapidly with flux and is at one percent level for a 10 mJy source at 150 GHz.

At SPT frequencies,  $\sim 7$  percent of new sources with  $S/N \geq 5$  are expected to be observed with no counterparts at 843 MHz. This is due to the possible variability of radio sources or wide posteriors of spectral indexes or some error in the SUMSS source selection tree (Mocanu et al., 2013). As our catalogs are selected at SUMSS frequencies, thus, we correct for this small bias in our analysis of high frequency sources as well.

Table 3.1: Best fit projected NFW model parameters for the radial profile of radio galaxies above a flux cut (see section 3.3.4) in a stack of 7063 redMaPPer DES-Y1 galaxy clusters. The samples at 0.843, 95 and 220 GHz are shown, and for each we present concentration  $c$ , the estimate of the total sample of radio galaxies within  $R_{200}$  in our sample  $\sum_{\text{cl}} N_{200}$  and the background density of radio galaxies  $\Sigma_{\text{B}}$  within  $\theta_{200c}$ .

$\nu$ (GHz)	$c$	$\sum_{\text{cl}}(N_{200})$	$\Sigma_{\text{B}}$ [deg $^{-2}$ ]
0.843	$170^{+20}_{-18}$	$1087.8^{+39.7}_{-39.3}$	$54.3 \pm 0.41$
95	$602^{+1150}_{-540}$	$53.4^{+9.2}_{-8.2}$	$2.82 \pm 0.03$
150	$458^{+358}_{-272}$	$75.7^{+10.7}_{-9.7}$	$3.55 \pm 0.04$

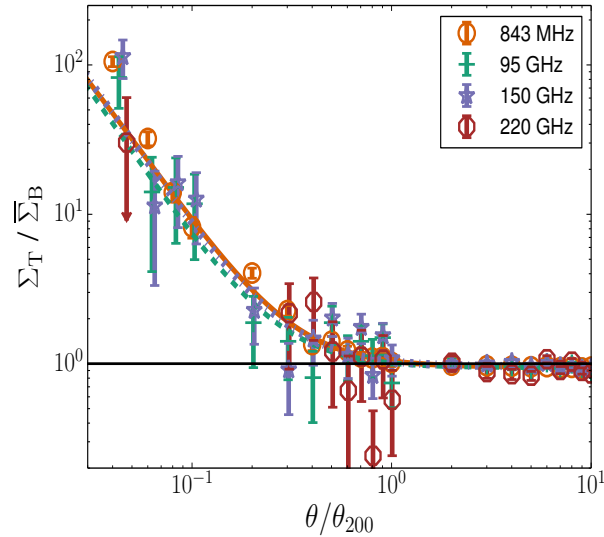


Figure 3.2: Radial distribution of radio sources observed at 0.843, 95, 150 and 220 GHz in the direction of redMaPPer DES-Y1 galaxy clusters. The lines are the best fit projected NFW models (see Table 3.1). At 220 GHz, the data is not enough to constrain the projected NFW profile.

## 3.4 Cluster Radio Galaxy Populations

### 3.4.1 Radial Distribution of Cluster Radio Galaxies

We study the radial distribution of radio galaxies in the cluster  $\theta_{200c}$  by stacking all radio galaxies overlapping the redMaPPer sample. Following Gupta et al. (2017a), we use the projected NFW profile  $\Sigma(x)$  (Navarro et al., 1997; Bartelmann, 1996) as a fitting function for the radial distribution. Here  $x = r/r_s$  and  $r_s = R_{200c}/c$ , where  $c$  is the concentration parameter and  $x$  is equivalent to  $c$  for  $r = R_{200c}$ .

The total surface density of the clusters ( $\Sigma_T$ ) can have both cluster and background components ( $\Sigma_B$ ) and is written as

$$\Sigma_T = \Sigma(x) + \Sigma_B, \quad (3.2)$$

and to reduce the covariance between the normalization and concentration, we write this in terms of the number of galaxies as

$$N_T = N(x) + \Sigma_B A, \quad (3.3)$$

where  $A$  is the solid angle of the annulus or bin and number of background subtracted galaxies  $N(x) = N_{200}$  for  $r = R_{200c}$ . We fit our stacked distribution of radio galaxies to a model with three parameters:  $c$ ,  $N_{200}$  and  $\Sigma_B$  (see Gupta et al., 2017a). We stack radio galaxies out to  $10 \times \theta_{200c}$  to allow for a good constraint on the background density  $\Sigma_B$ .

We employ the Cash (1979) statistic

$$C = \sum_i (N_{T,i}^d \ln(N_{T,i}^m) - N_{T,i}^m - N_{T,i}^d \ln(N_{T,i}^d) + N_{T,i}^d), \quad (3.4)$$

in this fit, where  $N_{T,i}^m$  is the total number of galaxies from the model as in equation (3.3) and  $N_{T,i}^d$  is the total number of galaxies in the observed data in the  $i^{\text{th}}$  angular bin.

We use the Markov Chain Monte Carlo (MCMC) code, `emcee` (a Python implementation of an affine invariant ensemble sampler; Foreman-Mackey et al., 2013) to fit the model to the data throughout this work. In the fitting we adopt a bin size corresponding to  $\theta_{200c}/1000$  and fit over the region extending to  $10\theta_{200c}$ . The concentration parameter is sampled in log space during the fit.

The best fit values and uncertainties of the parameters are given in Table 3.1 for the radio galaxy data at 0.843, 95 and 150 GHz in the stack of redMaPPer clusters. The number of background subtracted galaxies  $N_{200}$  is smaller at higher frequency due to the choice of high  $S/N$  sources from SPT maps.  $\Sigma_B$  is the background density per unit [ $\text{deg}^{-2}$ ]. The profile is centrally concentrated with  $c \sim 170, 600$  and  $450$  at 0.843, 95 and 150 GHz, respectively. We use this behavior in the next section to correct the projected LF to the LF within the cluster virial region defined by  $R_{200c}$ .

In Fig. 3.2 we show the best fit surface density profiles and data for each of the datasets. To create these plots we combined many bins to reduce the noise in the measured radial profile. Following Gupta et al. (2017a), we normalize the  $y$ -axes of this plot with the

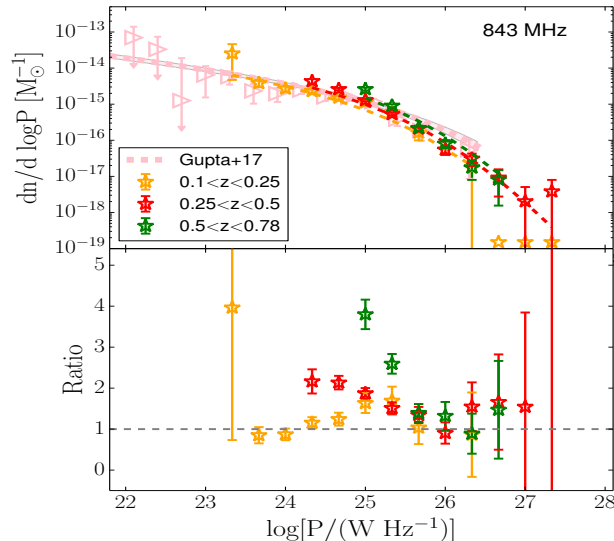


Figure 3.3: Cluster Radio Galaxy LFs: Upper panel shows the SUMSS based 843 MHz LF, which is constructed using DES-Y1 redMaPPer galaxy clusters. The uncertainties are represented by Poisson errors here. The datasets are fitted with the LF model by varying  $y$ ,  $x$  and  $\gamma$  (density or luminosity evolution) parameters as discussed in section 3.4.2. Different lines indicate the best fit model LFs (see Table 3.2). Lower panel shows the ratio between the data points and the best fit model for first redshift bin, representing the change in the shape of LFs. We divide the samples into three different redshift bins. For convenience in this figure the bins containing negative values in the background subtracted counts are represented as points at the bottom of the figure. We show the data, best fit model and model uncertainties from Gupta et al. (2017a) in pink here.

annulus area in each angular bin and the background level density or the mean number density of sources ( $\bar{\Sigma}_B$ ). Fig. 3.2 shows that  $\bar{\Sigma}_B$  is a good estimation of the background number density of the clusters, as  $\Sigma_T/\bar{\Sigma}_B$  is consistent with 1 outside of the cluster. At 220 GHz the data is not enough to constrain the projected NFW profile.

### 3.4.2 Redshift trends for Radio Galaxy Luminosity Functions

We construct radio LFs by counting the excess of radio sources in the direction of redMaPPer galaxy clusters. We use the redshift of clusters to estimate the radio source luminosities and we apply the redshift dependent  $k$ -correction with a spectral index of -0.7 to get the luminosity at the same rest frame frequency for all redshifts.

#### LF Construction Method and Modeling

The method to construct LFs is described in detail in previous works (Lin et al., 2004; Gupta et al., 2017a). Briefly, we add up the number of point sources within  $\theta_{200c}$  of all

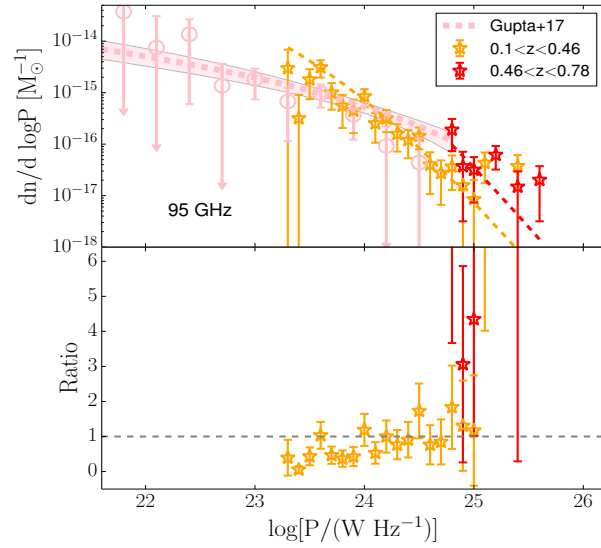


Figure 3.4: Same as Fig. 3.3 but for 95 GHz observed SUMSS selected radio sources.

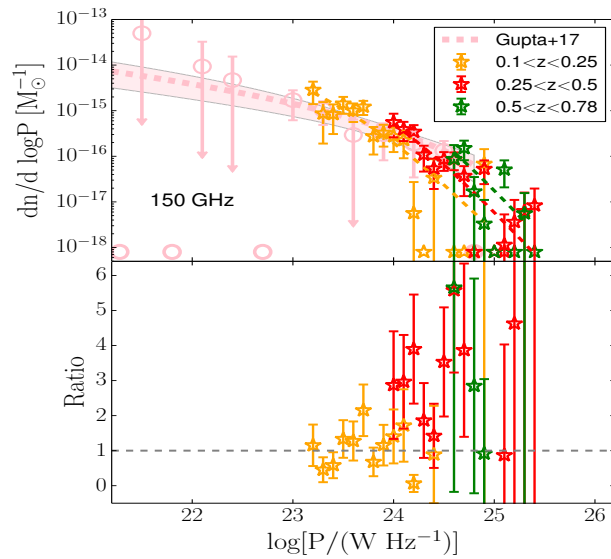


Figure 3.5: Same as Fig. 3.3 but for 150 GHz observed SUMSS selected radio sources.

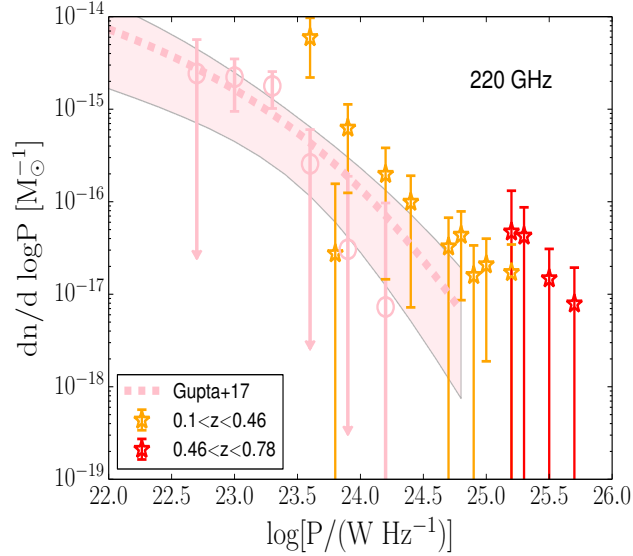


Figure 3.6: Same as Fig. 3.3 but for 220 GHz observed SUMSS selected radio sources. The data is not enough to provide meaningful constraints on the redshift evolution for the 220 GHz LF, thus we do not plot the ratio between the data points and best fit model as well.

Table 3.2: The best fit LF parameters for different samples of cluster radio galaxies. The samples with SPT fluxes at SUMSS locations are corrected for the SZE flux bias at 95 and 150 GHz.  $\gamma_D$  and  $\gamma_P$  are defined as the density and luminosity redshift evolution parameters, respectively.

$\nu$ (GHz)	$y$	$x$	$\gamma_D$
0.843	$25.61^{+0.05}_{-0.05}$	$26.32^{+0.08}_{-0.08}$	$2.32^{+0.40}_{-0.41}$
95	$23.73^{+0.38}_{-0.32}$	$23.74^{+0.41}_{-0.46}$	$6.68^{+3.25}_{-3.54}$
150	$23.37^{+0.24}_{-0.20}$	$23.82^{+0.34}_{-0.35}$	$6.26^{+2.60}_{-2.77}$
$\nu$ (GHz)	$y$	$x$	$\gamma_P$
0.843	$25.67^{+0.05}_{-0.05}$	$26.45^{+0.08}_{-0.08}$	$2.21^{+0.46}_{-0.45}$
95	$23.53^{+0.24}_{-0.22}$	$24.08^{+0.32}_{-0.38}$	$3.03^{+1.30}_{-1.71}$
150	$23.21^{+0.13}_{-0.13}$	$24.16^{+0.25}_{-0.27}$	$2.90^{+1.14}_{-1.31}$

clusters in logarithmic luminosity bins. We estimate the background source counts in these luminosity bins from the corresponding bins in  $\log N - \log S$  space by again using the cluster redshift to transform from radio source flux to luminosity. As we want the background counts in cluster virial region, thus, we correct the counts for the surface area of all the clusters in our sample. For the reasons discussed in Gupta et al. (2017a) and in upcoming section 3.4.3, we normalize our LFs by the total mass of the clusters, which are contributing to each of the luminosity bins.

We fit our LFs using the functional form from Condon et al. (2002) given as

$$\log \left( \frac{dn}{d \log P} \right) = y - \left[ b^2 + \left( \frac{\log P - x}{w} \right)^2 \right]^{1/2} - 1.5 \log P, \quad (3.5)$$

where the parameters  $b$ ,  $x$  and  $w$ , control the shape of the LF and  $y$  is its amplitude.

Assuming that the overall shape of LFs remain constant, the only changes can be in the density and luminosity of the sources (Machalski & Godlowski, 2000). The density evolution corresponds to a vertical shift in the LFs and can be quantified as

$$\frac{dn(z)}{d \log P} = \frac{dn(z=0)}{d \log P} \times \left( \frac{1+z}{1+z_C} \right)^{\gamma_D}, \quad (3.6)$$

similarly, the luminosity evolution corresponds to a horizontal shift in the LFs because of evolving luminosities of the sources

$$P(z) = P(z=0) \times \left( \frac{1+z}{1+z_C} \right)^{\gamma_P}, \quad (3.7)$$

where  $z_C$  corresponds to the median redshift of the redMapper cluster sample ( $\sim 0.46$ ).  $\gamma_D$  and  $\gamma_P$  correspond to the power law index for density and luminosity evolution of LFs, respectively.

We again perform MCMC analysis with the Cash statistic to fit LFs. Following Gupta et al. (2017a), we fit for the AGN part of the LF, fix the values of two shape parameters  $b$  and  $w$  to those determined in Condon et al. (2002) and vary  $x$  and  $y$  along with density or luminosity evolution power law index. In agreement with (Gupta et al., 2017a), we find consistent results when  $b$  and  $w$  are fixed to either Condon et al. (2002) or Best & Heckman (2012) best fit values. We evaluate the likelihood of a given model by scaling the LF model with the total cluster mass contributing to each luminosity bin and then adding the statistically determined background number of galaxies to it for corresponding luminosity bin.

We correct our LF amplitudes by scaling it with a deprojection factor ( $D_{\text{prj}}$ ) that accounts for the cylindrical to spherical projection bias of radio galaxies. This correction is very small as for the radio sources in the direction of galaxy clusters the NFW concentrations are very high (see Table 3.1) and  $D_{\text{prj}} \sim 0.93, 0.95$  and  $0.94$  for 0.843, 95 and 150 GHz LFs, respectively.

We validate our codes by analyzing simulated samples (10 times the size of our 843 MHz radio source catalog) created using the best fit LFs reported in Table 3.2 (for density evolution), demonstrating that we recover the input parameters.

### Measurements and Comparison of LF trends

We construct LFs at 0.843, 95, 150 and 220 GHz as shown in the upper panels of Figs. 3.3, 3.4, 3.5 and Fig.3.6, respectively. In these figures, we show the background subtracted observed counts in larger luminosity bins and in three or two redshift bins. However, these figures do not represent the fitting method, where the observed counts are divided into much finer luminosity bins and in 15 redshift bins (with similar number of clusters in each bin) to get the model parameters. We also show the best fit data and model along with model uncertainties from Gupta et al. (2017a), where the median redshift of the sample is 0.1. In Table 3.2, we show the best fit parameters for the LFs, where the upper panel describes the results when pure density evolution is considered and lower panel tables the results when pure luminosity evolution is taken into account. We find that our data is not enough to allow both density and luminosity evolution scenarios in the MCMC analysis.

At 843 MHz, we chose all sources to construct the LF with a flux limit at the 100 percent completeness of the SUMSS catalog as described in section 3.3.2. As SZE correction is negligible at this frequency so no correction is applied here. However, at 95 and 150 GHz, we use SZE corrected sample to study the redshift trends in the LFs. The density evolution power law index ( $\gamma_D$ ) of the LFs at 95 and 150 GHz is consistent with the evolution at 843 MHz LF within  $\sim 1.2$  and  $1.4 \sigma$  levels, respectively. The luminosity evolution index ( $\gamma_P$ ) is however, consistent at all frequencies well within the  $1\text{-}\sigma$  levels.

In the lower panels of Figs. 3.3, 3.4 and 3.5, we show the ratio between the data points and the best fit LF model for first redshift bin. This represents a change in shape of the LF with increasing redshift. For instance at 843 MHz, there is a large redshift evolution in LF at lower luminosities but for power  $> 10^{25.5} \text{ W/Hz}^{-1}$ , no evolution with redshift is evident. At 95 and 150 GHz, the signal is totally diluted at higher luminosities, thus we do not have a strong evidence there.

Similar trends with redshift were seen in previous studies for field radio LFs. LFs of optically selected Quasi-Stellar Objects (QSOs) at  $z \leq 2.2$  showed a luminosity evolution with  $\gamma_P = 3.2 \pm 0.1$  (Boyle et al., 1988). Machalski & Godlowski (2000) and Brown et al. (2001) studied a sample of 1.4 GHz radio sources at low and intermediate redshifts and suggested a luminosity evolution of  $\gamma_P = 3 \pm 1$  and  $4 \pm 1$ , respectively. In a recent study, Pracy et al. (2016) derived 1.4 GHz LFs for radio AGN separated into Low Excitation Radio Galaxies (LERGs) and High Excitation Radio Galaxies (HERGs). They found that the LERG population displays little or no evolution, while the HERG population evolves more rapidly as  $\gamma_P = 7.41^{+0.79}_{-1.33}$  and  $\gamma_D = 2.93^{+0.46}_{-0.47}$ . HERGs have bluer color and lower 4000 Å breaks, which are indications of ongoing star formation activity. LERGs, however, appear to be preferentially located at the centers of groups or clusters and are fueled by accretion from their hot gas haloes (Kauffmann et al., 2008; Lin et al., 2010; Best & Heckman, 2012). Strazzullo et al. (2010) carried out a multi-wavelength analysis of Deep *Spitzer* Wide-area InfraRed Extragalactic Legacy Survey Very Large Array field (SWIRE VLA) and find  $\gamma_P = 2.7 \pm 0.3$  and  $3.7^{+0.3}_{-0.4}$  for AGN and starforming populations, respectively. Similarly, McAlpine et al. (2013) studied pure density and luminosity evolutions for a combined datasets of  $\sim 900$  VLA observed galaxies in field and find  $\gamma_P = 1.18 \pm 0.21$  and  $2.47 \pm 0.12$

Table 3.3: Best fit normalization  $A_{\text{H}}$  and slope  $B_{\text{H}}$  of the power law at 0.843, 95 and 150 GHz (see section 3.4.3).

$\nu$ (GHz)	$A_{\text{H}}$	$B_{\text{H}}$
0.843	$0.196 \pm 0.006$	$0.83 \pm 0.05$
95	$0.021 \pm 0.002$	$0.92^{+0.22}_{-0.25}$
150	$0.019 \pm 0.002$	$1.23^{+0.14}_{-0.15}$

for AGN and star forming galaxies, respectively. Janssen et al. (2012) demonstrated that in the local universe a sub-population of LERGs are hosted in blue starforming galaxies, with these blue LERGs becoming increasingly important at higher radio powers. Thus, it is possible that the contribution of such blue LERGs increases towards higher redshifts, rendering the initial assumption that all AGN are hosted by red passive galaxies invalid.

Also for clusters, Green et al. (2016) have shown that at least 14 percent of BCGs show a significant color offset from passivity in a population of 980 X-ray detected clusters ( $0.03 < z < 0.5$ ). In table 2 and figure 16, they show the offset to passivity as a function of X-ray luminosity of host clusters and they find larger fraction of galaxies with offset from passivity in high luminous clusters which are preferentially at high redshift. For samples of X-ray and optically selected galaxy clusters, Sommer et al. (2011), show  $\gamma_{\text{P}} = 8.19 \pm 2.66$  and  $3.99 \pm 1.24$ , respectively using 1.4 GHz detected radio galaxies from FIRST survey in a redshift range of 0.1 to 0.3. They also find a steep pure density evolution with  $\gamma_{\text{D}} = 9.40 \pm 1.85$  for X-ray selected sample of galaxy clusters. In a recent work, Birzan et al. (2017) investigated AGN feedback in a large sample of SZE selected clusters from SPT and ACT surveys and found  $\sim 7$  times more SUMSS sources in  $z > 0.6$  clusters than in the  $z < 0.6$  sample, which may due to the differences in the accretion mechanism onto the super massive black holes (SMBHs) in the low and high luminosity sources. In another recent work, Lin et al. (2017) constructed the radio LFs for 1.4 GHz sources in clusters out to  $z \sim 1$  and find an over-abundance of radio galaxies in clusters compared to the field population. They find that cluster galaxies at  $z > 0.77$  are about 1.5 to 2 times more likely to be active in the radio compared to those in the lower- $z$  clusters.

### 3.4.3 Halo Occupation Number

We define the halo occupation number (HON) as the number of background subtracted radio galaxies in a stack of galaxy clusters. We estimate the HON in a stack of redMaPPer clusters in various mass bins to study the mass trends for 0.843, 95, 150 and 220 GHz observed radio sources. We take out the redshift trends estimated at these frequencies in previous section to get the redshift independent mass trends. This is done by multiplying the observed galaxy counts from cluster stack for each luminosity bin by a factor of  $(1+z)^{-\gamma_{\text{D}}}$ . Fig. 3.7 shows the HON at these frequencies, where we also show the best fit power

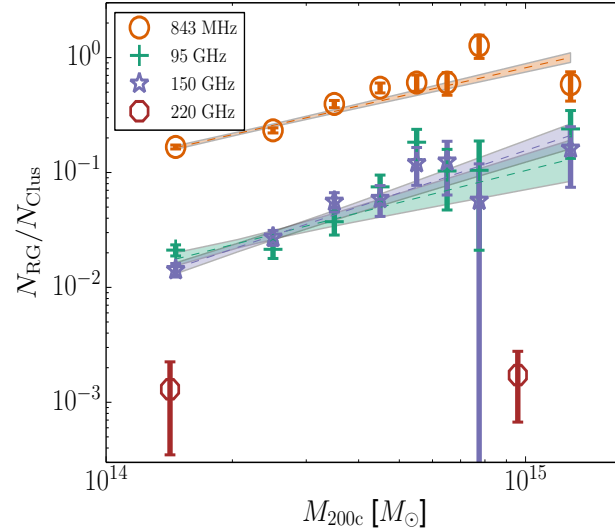


Figure 3.7: HONs: Number of radio sources observed at 0.843, 95, 150 and 220 GHz per unit number of galaxy clusters. The dashed lines are the best fit power law models and shaded regions show  $1\text{-}\sigma$  model uncertainties (see Table 3.3). The redshift dependence is marginalized here by multiplying the number of radio galaxies by  $(1+z)^{-\gamma_D}$ , where  $\gamma_D$  is the density evolution presented in Table 3.3 for different frequencies.

law of the form

$$N_H = A_H \left( \frac{\langle M_{200c} \rangle}{1.8 \times 10^{14}} \right)^{B_H}, \quad (3.8)$$

where  $N_H$  describes the galaxy count per unit number of clusters and  $A_H$  and  $B_H$  are the normalization and slope of the power law, respectively.  $\langle M_{200c} \rangle$  is the mean mass of clusters in each of the mass bins. The best fit slopes and normalizations are presented in Table 3.3 for different frequencies, except for 220 GHz, where data is not enough to fit for the power law. In Fig. 3.7, we also show the  $1\text{-}\sigma$  model uncertainties as the shaded region over the model.

Similar slope was estimated by Lin et al. (2004) in an analysis of the near-infrared (NIR) K-band properties of galaxies within 93 galaxy clusters and groups using data from the Two Micron All Sky Survey (2MASS), where they found  $B_H = 0.84 \pm 0.04$ . This indicates that the high mass galaxy clusters have fewer number of galaxies per unit mass as compared to low mass clusters and strengthens our choice of normalizing the LFs by the mass of the galaxy clusters. The slopes are larger at higher frequencies but consistent among each other within  $2\text{-}\sigma$  level.

### 3.5 Radio Galaxy Contamination of Cluster SZE

The LFs and their redshift trends presented in section 3.4.2 describe the background subtracted number of galaxies in a galaxy cluster of a given mass and redshift. The galaxies in these clusters can collectively contaminate the SZE flux from clusters and result in incompleteness in the SZE selected cluster samples. In this section we use LFs derived from SUMSS selected radio sources at 150 GHz to quantify the incompleteness in SPT-SZ like survey of galaxy clusters.

We estimate the levels of contamination in the same way as described in detail in Gupta et al. (2017a). Briefly, we multiply the LF at 150 GHz with the mass of the cluster of interest and integrate it in the luminosity range of  $10^{23}$  to  $10^{26}$   $\text{WHz}^{-1}$  to get the expectation number of radio galaxies  $\langle N_A \rangle$ . This range of luminosity is selected as these are the minimum and maximum luminosities of the galaxies observed in our sample of clusters. We take into account the cluster to cluster variation in the number of galaxies by sampling  $10^3$  random numbers from a Poisson distribution with mean  $\langle N_A \rangle$  to determine the  $N_R$  for a cluster of a particular mass and redshift. In addition, we propagate the uncertainties in the LF model by randomly sampling  $10^3$  set of parameters from the full MCMC chain after removing the burn-in part of the chain. Thus, we have a distribution of  $10^6$  random samples  $N_R$  and to each of these samples we assign luminosities and fluxes (using the redshift of the cluster as before) using the 150 GHz LF as the cumulative distribution function. We then sum the fluxes from  $N_R$  cluster radio sources to get the total flux  $S_A$  in that cluster. Following Gupta et al. (2017a), we define the degree of contamination ( $s$ ) for each cluster as  $S_A/S_{\text{SZE}}$ , where  $S_{\text{SZE}}$  is the total SZE flux of that cluster. Thus we have a distribution of fractional contamination  $s$  for different cluster masses and redshifts which include the effects of cluster to cluster variation in galaxy counts as well as uncertainties in the LF model.

#### 3.5.1 Incompleteness in SPT-SZ like Survey

To estimate the scale of the effect of cluster radio galaxy contamination on the cluster sample detected in the  $2500 \text{ deg}^2$  SPT-SZ survey, we sample from the halo mass function (Tinker et al., 2008; Eisenstein & Hu, 1998) and use the mass-observable relations to predict the SZE observable with and without the radio galaxy flux biases. The SZE observable is the detection significance  $\xi$ , which is related to the halo mass through a two step process. First,  $\xi$  is biased through the multi-scale matched-filter extraction (Melin et al., 2006), specifically through the selection of the maximum value as a function of position and scale. Thus, it is related to an unbiased SZE significance  $\zeta$  (Vanderlinde et al., 2010), which is the signal-to-noise at the true, underlying cluster position and the filter scale. The relation between  $\xi$  and  $\zeta$  is

$$\zeta = \sqrt{\langle \xi \rangle^2 - 3}. \quad (3.9)$$

Second, the unbiased significance  $\zeta$  is related to mass  $M_{500}$  as

$$\zeta = A_{\text{SZ}} \left( \frac{M_{500}}{3 \times 10^{14} M_{\odot} h^{-1}} \right)^{B_{\text{SZ}}} \left( \frac{E(z)}{E(0.6)} \right)^{C_{\text{SZ}}}, \quad (3.10)$$

where  $A_{\text{SZ}}$  is the normalization,  $B_{\text{SZ}}$  is the mass power law index,  $C_{\text{SZ}}$  is the redshift evolution parameter and  $E(z) \equiv H(z)/H_0$ . For our calculation we adopt the published values for these parameters (Bleem et al., 2015), which are also consistent with those obtained in the latest cosmological analysis (de Haan et al., 2016). The fractional intrinsic scatter in the  $\zeta$ -mass relation, which is assumed to be log-normal and constant as a function of mass and redshift is given as  $D_{\text{SZ}} \sim 0.22$ . Rather than modeling the individual subfields within the SPT-SZ survey, we use a single field with a mean depth scale factor of 1.13 for  $A_{\text{SZ}}$  (see section 2.1 in Bleem et al., 2015, for details about SPT-SZ subfields).

To select clusters from the mass function, we first integrate the halo mass function over a mass range  $10^{14} M_{\odot} \leq M_{500} \leq 10^{16} M_{\odot}$  and redshift in bins of  $\Delta z = 0.1$  in a redshift range of 0.25 to 1.55 to obtain the expected number of clusters  $\langle N_{\text{C}}(z_i) \rangle$  in each redshift bin  $z_i$ . We then Poisson sample the number of clusters  $N_{\text{C}}$  in each bin, and for each of these we assign the mass by sampling the mass function. Given the mass and redshift, we use the  $\zeta$ -mass relation as in equation (3.10) and the log-normal scatter to calculate the  $\zeta$  for each cluster. We then transform from  $\zeta$  to  $\xi$  using equation (3.9) and a normal distribution with standard deviation of unity, which represents the observational noise on the quantity  $\xi$ . In the end we apply a  $\xi$  based selection exactly as it is done within the real SPT-SZ analysis; we examine here the threshold  $\xi \geq 5$ .

To study the effect of cluster radio galaxies on the cluster number counts, we adopt the same procedure but introduce a random contaminating flux appropriate for the cluster mass and redshift. Specifically, we derive the contaminated SZE significance  $\zeta_{\text{c}}$  as

$$\zeta_{\text{c}} = \zeta(1 - s_{\text{r}}), \quad (3.11)$$

where  $s_{\text{r}}$  is a randomly selected value of the radio galaxy contamination  $s$  drawn from the calculated distribution of  $s$  for the given cluster mass and redshift. Here the  $s$  distribution not only accounts for the cluster to cluster variation, but also takes into account the uncertainties in the best fit LF parameters. We then calculate  $\xi$  from  $\zeta_{\text{c}}$  as described above. After applying the same selection threshold  $\xi \geq 5$ , we find that there is a  $10.7 \pm 2.4$  percent reduction in the number of galaxy clusters over the redshift range  $0.25 \leq z \leq 1.55$  in a  $2500 \text{ deg}^2$  SPT-like SZE survey. The error bars are evaluated by generating 100 realizations of the survey and sampling the  $s$  distributions as previously described. The decrease in the number counts as a function of redshift is shown in Fig. 3.8.

We fit for a power law to the ratio of cluster number counts – without and with radio galaxy contamination – of the form

$$R = A_{\text{M}} \left( \frac{(1+z)}{(1+0.6)} \right)^{C_{\text{M}}}, \quad (3.12)$$

and find  $A_{\text{M}} = 0.83 \pm 0.05$  and  $C_{\text{M}} = -0.70 \pm 0.33$ . The ratio and model uncertainties are plotted in the lower panel of Fig 3.8.

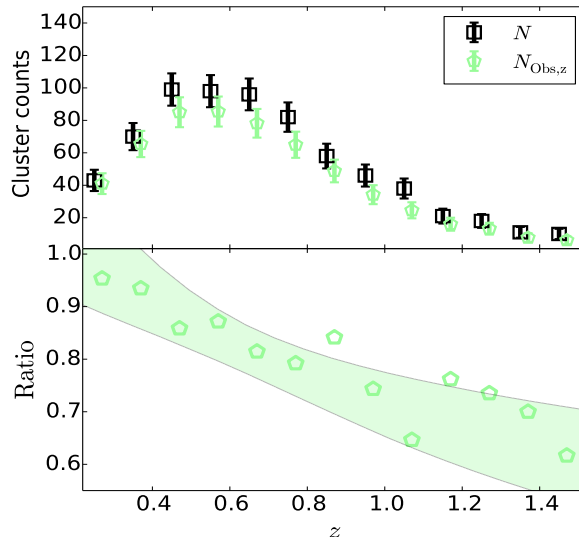


Figure 3.8: The estimated decrease in the observed number of galaxy clusters ( $N_{\text{Obs},z}$ ) due to the point source contamination as compared to the theoretical number counts ( $N$ ) for 2500 deg<sup>2</sup> of the SPT survey with  $\xi_r \geq 5$ . The shaded green region in the lower panel shows the 1- $\sigma$  model uncertainties.

### 3.5.2 Bias in Scaling Relation Parameters

We examine the bias in the  $\zeta$ –mass relation as described in equation 3.11 by selecting all clusters with  $\xi \geq 5$  in the redshift range of 0.25 to 1.5. This is done by fitting the scaling relation for  $\zeta$  and  $\zeta_c$  distributions of clusters. We find that  $A_{\text{SZ}}$  and  $C_{\text{SZ}}$  parameter values decrease by  $\sim 5$  and 37 percent, respectively and  $B_{\text{SZ}}$  increases by  $\sim 1$  percent due to the radio source contamination. This bias in scaling relation parameters is comparable with the 1- $\sigma$  parameter constraints obtained by de Haan et al. (2016) (see table 3 in their paper) using SPT number counts in addition to  $H_0$  prior and Big Bang Nucleosynthesis (BBN) datasets. Thus, it is not an important systematic for the cosmological point of view.

## 3.6 Conclusions

We construct radio luminosity functions (LFs) and radial profiles for the SUMSS selected sources at 0.843 GHz and at 95, 150 and 220 GHz frequencies by measuring the fluxes of SUMSS selected sources in appropriately filtered SPT maps. We use redMaPPer catalog from the Dark Energy Survey first year observations and look for the excess of the sources in the direction of these clusters. The median redshift of these clusters is 0.46 with the highest redshift system at  $z \sim 0.77$ . The mass of these clusters is estimated using the richness-mass relation from Capasso et al. in (prep) and the median  $M_{200c} = 1.8 \times 10^{14}$

$M_{\odot}$ .

We find that the radial profile of these sources is highly concentrated at the center of the cluster for all frequencies and is consistent with NFW model with concentration  $c \sim 170, 600$  and  $450$  at  $0.843, 95$  and  $150$  GHz, respectively. We construct the LFs assuming that the overdensity of radio galaxies towards a cluster is at the redshift of the cluster and we correct for the non-cluster sources by employing a statistical background correction. We find redshift trends in radio sources in galaxy clusters at all frequencies. The pure luminosity  $(1+z)^{\gamma_P}$  and density  $(1+z)^{\gamma_D}$  evolution at  $0.843$  GHz is of the order of  $\gamma_P = 2.21 \pm 0.46$  and  $\gamma_D = 2.32 \pm 0.41$ , respectively. At higher frequencies we find consistent but larger evolution with  $\gamma_D = 6.7 \pm 3.5$  and  $\gamma_D = 6.3 \pm 2.8$  for  $95$  and  $150$  GHz samples, respectively.

We estimate the impact of the contamination due to cluster radio galaxies on the incompleteness in SZE observed galaxy clusters from the SPT-SZ like  $2500 \text{ deg}^2$  survey at  $150$  GHz. We use LF measured at  $150$  GHz for estimating the number of galaxies for a given mass and redshift of the cluster and assign fluxes to these galaxies by using same LF as the cumulative distribution function. We take into account the cluster to cluster variation in the galaxy counts and propagate the error on the LF model to get unbiased estimations of the degree of contamination for a cluster with particular mass and redshift. We find that around  $10.7 \pm 2.4$  percent of clusters would be lost from the sample in a redshift range of  $0.25$  to  $1.55$  in  $2500 \text{ deg}^2$  SPT-SZ like survey. We find the bias in the parameters of  $\zeta$ -mass relation due to radio galaxy contamination to be not important to impact our cosmological analysis, given the posterior constraints on these parameters as presented in de Haan et al. (2016).

In our future work, we will study the impact of incompleteness in the cluster sample on the cosmological parameter estimation from SPT-SZ survey. We speculate that the incompleteness in the ongoing or upcoming SZE surveys like SPTpol (Bleem et al., 2012), SPT-3G (Benson et al., 2014) and CMB-S4 (Abazajian et al., 2015) would be even more and we are currently working to quantify incompleteness for these experiments.

## Acknowledgements

We acknowledge the support of the International Max Planck Research School on Astrophysics of the Ludwig-Maximilians-Universität, the Max-Planck-Gesellschaft Faculty Fellowship program at the Max Planck Institute for Extraterrestrial Physics, the DFG Cluster of Excellence ‘‘Origin and Structure of the Universe’’, the Transregio program TR33 ‘‘The Dark Universe’’ and the Ludwig-Maximilians-Universität. The data processing has been carried out on the computing facilities of the Computational Center for Particle and Astrophysics (C2PAP), located at the Leibniz Supercomputer Center (LRZ).

The South Pole Telescope is supported by the National Science Foundation through grant PLR-1248097. Partial support is also provided by the NSF Physics Frontier Center grant PHY-1125897 to the Kavli Institute of Cosmological Physics at the University of Chicago, the Kavli Foundation and the Gordon and Betty Moore Foundation grant GBMF

947. B. A. Benson is supported by the Fermi Research Alliance, LLC under Contract No. De-AC02-07CH11359 with the United States Department of Energy.

# Chapter 4

## SZE Observables, Pressure Profiles and Center Offsets in *Magneticum* Simulation Galaxy Clusters

N. Gupta<sup>1,2,3</sup>, A. Saro<sup>1,3</sup>, J.J. Mohr<sup>1,2,3</sup>, K. Dolag<sup>1,3,4</sup> and J. Liu<sup>1,5</sup>

<sup>1</sup> Faculty of Physics, Ludwig-Maximilians-Universität, Scheinerstr. 1, 81679 Munich, Germany

<sup>2</sup> Max Planck Institute for Extraterrestrial Physics, Giessenbachstrasse, 85748 Garching Germany

<sup>3</sup> Excellence Cluster Universe, Boltzmannstr. 2, 85748 Garching, Germany

<sup>4</sup> Max Planck Institute for Astrophysics, Karl-Schwarzschild-Str. 1, 85741 Garching Germany

<sup>5</sup> Bosch Research and Technology Center North America, CA 94304, United States

### 4.1 Abstract

We present a detailed study of the galaxy cluster thermal SZE signal  $Y$  and pressure profiles using *Magneticum* Pathfinder hydrodynamical simulations. With a sample of 50,000 galaxy clusters ( $M_{500c} > 1.4 \times 10^{14} M_{\odot}$ ) out to  $z = 2$ , we find significant variations in the shape of the pressure profile with mass and redshift and present a new generalized NFW model that follows these trends. We show that the thermal pressure at  $R_{500c}$  accounts for only 80 percent of the pressure required to maintain hydrostatic equilibrium, and therefore even idealized hydrostatic mass estimates would be biased at the 20 percent level. We compare the cluster SZE signal extracted from a sphere with different virial-like radii, a virial cylinder within a narrow redshift slice and the full light cone, confirming small scatter ( $\sigma_{\ln Y} \simeq 0.087$ ) in the sphere and showing that structure immediately surrounding clusters increases the scatter and strengthens non self-similar redshift evolution in the cylinder.

Uncorrelated large scale structure along the line of sight leads to an increase in the SZE signal and scatter that is more pronounced for low mass clusters, resulting in non self-similar trends in both mass and redshift and a mass dependent scatter that is  $\sim 0.16$  at low masses. The scatter distribution is consistent with log-normal in all cases. We present a model of the offsets between the center of the gravitational potential and the SZE center that follows the variations with cluster mass and redshift.

## 4.2 Introduction

The formation and evolution of galaxy clusters are sensitive to the expansion history of the universe and to the growth rate of structure. This makes them a promising avenue to constrain different cosmological models (e.g. Haiman et al., 2001). In recent years, the SZE, the inverse Compton scattering of cosmic microwave background (CMB) photons by hot electrons in galaxy clusters (Sunyaev & Zel’dovich, 1970, 1972), has emerged as a powerful tool to detect massive clusters out to high redshift. This distorts the CMB Planckian spectrum such that, at frequencies lower than 217 GHz, we observe a decrement in CMB flux in the direction of galaxy clusters (peaking in amplitude at 150 GHz), which enables their detection (see Birkinshaw et al., 1984; Rephaeli, 1995; Carlstrom et al., 2002).

Since Staniszewski et al. (2009) presented the first SZE selected clusters, ongoing surveys in microwave bands such as the South Pole Telescope (SPT), the Atacama Cosmology Telescope (ACT) and Planck have yielded hundreds to thousands of newly discovered clusters (e.g. Vanderlinde et al., 2010; Sehgal et al., 2011; Reichardt et al., 2013; Hasselfield et al., 2013; Bleem et al., 2015; Planck Collaboration et al., 2016c). Combined with the knowledge of cluster mass from follow-up programs and from simulations, these cluster samples provide competitive cosmological constraints (Planck Collaboration et al., 2016b; de Haan et al., 2016). However, current SZE cluster cosmology is limited by our understanding of cluster selection and mass-observable scaling relations (see, e.g., Bocquet et al., 2015; Planck Collaboration et al., 2016b). In particular, further progress requires that we develop an improved understanding of cluster pressure profiles and the expected form of mass-observable scaling relations—including the distribution of scatter and its dependence on cluster mass, redshift and radius.

A crucial issue in the calibration of the  $Y_{\text{SZE}}$ -mass relation (Johnston et al., 2007; George et al., 2012; Du & Fan, 2014; Schrabback et al., 2016) and also in understanding multiwavelength SZE, optical and X-ray scaling relations (Biesiadzinski et al., 2012; Sehgal et al., 2013; Planck Collaboration et al., 2013d; Rozo & Rykoff, 2014b; Rozo et al., 2014a,b; Saro et al., 2015, 2017) is the miscentering of the observable with respect to the center of mass of the cluster. While it has been shown that approximately 80 percent of clusters exhibit good agreement in their X-ray/SZE and brightest cluster galaxy (BCG) centers (Lin & Mohr, 2004; Sanderson et al., 2009; Stott et al., 2012; Song et al., 2012; Saro et al., 2015), providing a strong suggestion that these trace the center of mass, the behavior of the remainder of the population—presumably those clusters that have undergone recent major mergers—is more complicated. Understanding the SZE center offset distribution

for all masses and redshifts is helpful especially in analyses of stacked cluster observables where ignoring the tail of the offset distribution will lead to biases.

Assuming self similarity (Kaiser & Silk, 1986) in the galaxy cluster population, the SZE flux within a fixed critical overdensity radius scales with mass as  $Y \propto M^{5/3}$ . However, as shown with X-ray scaling relations (e.g. Mohr & Evrard, 1997; Mohr et al., 1999), physical processes underway in galaxies and the intracluster medium (ICM) can alter these scalings, producing relations that are non-self-similar. Interestingly, the SZE scaling relations are expected to be much less sensitive to ICM physics. Significant attention has been focused toward using simulations to understand the impact of ICM physics on the  $Y_{\text{SZE}}$ -mass scaling relation (e.g. Da Silva et al., 2001; White et al., 2002; McCarthy et al., 2003; Motl et al., 2005; Nagai, 2006; Bonaldi et al., 2007; Shaw et al., 2008; Battaglia et al., 2011; Kay et al., 2012). Some of the simulations used in these studies are based on pure gravitational physics complemented with the runs of the so-called Semi Analytic Models (SAMs) of galaxy evolution. These SAMs provide a realistic description of galaxy properties, but neither do they provide direct information on the properties of ICM, nor do they properly include the dynamical effects of the baryons on structure formation, which is highly relevant for the study of environmental effects.

Over the past decade, some studies have employed large scale hydrodynamical simulations that include only non-radiative physics (e.g. the Marenstrum universe, Gottloeber et al., 2006) or a crude description of star formation (e.g. the Millennium gas project, Gazzola & Pearce, 2007). Simulations with higher- though still moderate- spatial resolution and better treatment of cooling and star formation are typically only realized for relatively small simulation volumes (e.g. Borgani et al., 2004; Kay et al., 2004). Only small volumes (typically 25 Mpc/ $h$ ) are so far explored at high resolution (typically 2 Kpc/ $h$ ) and with moderate inclusion of physical processes (e.g. Tescari et al., 2009; Schaye et al., 2010). More physical processes like the description of radiative cooling of the ICM, a sub-resolution prescription to follow the formation and evolution of the stellar component and the release of energy and metals from Type II and Type Ia supernovae and asymptotic giant branch (AGB) stars are included in later simulations (e.g. Tornatore et al., 2003, 2007b; Fabjan et al., 2008). However, accurate modeling of active galactic nucleus (AGN) feedback (e.g. Fabjan et al., 2010), inclusion of transport processes like thermal conduction (e.g. Dolag et al., 2004) and consistent treatment of magnetic fields (e.g. Dolag & Stasyszyn, 2009) have allowed researchers to extend the comparison with observations towards radio wavelengths. Recently, the cosmo-OWLS suite of cosmological hydrodynamical simulations (Le Brun et al., 2014)- which includes a range of physical processes like the UV/X-ray background, cooling, star formation, supernova feedback and AGN feedback- has been explored to study group and cluster mass-observable scaling relations (Le Brun et al., 2017).

The *Magneticum Pathfinder Simulation* (MPS)<sup>1</sup> project involves a series of hydrodynamical simulations of different cosmological volumes covering a broad range of scales (Dolag et al. in, prep). These simulations allow us to examine the impact of ICM physics and to do so even within large enough volumes to enable good statistics in the study of

---

<sup>1</sup><http://www.magneticum.org/>

Table 4.1: *Magneticum* simulation box used in this work. Column 1: size of the box in Mpc. Column 2: gravitational softening length for dark matter, ICM and star particles in kpc. Column 3: number of particles in the box. Column 4: mass of each dark matter, ICM and star particle. Column 4: minimum halo mass selected to construct the final catalog for this study. Column 5: number of halos with  $M_{500c} \geq M_{500c, \min}$  in the full simulation box. Column 6: number of halos in the light cone with  $M_{500c} \geq M_{500c, \min}$ .

Size $L_{\text{box}}$ Mpc	softening length (kpc)			$N_{\text{particles}}$	$m_{\text{particle}} (M_{\odot})$			$M_{500c, \min}$ ( $M_{\odot}$ )	$N_{\text{box}}$ $z \geq 0$	$N_{\text{lc}}$ $z \geq 0$
	DM	gas	stars		DM	gas	star			
1274	10	10	5	$2 \times 1526^3$	$1.8 \times 10^{10}$	$3.7 \times 10^9$	$9.3 \times 10^8$	$1.4 \times 10^{14}$	49311	1593

rare, high mass structures like galaxy clusters (Hirschmann et al., 2014; Saro et al., 2014; Teklu et al., 2015; Bocquet et al., 2016b; Dolag et al., 2016). In this work, we study the pressure profiles and SZE cluster scaling relations using these simulations and compare them with observational results as well as previous hydrodynamical simulation studies. We study trends in pressure profiles with cluster mass and redshift and propose extensions to the standard model. We examine the offsets between the center of the cluster gravitational potential and the SZE center.

In section 4.3, we describe the simulations. The pressure profiles are examined in section 4.4, and we show the fitting results of the  $Y_{\text{SZE}}$ -mass relation in section 4.5. In section 4.6 we present the offset distributions of the gravitational & SZE centers of clusters and we summarize our findings in section 4.7.

## 4.3 Simulation

MPS has been carried out as a counterpart to ongoing, multi-wavelength surveys (DES Collaboration, 2005; The Planck Collaboration, 2006; Carlstrom et al., 2011) and to prepare for future datasets like those from eROSITA, Euclid and LSST (Merloni et al., 2012; Laureijs et al., 2011; LSST Science Collaboration, 2009). The details about the simulations will be discussed in Dolag et al. in (prep), but here we briefly summarize the most relevant features used in this work.

### 4.3.1 Simulation Method

The simulations have been carried out with P-GADGET3, an improved version of the GADGET-2 code (Springel, 2005). We use an entropy-conserving formulation of smoothed-particle hydrodynamics (SPH) (Springel & Hernquist, 2002), and a higher order kernel based on the bias corrected, sixth-order Wendland kernel (Dehnen & Aly, 2012) with 295 neighbors, which together with a low-viscosity SPH scheme allows us to properly track turbulence within galaxy clusters (Dolag et al., 2005a; Donnert et al., 2013; Beck et al., 2016).

Many physical processes are included in the simulations. We include a treatment of radiative cooling computed following the same procedure as described in Wiersma et al.

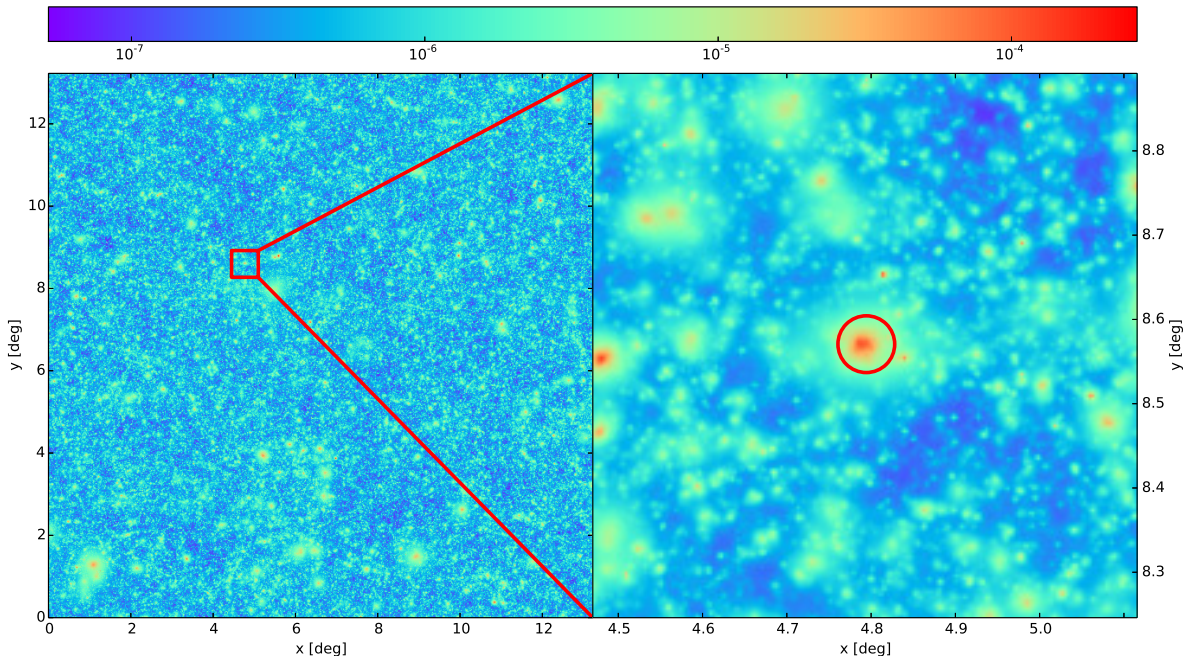


Figure 4.1: Compton- $y$  map from a simulated light cone. The left panel color codes the  $y(\theta)$  over the whole field of view and the right panel is zoomed into one massive cluster with  $M_{500c} = 3.57 \times 10^{14} M_{\odot}$  at redshift 0.67 with  $R_{500c}$  marked with a red circle.

(2009), heating by a UV background and feedback processes associated with supernovae driven galactic winds and AGN (Springel & Hernquist, 2003; Fabjan et al., 2010). We incorporate a detailed treatment of star formation (Springel & Hernquist, 2003) and chemical enrichment (Tornatore et al., 2007a). The problem of resolving Kelvin-Helmholtz and Rayleigh-Taylor instabilities within an SPH simulation is often achieved by adding an artificial transport of internal energy. Here, we are using physically motivated heat transport, with a choice of 1/20th of the classical spitzer value as motivated by MHD simulations with anisotropic conduction (Dolag et al., 2004). Finally, we include passive magnetic fields based on Euler potentials (Dolag & Stasyszyn, 2009). More information about the physical processes incorporated into MPS can be found elsewhere (e.g. Hirschmann et al., 2014; Bocquet et al., 2016b; Dolag et al., 2016).

MPS allows us to predict SZE signals from galaxy clusters with new levels of fidelity and for a large set of simulated clusters in the so-called Box1/mr (medium resolution) with  $1512^3$  dark matter particles and the same number of gas particles in a box of 1274 Mpc per side. The mass of each dark matter, gas and star particle is  $1.8 \times 10^{10} M_{\odot}$ ,  $3.7 \times 10^9 M_{\odot}$  and  $9.3 \times 10^8 M_{\odot}$ , respectively. The Plummer-equivalent softening length for gravitational forces is fixed to 10 kpc in physical units from redshift  $z = 0$  to  $z = 2$ . The WMAP7 flat  $\Lambda$ CDM cosmological parameters (Komatsu et al., 2011) are adopted, such that the variance in the density field within  $8 h^{-1}$  Mpc  $\sigma_8 = 0.809$ , the Hubble constant  $H_0 = 70.4 \text{ km s}^{-1} \text{ Mpc}^{-1}$ , the mean matter density  $\Omega_m = 0.272$ , and the mean baryon density  $\Omega_b = 0.0456$ .

MPS has been shown to reproduce the observed baryon fraction of nearby ( $z \sim 0.07$ ) halos at galaxy cluster/group mass scales but the agreement at redshift  $z \sim 0.9$  is not as good (Bocquet et al., 2016b). The X-ray luminosity-temperature relation obtained using the same simulation scheme as ours has been shown to be consistent with the observed relation from a sample of local clusters (Biffi et al., 2013). The thermal SZE power spectrum from MPS has also been shown to be consistent with Planck measurements at multipoles  $\ell$  up to  $\ell \sim 1000$  (Dolag et al., 2016).

In a series of papers, the nIFTy cluster comparison project (e.g. Elahi et al., 2016; Cui et al., 2016; Arthur et al., 2017) tests eight state-of-the-art hydrodynamical codes (including the P-GADGET3 code used for MPS), each equipped with their own calibrated subgrid physics and the same initial conditions are compared. They find large variations in the resulting abundance of haloes, sub-haloes and galaxies, depending upon the code. They also find that— with the exception of GADGET3-PESPH, which uses a stellar feedback scheme with additional quenching in massive galaxies— the simulations that do not include AGN feedback do not reproduce observed stellar and baryonic fractions either in the cluster core or in the infall regions. This underscores the importance of the subgrid physics in determining the structure of simulated clusters. Setting aside subgrid physics, the P-GADGET3 code produces clusters with ICM core structure that lies between that of the grid codes and the classical SPH codes, while in the outer regions of clusters, there are no significant differences among the codes.

### 4.3.2 Compton- $y$ Map

The SZE results in a shift of the energy distribution of the CMB photons from its blackbody spectrum. In this work, we focus on the SZE introduced by energetic electrons in the non-relativistic regime, i.e. the thermal-SZE. The amplitude of this distortion is commonly expressed in terms of CMB temperature ( $T_{\text{CMB}}$ ). At a given position ( $\theta$ ) on the sky this can be expressed as (Carlstrom et al., 2002)

$$\frac{\Delta T_{\text{CMB}}}{T_{\text{CMB}}}(\theta) = y(\theta)g(x), \quad (4.1)$$

where  $g(x) = x \coth(x/2) - 4$  is a function of frequency ( $\nu$ ) with  $x \equiv h_P \nu / k_B T_{\text{CMB}}$  and  $h_P$  and  $k_B$  are the Planck and Boltzmann constants, respectively. The projected Compton- $y$  parameter is proportional to electron pressure along the line of sight

$$y(\theta) = \frac{\sigma_T}{m_e c^2} \int P_e(\theta, l) dl, \quad (4.2)$$

where  $\sigma_T$  is the Thompson scattering cross section,  $P_e = n_e k_B T$  denotes the electron pressure and  $n_e$  is the electron number density.

The two-dimensional Compton- $y$  map is created by applying the so-called ‘gather approximation’ with the SPH kernel (Monaghan & Lattanzio, 1985), where all gas particles that project into the target pixel contribute to the total  $y$ . The gas particles are assumed

to be fully ionized with mean molecular weight per free electron  $\mu_e = 1.14$ . The details of this map-making procedure can be found in Dolag et al. (2005a). To study the projection effects on the scaling relations, we construct four light cones from randomly selected slices without rotating the simulation box. Each light cone is a stack of 27 slices extracted from the simulation box at different redshifts, such that the time interval between the slices is approximately the same ( $\sim 4 \times 10^8$  years). The field of view of each light cone is  $13 \text{ deg} \times 13 \text{ deg}$  with the maximum comoving width of  $\sim 1228 \text{ Mpc}$  at redshift 2. The depth of each slice along the z-direction ranges from  $\sim 143$  to  $471 \text{ Mpc}$ . We expect to have some duplicate structure at high redshift ( $z > 1.4$ ) in these light cones, but this duplication is negligible when we focus on massive clusters. Fig. 4.1 shows the resulting map from a light cone with  $4096^2$  pixels. These maps have a resolution of  $\sim 0.2$  arcminute per pixel and a dynamical range in  $y$  of  $10^4$  from diffuse background ( $5 \times 10^{-8}$ ) to massive clusters ( $3 \times 10^{-4}$ ).

### 4.3.3 Cluster Catalog

Clusters are first identified using the friends-of-friends (FoF) algorithm with a linking length of 0.16 (see Davis et al., 1985, and references therein), linking only the dark matter particles. For each identified cluster halo, we then implement the algorithm SUBFIND (Springel et al., 2001; Dolag et al., 2009) in parallel to compute spherical overdensity (SO) masses at different overdensities like  $M_{500c}$ ,  $M_{500m}$ ,  $M_{200c}$ ,  $M_{200m}$  and  $M_{2500c}$ . Here  $M_{500c}$  and  $M_{500m}$ , for example, describe the mass of the cluster within the region where the density is 500 times the critical and mean density of the universe, respectively. The cluster central position is recorded as the deepest gravitational potential position. For this analysis, the final catalog is selected to have clusters with  $M_{500c} > 1.4 \times 10^{14} M_\odot$  and  $z_{\text{max}} = 2$ . The mean mass and redshift of this sample are  $2.3 \times 10^{14} M_\odot$  ( $M_{500c, \text{max}} = 2.1 \times 10^{15} M_\odot$ ) and 0.31 in the full simulation box, and  $2.1 \times 10^{14} M_\odot$  ( $M_{500c, \text{max}} = 1.36 \times 10^{15} M_\odot$ ) and 0.67 in the light cones. The details about the simulation and selected clusters are given in Table 4.1.

## 4.4 Pressure Profile

A detailed study of the  $Y_{\text{SZE}}$ -mass relation of clusters requires an understanding of the pressure profile. Moreover, as mentioned already in the introduction, a matched filter cluster selection from SZE survey data can be informed by numerical simulations of clusters and their pressure profiles. In this section, we present constraints on the ICM pressure profile and also explore potential hydrostatic mass biases by comparing the ICM pressure profile with that deduced from an HSE approximation. To analyze the pressure profiles we adopt the cluster mass definition  $M_{500c}$ .

Table 4.2: Constraints on the GNFw model parameters from fits to the pressure profiles of 50,000 simulated clusters with  $\langle M_{500c} \rangle = 2.3 \times 10^{14} M_{\odot}$  and  $\langle z \rangle = 0.31$ . For each parameter— see equations (4.3) and (4.4)— we present our results (MPS) followed by literature results from another simulation (Kay et al., 2012) and observations (Planck Collaboration et al., 2013c; Arnaud et al., 2010; McDonald et al., 2014). Further discussion appears in section 4.4.1.

	MPS	K12	PL13	A10	McD14
$P_0$	$0.1701^{+0.0001}_{-0.0001}$	0.33	0.19	0.21	$0.13^{+0.12}_{-0.05}$
$c_{500}$	$1.21^{+0.01}_{-0.01}$	1.97	1.81	1.18	$2.59^{+0.74}_{-0.79}$
$\gamma$	$0.37^{+0.01}_{-0.01}$	0.61	0.31	0.31	$0.26^{+0.26}_{-0.22}$
$\alpha$	$1.23^{+0.01}_{-0.01}$	2.04	1.33	1.05	$1.63^{+1.01}_{-0.41}$
$\beta$	$5.06^{+0.03}_{-0.03}$	2.99	4.13	5.19	$3.30^{+0.86}_{-0.57}$
$\alpha_P$	$0.0105^{+0.0006}_{-0.0006}$	0.12	0.12	0.12	0.12
$c_P$	$-0.121^{+0.002}_{-0.002}$	-	-	-	-

#### 4.4.1 Pressure Profiles from the Simulations

##### Profile Construction

The pressure profile of each cluster is calculated using the properties of gas particles within 30 radial bins equally spaced logarithmically between 0.1 and  $3R_{500c}$ . We take the pressure of each bin to be the median pressure of particles in that bin, and the radial distance of the bin is the mass weighted mean radius of the particles. The particle pressure is calculated using the internal energy and density associated with each particle. The median pressure within a bin is relatively insensitive to the significantly different pressures exhibited by multiphase gas particles.

We follow the variation of the pressure about the median using the 16<sup>th</sup> and 84<sup>th</sup> percentiles of the distribution. The ICM pressure profiles are constructed for  $\sim 50,000$  clusters in the full simulation box (see Table 4.1). The mean mass and redshift of the sample are  $\langle M_{500c} \rangle = 2.3 \times 10^{14} M_{\odot}$  and  $\langle z \rangle = 0.31$ .

##### Profile Fitting

We adopt the generalized NFW model (GNFW, Nagai et al., 2007) for fitting the pressure profile. This model has been found to be a good description for the cluster ICM pressure profile in cosmological simulations (e.g. Nagai et al., 2007; Kay et al., 2012) and in X-ray/SZE observations of real clusters (e.g. Arnaud et al., 2010; Plagge et al., 2010; Sun et al., 2011). The pressure  $P_{\text{mod}}(r, M, z)$  as a function of cluster mass ( $M$ ) and redshift ( $z$ ) is written as

$$P_{\text{mod}}(r, M, z) = P_{500}(M, z) \frac{c_{500}^{\gamma} (1 + c_{500}^{\alpha})^{(\beta-\gamma)/\alpha}}{(c_{500} x)^{\gamma} [1 + (c_{500} x)^{\alpha}]^{(\beta-\gamma)/\alpha}}, \quad (4.3)$$

where the parameters  $\gamma$ ,  $\alpha$ , and  $\beta$  are the central ( $r \ll r_s$ ), intermediate ( $r \sim r_s$ ), and outer slopes ( $r \gg r_s$ ). Also, here  $r_s = R_{500c}/c_{500}$ ,  $x = r/R_{500c}$  and  $c_{500}$  is the concentration. The overall pressure scale  $P_{500}$ , representing the pressure at  $R_{500c}$ , is written as

$$P_{500}(M, z) = 1.65 \times 10^{-3} P_0 E(z)^{8/3+c_P} \left[ \frac{M_{500c}}{3 \times 10^{14} M_\odot} \right]^{2/3+\alpha_P} \text{keV cm}^{-3}, \quad (4.4)$$

where  $P_0$  is the dimensionless normalization and  $E(z) = H(z)/H_0$ . The parameters  $c_P$  and  $\alpha_P$  denote the departures from self-similarity of the pressure profile scale with redshift and mass, respectively (see Arnaud et al., 2010). Note that our model differs slightly from that used in previous studies; specifically, the factor  $c_{500}^\gamma (1 + c_{500}^\alpha)^{(\beta-\gamma)/\alpha}$  ensures that at  $r = R_{500c}$ ,  $P_{\text{mod}}(r, M, z)$  is equivalent to  $P_{500}(M, z)$ , independent of the value of  $c_{500}$  and the slope parameters.

We use the Markov Chain Monte Carlo (MCMC) code, `emcee` (a Python implementation of an affine invariant ensemble sampler; Foreman-Mackey et al., 2013) to fit the model to the data throughout this paper. The pressure profile is constrained by the sum of the log likelihood of the individual clusters  $j$

$$\log \mathcal{L} = -\frac{1}{2} \sum_{i,j} \frac{\ln[P_{\text{sim}}(i, j)/P_{\text{mod}}(r_i, M_j, z_j)]^2}{(\sigma_{\text{lnP,SPH}}^2(i, j) + \sigma_{\text{lnP}}^2(i))}, \quad (4.5)$$

where  $P_{\text{sim}}(i, j)$  is the median pressure for cluster  $j$  in different radial bins  $i$  (between  $0.1R_{500c}$  and  $3R_{500c}$ ) from the simulation and  $P_{\text{mod}}(r_i, M_j, z_j)$  is the corresponding value from the model.  $\sigma_{\text{lnP,SPH}}(i, j)$  is the log-normal particle to particle scatter determined for each cluster  $j$  as half the difference between the 16<sup>th</sup> and 84<sup>th</sup> percentile pressure divided by the square root of the number of particles in each radial bin  $i$ . The additional scatter term  $\sigma_{\text{lnP}}(i)$  is the characteristic intrinsic logarithmic cluster to cluster scatter, which we derive iteratively from the full cluster sample. First, we calculate the cluster to cluster variation in the median pressure profile in each radial bin and adopt it while determining the best fit model. Then we extract the cluster to cluster intrinsic scatter in each radial bin with respect to the best fit model and use that updated information to determine the best fit model again. We iterate until the resulting intrinsic scatter profile converges.

The pressure profile from the simulation is shown in Fig. 4.2. In the upper panel, the solid red line marks the median pressure profile of all clusters where the pressure for individual clusters in a radial bin is the median pressure of the particles in that bin. The dashed red lines show the variation of the pressure profiles from cluster to cluster. Because the variation around the median pressure is much smaller than the cluster to cluster variation in pressure, we do not show it in the plot. The model parameters are reported in Table 4.2 as the most likely values with 68 percent confidence intervals. Note that  $P_0$  and the uncertainty for these reference studies is re-normalized to take into account the factor of  $c_{500}^\gamma (1 + c_{500}^\alpha)^{(\beta-\gamma)/\alpha}$  as in equation (4.4). In calculating the rescaled uncertainties, we do not apply corrections for the degeneracies among the slope parameters.

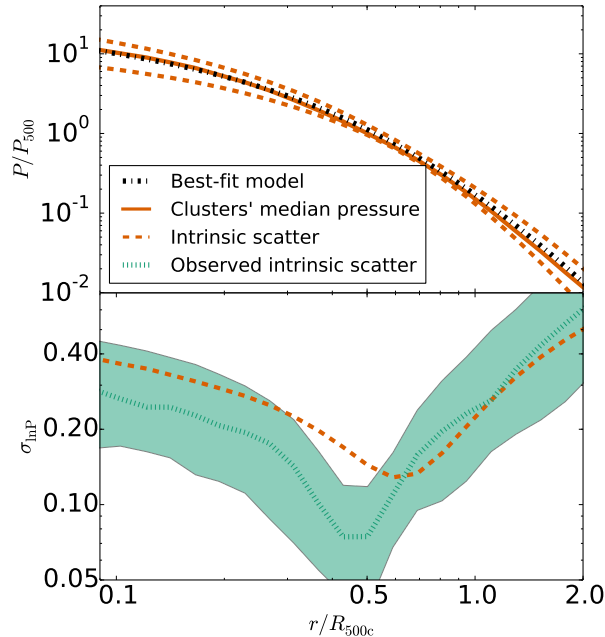


Figure 4.2: The best-fit pressure profile model (black dot-dashed line) derived from 50,000 clusters in the full simulation box with  $\langle M_{500c} \rangle = 2.3 \times 10^{14} M_{\odot}$  and  $\langle z \rangle = 0.31$ . The solid red line shows the median pressure for all clusters, and the dashed red lines mark the intrinsic cluster to cluster scatter  $\sigma_{\text{inP}}$  about the best fit model. This scatter also appears in the lower panel, where for comparison we show the intrinsic scatter of 31 clusters from Arnaud et al. (2010) (dotted green line). The filled green region is the  $1\text{-}\sigma$  bootstrapped uncertainty on the observed intrinsic scatter.

The lower panel of Fig. 4.2 shows the derived intrinsic scatter as a function of radius. For comparison, we also present the observed intrinsic scatter (along with  $1\text{-}\sigma$  error bars derived by bootstrapping) in the individual pressure profiles of 31 galaxy clusters presented in table C.1 by Arnaud et al. (2010). The scatter is large in both the central and the outer part of the cluster and reaches a minimum at about  $0.5R_{500}$ . We expect that this is because of the variable AGN activity in the cluster cores (see, e.g., Gupta et al., 2017b) and because of the cluster mergers and infalling field population in the outer regions. The cluster to cluster variation in the pressure profiles dominates over the cluster specific scatter within each radial bin, and therefore the latter does not impact the best fit model.

### Variations of Profile Shape With Mass and Redshift

As a next step we examine whether the ICM pressure profiles exhibit systematic shape variations with mass and redshift. To probe for mass dependent trends we explore the behavior of the pressure profiles within six mass bins within each of two redshift ranges:  $z < \bar{z}$  &  $z \geq \bar{z}$ , where  $\bar{z}$  is the median redshift of the whole sample. To probe for redshift

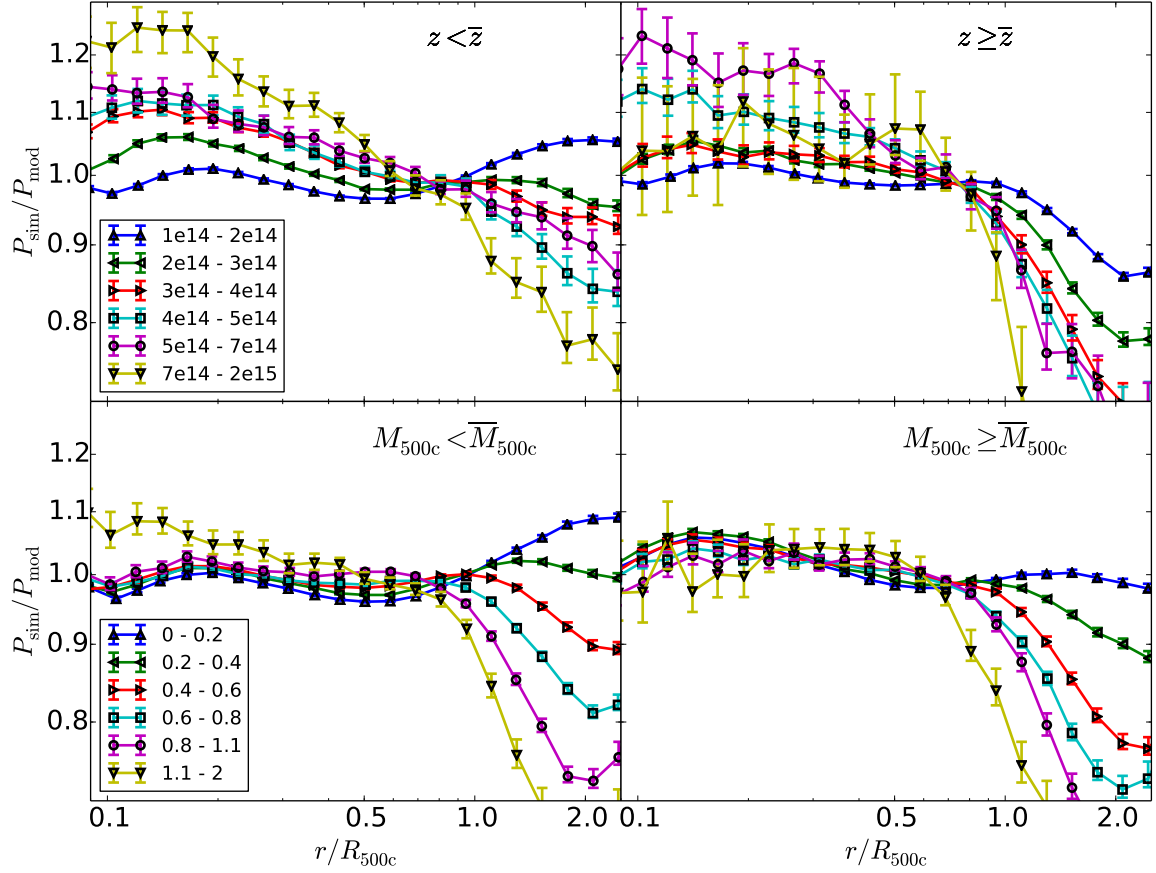


Figure 4.3: Pressure comparison in bins of mass (above) and redshift (below) of clusters with respect to the best fit model from the full sample. When probing for trends in mass (redshift) we subdivide the sample around the median value of redshift (mass) that is equivalent to 0.3 ( $2.3 \times 10^{14} M_{\odot}$ ). The data points mark the median of the ratio between pressure from simulations and best fit model in the radial bins and the error bars are  $1-\sigma$  uncertainties. There are clear indications of trends in mass and redshift which are more significant in the inner and outer regions of clusters, indicating that there is no universal pressure profile.

dependent trends we study the behavior of the pressure profiles within six redshift bins for each of two mass ranges:  $M_{500c} < \overline{M}_{500c}$  &  $M_{500c} \geq \overline{M}_{500c}$ , where  $\overline{M}_{500c}$  is the median mass of the whole sample. The clusters are selected from the full simulation box and divided into various bins so that there are at least 200 clusters in each bin. For the bins where the number of clusters is very large, we select a random subset of 200 clusters.

We calculate the ratios between the pressure from simulations and the best fit model (as described in section 4.4.1) within each of the bins. Fig. 4.3 shows the trends in pressure as a function of mass (above) and redshift (below). The points represent the median of the ratios in each radial bin, and the error bars indicate the uncertainties in the median that are calculated as the standard deviation in each bin divided by the square root of the number of clusters in the bin.

These plots show clear mass and redshift trends in the shape of the ICM pressure profile, especially in the inner and outer parts of clusters. These differences are what drive the larger intrinsic scatter measured in these radial regions of clusters (as shown in the lower panel of Fig. 4.2 and discussed in section 4.4.1). These variations are due to the trends in AGN activity and its impact on the core and trends within the infall regions with redshift and mass. AGN provide feedback in central cluster regions, impacting the pressure profile in a mass dependent manner. In the outskirts, deviations from the model also vary with mass and redshift, in agreement with a simulation study by Battaglia et al. (2012b), where they examined a detailed dependency of pressure profiles on cluster radius, mass and redshift. At different redshifts, the inner regions of clusters show better self similarity as compared to cluster outskirts where the deviations increase with increasing redshift because of larger mass accretion rate at early times (Shi & Komatsu, 2014). Following Lau et al. (2015), where they investigate the self-similarity of the diffuse X-ray emitting ICM in the outskirts of galaxy clusters, we normalize our pressure profiles using mean density ( $\rho_m$ ) of universe instead of critical density ( $\rho_c$ ) to see if that has any impact. We also find better self similarity in the outer pressure profiles at different redshifts, when mean density is used. However, the inner profiles become less self similar as compared to the scenario where critical density is used. This behavior may be an indication that the outer gas profiles are dependent on the late time mass accretion, which is governed by the mean density of the universe, whereas the inner profiles are dependent on the gravitational potential, which is set when the universe was still matter dominated and stays roughly constant afterwards (Lau et al., 2015).

These highly significant variations of median pressure profile with mass and redshift indicate that there is no universal pressure profile. Indeed, the pressure profile model we adopt in our analysis of the full sample is insufficient to follow the effects of complex, location dependent physics within the cluster population. We explore a few possible extensions to this simple GNF model and present the best performing one for these MPS simulations in appendix 4.8. We also probe for trends with redshift and mass in the evolution of the intrinsic scatter in the pressure profile deduced from the best fit model, but we find no evidence for such trends.

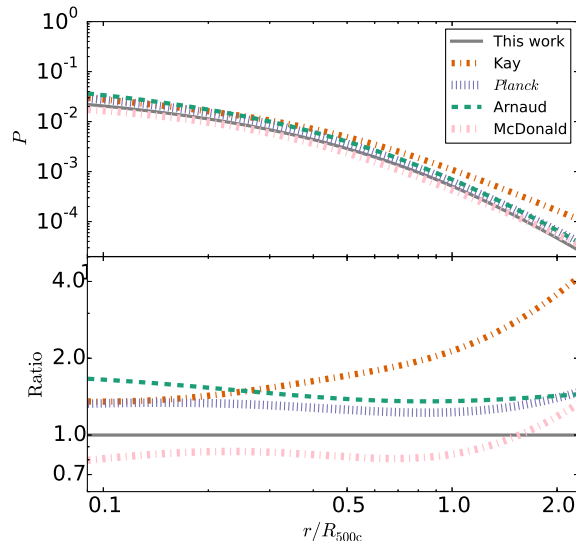


Figure 4.4: The comparison of the pressure profiles from the *Magneticum* simulations with the profiles from Kay et al. (2012), Arnaud et al. (2010), Planck Collaboration et al. (2013c) and McDonald et al. (2014). These profiles are constructed for a cluster mass of  $M_{500c} = 5 \times 10^{14} M_{\odot}$  at  $z = 0$ . The best fit values are stated in Table 4.2. The lower panel shows the ratio between the pressure profiles with respect to the profile obtained in this work.

### Comparison With Previous Studies

We compare our results with previous simulation (Kay et al., 2012) and observational studies (Planck Collaboration et al., 2013c; Arnaud et al., 2010; McDonald et al., 2014), taking care to re-normalize to our functional form to allow for a direct comparison. The parameter constraints from our sample and the best fit from their analysis are shown in Table 4.2 and Fig. 4.4.

On the simulation side, Kay et al. (2012) analyzed the *Millennium Gas Simulations* complemented with SAMs of galaxy formation and found that the cluster ICM pressure profile can be well described by the GNFW model. They consider a feedback-only (FO) model (Short & Thomas, 2009) for analyzing the SZE properties of clusters. Their sample is split into high mass ( $M_{500c} > 6.8 \times 10^{14} M_{\odot}$ ) and low mass ( $1.37 \times 10^{14} M_{\odot} \leq M_{500c} \leq 6.8 \times 10^{14} M_{\odot}$ ) clusters at  $z = 0$  and 1.

On the observational side, pressure profiles have been reconstructed (Arnaud et al., 2010) from X-ray observations of the REXCESS cluster sample (Böhringer et al., 2007) at low redshift for  $r < R_{500c}$  and from numerical simulations for  $r > R_{500c}$ . This allows us to compare our simulated pressure profiles to the observed profiles within the inner cluster region. The best fit parameters of the GNFW model from Arnaud et al. (2010) are also listed in Table 4.2. The Planck collaboration (Planck Collaboration et al., 2013c) derived the pressure profiles using XMM-*Newton* data for 62 massive, nearby clusters (mostly

at  $z < 0.3$ ) in a large radial range out to  $3 \times R_{500c}$ , which allows us to compare the pressure profiles outside  $R_{500c}$  as well. An SPT collaboration analysis of *Chandra* X-ray observations of 80 SZE selected clusters (McDonald et al., 2014) divides the sample into low- $z$  ( $0.3 < z < 0.6$ ) and high- $z$  ( $0.6 < z < 1.2$ ) clusters. Their analysis primarily constrains the  $r < 1.5R_{500c}$  region of the clusters.

The comparison among the best fitting pressure profiles is shown in Fig. 4.4 for a cluster with  $M_{500c} = 5 \times 10^{14} M_{\odot}$  at  $z = 0$ . The simulated profiles from Kay et al. (2012) are much flatter in the outer region of the cluster, which is reflected in the smaller outer slope ( $\beta$ ) of the GNF model. This parameter is found to be larger in observational studies as well as in our current work. As mentioned in Kay et al. (2012), they find higher thermal ICM pressure in the outskirts of the clusters due to the absence of radiative cooling.

Overall, our simulated profiles are comparable in shape to the observed pressure profiles. However, the observed profiles derived from XMM observations (Arnaud et al., 2010; Planck Collaboration et al., 2013c) exhibit a systematically higher pressure at the 30 to 40 percent level. The *Chandra* derived results (McDonald et al., 2014) exhibit somewhat lower pressure at the 10 to 20 percent level in the radial range  $0.1 - 1 \times R_{500c}$ , where the pressure profile is well constrained by the data. The comparison with observed properties is, however, further complicated by the different mass calibrations adopted by different authors as discussed in detail in Saro et al. (2017). As a result, differences emerge not only in the predicted pressure at fixed radius (in  $R_{500c}$  units), but also on the scale associated to the characteristic radius. In summary, there is still significant disagreement in the XMM and *Chandra* inferred pressure profiles, with the profiles from our simulations lying roughly in the middle.

### Tests of Self-Similar Scaling

It is worth noting that we have freely varied two parameters to constrain deviations from self-similar scaling of the cluster pressure normalization  $P_{500}(M, z)$  with cluster mass and redshift. This has not been done in previous analyses. We find that  $c_P = -0.121 \pm 0.002$ , indicating that the pressure normalization scales as  $P_{500} \propto E(z)^{2.55}$  rather than the self-similar expectation of  $8/3$ . This means that the pressure at a fixed cluster mass is increasing slightly less rapidly with redshift than in a self-similar model.

The parameter that describes the deviation from self-similar scaling of the pressure with the cluster mass is also inconsistent with zero ( $\alpha_P = 0.0105 \pm 0.0006$ ). The expected increase in pressure at a fixed redshift with mass is marginally steeper than the expected  $2/3$  within a self-similar model.

The non-self-similar evolution in the pressure normalization with mass and redshift reflects the mix of complex physics in the simulation that affects the amount of ICM in the cluster virial region and its thermal energy. Avestruz et al. (2016) studied a mass-limited sample of galaxy clusters from cosmological hydrodynamical simulations and showed that the departure of temperature profiles from self-similar scaling in the outskirts of clusters can be explained by non-thermal gas motions driven by mergers and accretion. In our case the small departure from self-similar scaling with redshift could be caused, for example,

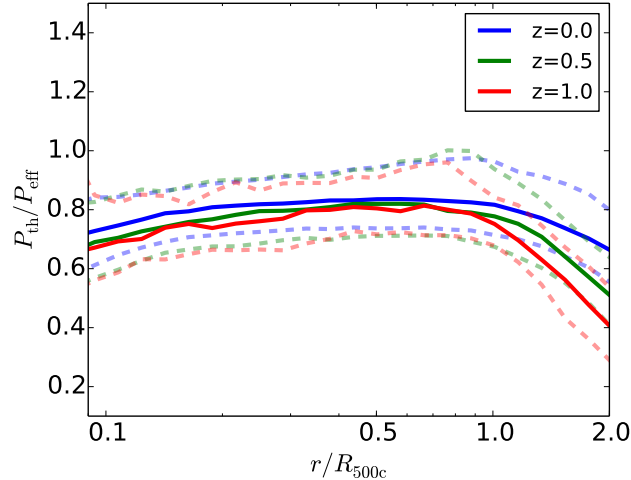


Figure 4.5: Ratio of the thermal gas pressure ( $P_{\text{th}}$ ) to the HSE derived effective pressure ( $P_{\text{eff}}$ ) for all the clusters in the light cone at three different redshifts. The solid lines show the median of the ratio and the dashed lines indicate the 16<sup>th</sup> and 84<sup>th</sup> percentiles of the ratio, in different radial bins.

by the ongoing feedback from star formation and AGN in the simulations. In the case of the mass scaling of the pressure at  $R_{500}$  it is clear that any increase in the ICM mass fraction with mass (e.g. Mohr et al., 1999) must be almost perfectly offset by a slightly lower temperature than expected within self-similarity. These offsetting effects have indeed been noted in previous simulations (Kravtsov et al., 2005, 2006).

#### 4.4.2 Effective Pressure $P_{\text{eff}}$ Assuming HSE

When a galaxy cluster is in a relaxed state, HSE pertains and the pressure profile is simply related to the mass density profile of the cluster, which can be described by a regular Navarro-Frenk-White profile (hereafter NFW; Navarro et al., 1997). In HSE there is a balance between the pressure gradient and the centrally directed gravitation attraction of the cluster on the cluster gas

$$\frac{dP}{dr} = -\frac{GM(r)\rho_{\text{ICM}}(r)}{r^2}, \quad (4.6)$$

where  $M(r)$  is the total mass enclosed within radius  $r$  and  $\rho_{\text{ICM}}(r)$  is the ICM density at radius  $r$ . This relation has often been assumed in deriving the masses of galaxy clusters with X-ray observations, and those masses will only be accurate if in fact HSE pertains. Here we derive the effective pressure profile and compare it to the actual thermal pressure profile in the simulated clusters.

### Effective Pressure Profile Construction

The mass of each particle, including not only dark matter and gas particles but also star and black hole particles, is summed to get the total enclosed mass as a function of radius for each simulated cluster. The gas particles are also summed separately in radial bins, providing an estimate of the gas mass that is translated into the mean gas density using the volume of the radial bins. These ingredients, i.e the total mass and gas mass profiles, together with a boundary condition, which is the thermal gas pressure measured in the simulations at  $3 \times R_{500c}$ , enable us to estimate an effective pressure profile  $P_{\text{eff}}(r/R_{500})$  within each cluster. If the thermal pressure in a cluster were to match this effective pressure, the cluster would by definition be in HSE.

### Hydrostatic Mass Bias

We compare the HSE derived effective pressure profiles ( $P_{\text{eff}}$ ) to the thermal gas pressure profiles ( $P_{\text{th}}$ ). Fig. 4.5 shows the ratio between the thermal gas pressure and the effective pressure. The median ratio from the cluster sample along with 16<sup>th</sup> and 84<sup>th</sup> percentile ratios (reflecting the cluster to cluster variation) is plotted in different radial bins at three different redshifts. The thermal gas pressure is always smaller than the effective pressure, implying that there must be some non-thermal pressure ( $P_{\text{nth}}$ ) support, that the cluster is still collapsing or both. Assuming large non-thermal pressure support we can write

$$P_{\text{Eff}} = P_{\text{th}} + P_{\text{nth}}. \quad (4.7)$$

The median ratio of  $P_{\text{th}}/P_{\text{eff}}$  for all clusters at a radius around  $R_{500c}$  is  $\sim 80$  percent at  $z = 0$  and is slightly lower at  $z = 0.5$  and  $z = 1$ . At all redshifts there is a tendency for the ratio to fall at larger radii, reaching values of between 40 and 65 percent at  $R_{200}$ . Because of this persistently low ratio of thermal to effective pressure, the masses obtained assuming HSE would be systematically biased low with respect to the true mass of the cluster at approximately the level of  $1 - P_{\text{th}}/P_{\text{eff}} \sim 20$  percent at  $R_{500c}$ . In addition to trends with redshift, we also studied possible variations in the HSE bias with cluster mass. We find a slightly lower bias ( $1 - P_{\text{th}}/P_{\text{eff}} \sim 15$  percent) for high mass systems ( $M_{500c} > 4 \times 10^{14} M_{\odot}$ ) in the region between  $0.5R_{500c}$  and  $1R_{500c}$  as well as in central region of clusters ( $r < 0.2R_{500c}$ ). There is smaller mass dependence in the outskirts of clusters with reversed trends i.e. slightly larger bias for high mass systems.

Similar results were obtained by Battaglia et al. (2012a), where they estimated the HSE mass estimates from  $P_{\text{th}}$  and compared this mass with the true mass of clusters in hydrodynamical simulations with AGN feedback at  $z = 0$ . Rasia et al. (2012) compared weak lensing and X-ray masses of the 20 most massive simulated galaxy clusters at  $z = 0.25$  and noted a bias of 25-35 percent due to non-thermal pressure support and temperature inhomogeneities. Biffi et al. (2016) investigated the level of HSE in the intra-cluster medium of simulated galaxy clusters and found an average deviation of 10-20 percent out to the virial radius, with no evident distinction between cool-core and non-cool-core clusters. Chiu & Molnar (2012) tested the HSE assumption for cluster MS-2137 using *Chandra* X-ray observations combined with strong and weak lensing results from optical surveys and

found a large contribution from the non-thermal pressure to the effective pressure in the cluster core, assuming a spherical model for the cluster.

In an older work, Nagai et al. (2007) found that HSE estimates of the cluster mass using X-ray data can underestimate the true mass by 15 percent. Recent comparisons of Planck collaboration hydrostatic masses to weak lensing masses over a similar redshift range indicated a tendency for the hydrostatic masses to be between 25 and 35 percent smaller, but with large uncertainties (von der Linden et al., 2014b; Hoekstra et al., 2015; Planck Collaboration et al., 2016b). Within the SPT collaboration, a comparison of hydrostatically calibrated masses to those derived from galaxy cluster velocity dispersions or from a calibration using the cluster mass function and external cosmological information also indicate that the hydrostatic masses are smaller at between 25 percent and 45 percent, respectively (Bocquet et al., 2015).

In a recent work, Shi et al. (2015) looked into 65 clusters in a set of high-resolution cosmological hydrodynamical simulations (Nelson et al., 2014) and found  $21 \pm 5$  percent bias between the mass obtained assuming HSE and the true mass from simulations. Contrary to our findings, they also found a decline in  $1 - P_{\text{th}}/P_{\text{eff}}$  towards the center of the cluster which is possibly due to the non-radiative nature of simulations used in their work. AGN feedback injected in MPS would push the gas from the center that decreases the thermal component and might also add to gas motions leading to higher non-thermal pressure towards the center. However, our results are consistent towards larger radii, where  $P_{\text{th}}/P_{\text{eff}}$  decreases as it would take a longer time to thermalize the non-thermal motions in cluster outskirts. Our results are also consistent with the fact that the non-thermal pressure support increases with redshift, perhaps due to a larger accretion rate in cluster outskirts at early times.

Several mechanisms have been proposed to understand the origin of non-thermal pressure in galaxy clusters. For instance, it has been shown that non-thermal pressure support originates from sub-sonic turbulent motions of the ICM (Evrard, 1990; Rasia et al., 2004; Dolag et al., 2005b; Rasia et al., 2006; Nagai et al., 2007). Fang et al. (2009) and Lau et al. (2009), investigating the same sample of clusters simulated by Nagai et al. (2007), found that the coherent rotation of gas plays a significant role providing additional support against gravity; on the other hand, Lau et al. (2009) claimed that random gas motion and gas rotations have a negligible role in driving the departure from HSE. Generally, the amount of energy in these bulk motions is of the order of 20-30 percent within the virial radius (Battaglia et al., 2010; Burns et al., 2010). Cosmic rays in clusters can also contribute to the non-thermal pressure support. Generally speaking, the contribution of cosmic rays is estimated to be less than 30 percent of the thermal pressure in the cluster core (Ensslin et al., 1997; Pfrommer, 2008; Sijacki et al., 2008). Such a study of the origin of non-thermal pressure is beyond the scope of this paper, but we plan to study these mechanisms in future work.

## 4.5 SZE Observable-Mass Relation

In this section we present the SZE observable-mass scaling relations from our simulations and compare them to observational results and to previous studies of simulations. We analyze the  $Y$ -mass relation for: (1) the spherically enclosed  $Y_{\text{sph}}$  using different mass and virial radius definitions, (2) the cylindrical signal  $Y_{\text{cyl}}$  that captures the projection effects within a redshift slice of width  $\sim 400$  Myr (see section 4.3.2), and (3)  $Y_{\text{lc}}$  from the projected light cones that include structure over the full redshift range extending to  $z = 2$ . By comparing these three relations we hope to be able to understand the impact of correlated or nearby structures as well as uncorrelated structures randomly superposed along the line of sight.

We adopt a power law relationship between  $Y_{\text{SZE}}$  and mass of the form

$$Y_{\text{sph},\Delta} = 10^A \left[ \frac{M_{\Delta}}{2.84 \times 10^{14} M_{\odot}} \right]^B \left[ \frac{E(z)}{E(0.6)} \right]^C \text{Mpc}^2, \quad (4.8)$$

where  $\Delta$  defines the overdensity used for the construction of the scaling relation.  $A$  and  $B$  are the fitting parameters for the normalization and mass slope of the relation, while the  $C$  parameter describes the redshift evolution. The self-similar expectations are  $B = 5/3$  and  $C = 2/3$ , where this is valid for  $C$  only in the case that  $\Delta$  is defined with respect to the critical density. Scaling relations of this form have been commonly used in simulations (e.g. Kay et al., 2012; Battaglia et al., 2012a) and observations (e.g. Planck Collaboration, 2011; Planck Collaboration et al., 2013b), in a slightly different form. For instance, Kay et al. (2012) do not normalize the redshift evolution term by the factor of  $E(0.6)$  as they only have clusters at  $z = 0$  or  $z = 1$ , and in the Planck analysis (Planck Collaboration, 2011) they measure the intrinsic SZE signal by taking into account the angular diameter distance ( $D_{\text{A}}$ ) dependence on the observed signal. In addition to the power law scaling relation in mass and redshift listed in equation (4.8), we adopt a redshift and mass independent log-normal scatter  $\sigma_{\text{ln}Y}$  that is varied along with the other parameters. The scaling relation is constrained by the log likelihood function of a similar form to that described in equation (4.5).

### 4.5.1 Spherical $Y_{\text{sph},\Delta} - M_{\Delta}$ Relation

We study the spherical  $Y$ -mass relation for different overdensities with respect to the critical density and mean density of the universe (as mentioned in section 4.3.3). The SZE signal  $Y_{\text{sph},\Delta}$  for each cluster is calculated using the ICM pressure distribution within a sphere of the appropriate radius centered on the cluster and is compared with the model as in equation 4.8. The MCMC results are shown in Table 4.3 and are evaluated using all clusters in the full simulation box with mass larger than  $1.4 \times 10^{14} M_{\odot}$  as mentioned in section 4.3.3.

We find that the normalization  $10^A$  falls systematically from the lowest mass definition  $M_{2500c}$  (smallest radius) to the highest mass definition  $M_{200m}$  (largest radius), but the differences are rather small. This is due to the falling radial pressure profile as discussed

Table 4.3: The parameter constraints for the  $Y_{\text{sph},\Delta} - M_{\Delta}$  scaling relations. The *Planck* result is converted from Table 6 in Planck Collaboration (2011) to our form of the scaling relation, and the Kay result is from the feedback-only model at  $z = 0$  in Table 3 in Kay et al. (2012) where the normalization is re-defined to be consistent with our relation.

$M_{\Delta}$	$A$	$B$	$C$	$\sigma_{\ln Y}$
$M_{200\text{m}}$	$-4.962 \pm 0.001$	$1.661 \pm 0.003$	$1.221 \pm 0.009$	$0.1225 \pm 0.0007$
$M_{500\text{m}}$	$-4.829 \pm 0.002$	$1.660 \pm 0.003$	$1.386 \pm 0.013$	$0.1110 \pm 0.0009$
$M_{200\text{c}}$	$-4.896 \pm 0.001$	$1.664 \pm 0.003$	$0.543 \pm 0.010$	$0.1068 \pm 0.0009$
$M_{500\text{c}}$	$-4.758 \pm 0.002$	$1.695 \pm 0.005$	$0.571 \pm 0.015$	$0.0875 \pm 0.0011$
$M_{2500\text{c}}$	$-4.456 \pm 0.018$	$1.850 \pm 0.063$	$0.892 \pm 0.157$	$0.1361 \pm 0.0088$
Kay $M_{500\text{c}}$	$-4.832 \pm 0.003$	$1.69 \pm 0.02$	$2/3$	$0.099$
<i>Planck</i> $M_{500\text{c}}$	$-4.769 \pm 0.013$	$1.783$	$2/3$	-

in section 4.4. Interestingly, similar behavior is noticed in an analytical study by Shi & Komatsu (2014), where they show that the non-thermal pressure is increasing with mass, redshift and radius.

The mass slope parameter  $B$  at the three largest radii ( $\Delta = 200\text{c}$ ,  $500\text{m}$  and  $200\text{m}$ ) is consistent with the self-similar expectation. At the smaller radius  $\Delta = 500\text{c}$  the slope is slightly steeper than self-similar and at  $\Delta = 2500\text{c}$ , the smallest radius we probe here, the slope is much steeper than self-similar. This is an indication that the physical heating and cooling processes modeled in the simulations are having a larger impact on the ICM distribution in the central regions of the cluster.

The redshift variation parameter  $C$  shows quite a range of values. For  $\Delta$  values defined with respect to critical the self similar expectation is  $2/3$ , and for  $200\text{c}$  and  $500\text{c}$  the scaling is significantly weaker than this. For  $2500\text{c}$ , the central most region of the cluster, the scaling is stronger than self-similar. Here again, the suggestion is that the cooling and heating processes modeled in the simulations are affecting the redshift evolution of the cores and outskirts of clusters in different ways. This is consistent with our profile results that suggest the shape of the pressure profile is changing with redshift.

For cases where  $\Delta$  is defined with respect to the mean density, the redshift evolution is different because the mean density scales as  $\rho \propto (1+z)^3$  as opposed to the critical density scaling as  $\rho_{\text{crit}} \propto E^2(z)$ . Because  $\rho(z) = \Omega_{\text{m}}(z)\rho_{\text{crit}}(z)$ , the scaling relations built using overdensities with respect to mean density  $\Delta_{\text{m}}$  exhibit not only the evolution of  $\rho_{\text{crit}}$  seen in the scaling relations using the critical overdensity, but also the evolution of the density parameter from  $\Omega_{\text{m}} = 0.3$  at  $z = 0$  to  $\Omega_{\text{m}} \sim 1$  at higher redshift. This generically leads to more rapid redshift evolution in the  $\Delta_{\text{m}}$  relations and thus higher values of  $C$ . Moreover, the physical regions corresponding to  $200\text{m}$  or  $500\text{m}$  are correspondingly larger than those for  $200\text{c}$  and  $500\text{c}$ , and thus any differences in the evolution of the cores and outskirts will lead to differences in the redshift evolution of the critical and mean relations.

The log-normal scatter  $\sigma_{\ln Y}$  falls from 0.12 at  $\Delta = 200\text{m}$  to 0.09 at  $\Delta = 500\text{c}$ , corresponding to a  $\sim 30$  percent improvement in the regularity of these clusters within  $500\text{c}$  as

Table 4.4: The parameter constraints for the  $Y - M_{500c}$  scaling relation for spherical and projected SZE signals.  $Y_{\text{sph}}$  represent the spherical signal,  $Y_{\text{cyl}}$  is the cylindrical signal in redshift slices,  $Y_{\text{lc}}$  is the signal from the whole light cone and  $\langle Y_{\text{lc}} \rangle$  is the signal that captures the large scale structure contribution along the line of sight, which is measured using the halo mass function.  $\sigma_{\ln Y}$  is derived assuming mass and redshift independence and has the same error bars  $\simeq 0.002$  for all the cases.

Obs	$A$	$B$	$C$	$\sigma_{\ln Y}$
$Y_{\text{sph}}$	$-4.753 \pm 0.002$	$1.68 \pm 0.01$	$0.55 \pm 0.01$	0.088
$Y_{\text{cyl}}$	$-4.697 \pm 0.002$	$1.65 \pm 0.01$	$0.45 \pm 0.02$	0.102
$Y_{\text{lc}}$	$-4.649 \pm 0.002$	$1.55 \pm 0.01$	$0.24 \pm 0.02$	0.159
$\langle Y_{\text{lc}} \rangle$	$-4.643 \pm 0.002$	$1.51 \pm 0.02$	$0.21 \pm 0.02$	-

compared to 200m. However, in the very central region  $\Delta = 2500c$  the scatter is 0.14, indicating that the central core region is the most varied due to the complex physical processes included in the simulation and their impact on the cluster cores. This radial dependence of the scaling relation scatter is consistent with the radial dependence of the intrinsic scatter in the pressure profile as shown in Fig. 4.2.

In Table 4.3, we also show the scaling relation parameters from two past analyses. Because the relations used in these studies are slightly different than ours, we convert the best fit values in accordance with the fitting relation in equation 4.8. Kay et al. (2012) vary normalization  $A$  and slope  $B$  of the relation, but keep the  $C$  parameter – that models the redshift evolution of the relation – fixed to the self-similar value. Our analysis shows that self-similar redshift evolution is not a good description of our simulated cluster ensemble. They also calculate the scatter about the best fit relation. Our log-normal scatter about the  $Y_{500c} - M_{500c}$  relation is similar to theirs. The mass slope of the relation is also consistent, preferring a scaling that is slightly steeper than self similar but with a factor of four larger uncertainty. The preferred normalization in our analysis is  $\sim 17$  percent higher than theirs.

We also show observational results from the Planck analysis (Planck Collaboration, 2011) where the SZE signal is measured in the direction of  $\sim 1600$  clusters from the MCXC (Meta-Catalogue of X-ray detected Clusters of galaxies, Piffaretti et al., 2011) catalog. Because this was an X-ray based analysis we expect that these results should be most comparable to our spherical  $Y$  scaling relation results. The parameters  $B$  and  $C$  were fixed in the analysis to values that are inconsistent with the behavior we see, but the normalization is in agreement at the  $1\sigma$  level. Comparison to future large observed cluster samples where mass and redshift trends are left free will be very interesting.

#### 4.5.2 Cylindrical $Y_{\text{cyl}} - M_{500c}$ Relation

We investigate the projected SZE signature by studying the  $Y_{\text{cyl}} - M_{500c}$  relation that captures the effects of surrounding structures within a redshift slice that are projected onto the cluster. We take the clusters present in all simulation light cones and compute

their projected  $Y_{\text{cyl}}$  within the simulated redshift slice where the cluster exists. There can be a bias in the cluster signal due to the surrounding structure within which the clusters are embedded as well as other clusters within the slice. To focus on the cluster associated signal, we choose only those clusters for which there is no other cluster along the line of sight and where the whole  $5R_{500c}$  region of the cluster is contained within the redshift slice.

The result is presented in Table 4.4 along with the result from the  $Y_{\text{sph}}$  signal from the same cluster sample. Also note that, the fitting result of  $Y_{\text{sph}}$  in Table 4.3 is different from Table 4.4, which is because the cluster selections are different. In the first case, we select all the clusters present in the whole simulation box at all redshifts, whereas in the second case we just select the clusters present in the light cone. In low redshift slices, there are fewer clusters in light cones due to the limited field of view, so the redshift distributions of the two cluster samples are slightly different.

The main difference between the scaling parameters from the spherical ( $Y_{\text{sph}}$ ) and cylindrical ( $Y_{\text{cyl}}$ ) signals is in the normalization. The larger signal from the cylindrical volume as compared to the spherical volume is simply evidence that the cluster SZE signature extends well outside  $R_{500c}$ . The mean ratio between the two measurements is  $Y_{\text{cyl}}/Y_{\text{sph}} = 1.151$ . In addition, the scatter is approximately 10 percent larger in the cylinder case, reflecting the additional variations introduced by the variations in the nearby structure projected onto the cluster  $R_{500}$  region. Finally, the redshift evolution is less steep, suggesting that there are redshift dependent changes in the contributions to the cluster SZE signal from the surrounding structures.

### 4.5.3 Light Cone $Y_{\text{lc}} - M_{500c}$ Relation

We also explore the scaling relation between the SZE signal extracted from light cones  $Y_{\text{lc}}$  and mass. For this investigation, we take all the clusters that are completely inside the light cone boundaries. Thus, we have contributions to the SZE signal from clusters which overlap with each other along the line of sight. Table 4.4 shows the scaling relation fits derived from the  $Y_{\text{lc}}$  measurements, and Fig. 4.6 contains a plot of the relation with the redshift trend projected out. The  $Y_{\text{lc}}$  scaling relation deviates significantly from self-similar evolution, preferring weaker trends with mass and redshift than those we see with the spherical or cylindrical SZE observables. In addition, in comparison to the cylindrical case, the normalization is 11 percent higher, and the scatter is a factor of 1.5 higher at 0.159. In Fig. 4.6, the black data points are the clusters from all lightcones and the red solid line is the best fit model. There is a clear indication that the scatter is larger at the low mass end, behavior which was not apparent in the scaling relations involving  $Y_{\text{sph}}$  and  $Y_{\text{cyl}}$ . This suggests that the unassociated large scale structures along the line of sight are introducing a mass dependent scatter, a subject that we return to in the next section.

Because  $Y_{\text{lc}}$  is impacted by the superposition of physically uncorrelated structure along the line of sight, one can estimate the difference between  $Y_{\text{lc}}$  and  $Y_{\text{cyl}}$  using the mean  $y$  from the simulation light cone (see also Kay et al., 2012). We find this mean value to be  $\langle y_{\text{iss}} \rangle = 1.02 \times 10^{-6} \text{ sr}^{-1}$  when averaged over four lightcones. Following this logic, we

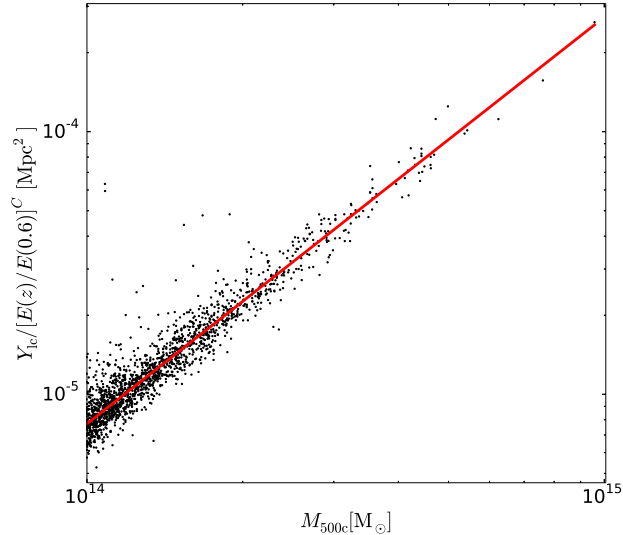


Figure 4.6: The scaling between  $Y_{lc}$  and  $M_{500c}$  where the black points represent clusters from all lightcones and the red solid line shows the best fit model. The scatter is clearly larger at the low mass end, whereas for  $Y_{sph}$  and  $Y_{cyl}$  we find no clear mass trends. This suggests that the mass dependent scatter is caused by the varying contribution of large scale structure to the total SZE signal from a cluster, introducing a mass trend that scales as  $\sigma_{\ln Y} \propto M_{500c}^{-0.38 \pm 0.05}$  (see section 4.5.4).

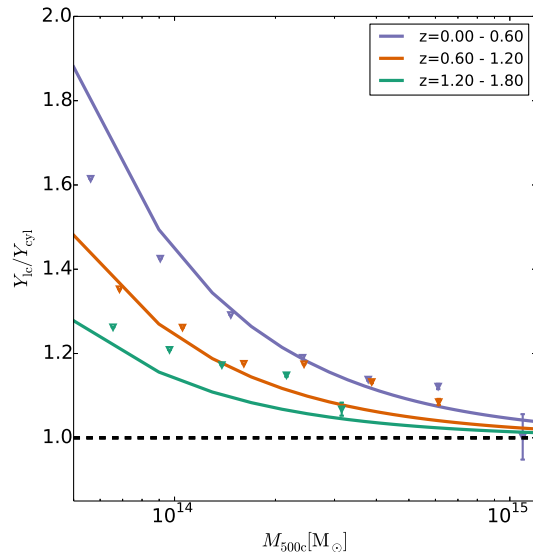


Figure 4.7: The ratio of the SZE signal extracted from light cones to that from cylinders within redshift shells is plotted versus mass for three different redshift bins. The points are the mean measurements from the simulated light cone, and the lines mark the expected impact from the SZE signal of uncorrelated structures along the line of sight, as described in equation (4.9). Points and lines are color coded by redshift. The bias decreases with increasing cluster mass and redshift.

express the estimate for the light cone SZE signal  $\langle Y_{\text{lc}} \rangle$  to be

$$\langle Y_{\text{lc}} \rangle = Y_{\text{cyl}} + \langle y_{\text{iss}} \rangle \pi R_{500c}^2, \quad (4.9)$$

where  $R_{500c}$  is the radius of the cluster, which naturally is a function of the cluster mass and redshift. Fig. 4.7 shows the ratio of the light cone to the cylindrical SZE signal  $Y_{\text{lc}}/Y_{\text{cyl}}$  as a function of cluster mass in three redshift ranges. Both direct measurements from simulation (points) and our simple model (line) are shown. It is clear that the impact of the background and foreground  $y$  due to projected structures is much larger on the low mass clusters. Moreover, one can see that at a fixed mass the impact is higher at lower redshift.

This behavior follows directly from equation (4.9), where it is the virial extent of clusters that determines how large a region of contaminating background is combined with the cluster SZE signal. This virial area scales as  $M_{500c}^{2/3}$ , while the cylindrical signal  $Y_{\text{cyl}}$  scales as  $M_{500c}^{5/3}$ , so the biasing contribution from the background and foreground structures scales as  $M_{500c}^{-1}$ , becoming less important for more massive clusters. Similarly, at fixed mass clusters have higher cylindrical SZE signal at higher redshift, scaling as  $E^{2/3}(z)$ , and smaller virial area at high redshift scaling as  $E^{-4/3}(z)$ , due to the higher density of the Universe; therefore, the contamination due to the mean  $\langle y_{\text{iss}} \rangle$  as a fraction of the cluster signal scales as  $E^{-2}(z)$ . The observed behavior in the simulations, demonstrated in Fig. 4.7, agrees qualitatively with this expectation.

As a consistency check, we test whether  $\langle y_{\text{iss}} \rangle$  measured from the light cones is consistent with the sum of the SZE signals from the population of halos along the line of sight. Specifically, we express the mean  $y$  due to large scale structure as

$$\langle y_{\text{iss}} \rangle = \iint Y_{\text{cyl}}(M, z) D_{\Lambda}(z)^{-2} \frac{dn}{dM} \frac{dV}{dzd\Omega} \Delta dM dz, \quad (4.10)$$

where  $\frac{dn}{dM}$  is the cluster mass function (Tinker et al., 2008; Eisenstein & Hu, 1998),  $V$  is the volume, and  $Y_{\text{cyl}}(M, z)$  is the SZE signal contributed by each cluster (see section 4.5.2). We integrate over redshift from 0.001 to 2 and over mass from  $10^{12}$  to  $10^{15} M_{\odot}$  in equation (4.10). The impact from extending the integral to larger redshift and lower masses is negligible for clusters with masses above  $10^{14} M_{\odot}$ . Thus, we are able to recover the measured mean SZE signal in the simulations to within 20 percent accuracy through contributions from galaxy to cluster scale halos.

The best fit parameters for the  $Y_{\text{lc}}-M_{500c}$  and the  $\langle Y_{\text{lc}} \rangle - M_{500c}$  are given in Table 4.4. The amplitude, mass and redshift trends are similar for the two relations, although there is statistical tension at the  $\sim 2\sigma$  level in the mass and redshift slopes. Note that to the extent that this bias is featureless, most CMB scanning strategies from ground based instruments would remove the bulk of this background signal. However, it is clear that departures from flatness in  $\langle y_{\text{iss}} \rangle$  contribute significantly to the cluster scatter about the SZE mass-observable relation, and therefore one might well expect that the shifts we see in the amplitude and in the redshift and mass trends will be largely mirrored in the observations.

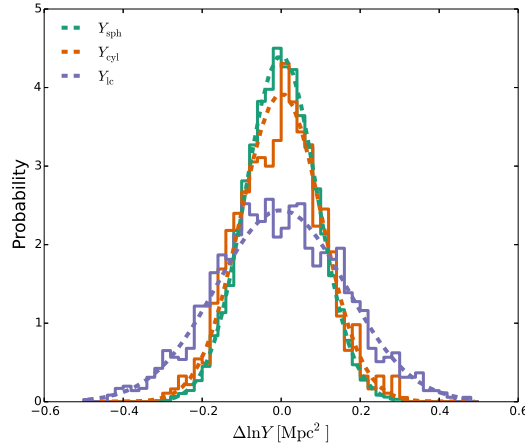


Figure 4.8: The distributions of scatter about the  $Y_{500c} - M_{500c}$  scaling relations for the spherical (green), cylindrical (red) and light cone (blue) cases. The cylindrical and light cone cases show the impacts of surrounding and physically unassociated large scale structure along the line of sight, respectively. In each case a Gaussian with the same standard deviation as the scatter distribution is shown with a dashed line. A KS test indicates that the distributions are consistent with log-normal distributions in all cases.

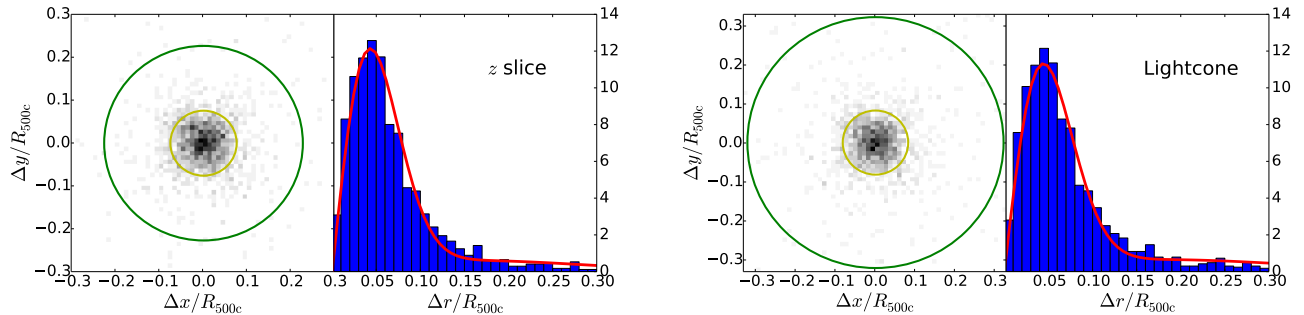


Figure 4.9: The distributions of central offsets between the gravitational center and the peak of the  $Y_{SZE}$  signal for clusters in redshift slices (top panels) and light cones (bottom panels). The yellow and green circles mark the 68<sup>th</sup> and 95<sup>th</sup> percentiles of the distribution, respectively. Radial offset distributions are also shown where the red line describes the double Rayleigh fit to these distributions. The fits indicate that about 80 percent of clusters populate the narrow first component with  $\sigma(\Delta r/R_{500c}) \sim 0.045$  and the remainder populate the wider component with  $\sigma \sim 0.16$  (see Table 4.5).

#### 4.5.4 Scatter about the $Y$ - $M$ Relations

Table 4.4 contains the log-normal constant scatter  $\sigma_{\ln Y}$  about the best fit mass–observable relations at overdensity 500c, and Fig. 4.8 shows the actual distributions of scatter. These distributions are shown as histograms color coded for the spherical SZE signal  $Y_{\text{sph}}$  (green), the cylindrical signal extracted from redshift shells  $Y_{\text{cyl}}$  (red) and the light cone signal  $Y_{\text{lc}}$  (blue). As clear from Table 4.4, the scatter increases in each of these steps. The cylindrical signal is sensitive to the asphericity of clusters and the variation in the surrounding structures in the infall regions, and the light cone includes scatter contributions from variations in the unassociated structures projected along the line of sight. A best fit log-normal distribution is plotted (dashed lines) for each of these distributions. A Kolmogorov-Smirnov (K-S) test provides no evidence that the scatter distributions are inconsistent with log-normal; the p-values are 0.83, 0.29 and 0.28 for the spherical, cylindrical and light cone cases, respectively.

As briefly mentioned in the previous section, Fig. 4.6 shows a clear trend in scatter with cluster mass. This motivates us to fit the mass dependence of the scatter to capture the impact of the uncorrelated structures along the line of sight. We fit for a scatter of the form

$$\sigma_{\ln Y}^2 = \sigma_{\ln Y_{\text{cyl}}}^2 + \sigma_{\text{A}}^2 \left[ \frac{M_{500\text{c}}}{2.84 \times 10^{14} M_{\odot}} \right]^{\sigma_{\text{B}}}, \quad (4.11)$$

along with other scaling relation parameters to all clusters in the lightcones. This form includes a floor  $\sigma_{\ln Y_{\text{cyl}}}$  to the scatter, which we measure from the  $Y_{\text{cyl}} - M_{500\text{c}}$  relation and quantifies the additional scatter in the light cones with a possible mass dependence. We find  $\sigma_{\text{A}} = 0.088 \pm 0.006$  and  $\sigma_{\text{B}} = -1.65 \pm 0.26$ , which mean that 30 percent and 66 percent of scatter is coming from uncorrelated large scale structure along the line of sight for a cluster  $M_{500\text{c}}$  of  $10^{15} M_{\odot}$  and  $10^{14} M_{\odot}$ , respectively. This provides clear evidence that low mass clusters are more affected by the mean background/foreground SZE signal. In addition to this, we also investigate trends in the scatter with redshift but find no clear evidence for that.

Interestingly, when we probe for mass dependent scatter in the  $Y_{\text{cyl}}$ -mass and  $Y_{\text{sph}}$ -mass relations, we find no evidence to support it ( $\sigma_{\text{B}}$  consistent with zero). This suggests that the cluster asphericity and variation in the surrounding structure have a similar fractional impact on the SZE observable for all masses and redshifts, but that the variation in the uncorrelated structures along the line of sight toward clusters has a more significant impact on the scatter of the SZE observable for low mass clusters than for high.

In a recent study, Le Brun et al. (2017) presented the scaling of the spherical  $Y$  signal with mass and showed a variation in the log-normal scatter by a factor of 2-3 in a mass range of  $10^{13} - 3 \times 10^{14} M_{\odot}$ . They noted that such a variation in the amplitude of the scatter with mass is caused by the inclusion of non-gravitational physics like AGN feedback. Our results here that are extracted from more massive clusters suggest a different picture. In a more recent work, Barnes et al. (2017) studied the spherical  $Y_{\text{sph}}$ -mass relation using clusters simulated with baryonic physics that yields realistic massive galaxy clusters with a comparable mass and redshift range to ours. In agreement with our findings, they find

no trend in scatter with mass and redshift.

In summary, we note that the mass dependence of the scatter that we see in the lightcone  $Y_{\text{lc}}$ -mass relation results from the fact that the SZE signal of a cluster depends sensitively on mass, while the characteristic variation of the projected SZE signal along random lines of sight does not. This leads to larger scatter for low mass clusters than for high, and we would expect this to be present also in observations. Such behavior would have implications for cosmological analyses of SZE selected cluster samples.

## 4.6 SZE Center Offsets

We study the offset between the center of the gravitational potential (most bound particle) in the clusters and the centers defined to be the peak of the SZE signal. We choose the clusters in all redshift slices and light cones with  $M_{500c} > 1.4 \times 10^{14} M_{\odot}$ . We further select clusters which have no overlap with other clusters along the line-of-sight and the clusters for which the whole  $R_{500c}$  region is contained within the respective redshift slice or light cone to avoid boundary effects in the signal.

We calculate the projected offset between the SZE center and the gravitational center in the  $x$  and  $y$  directions and normalize them by the cluster  $R_{500c}$ . Fig. 4.9 contains a plot of the scaled offsets measured using the redshift slices (left) and the light cone (right). Over the full sample of clusters we find the 68<sup>th</sup> and the 95<sup>th</sup> percentiles for the offset distributions, and these are shown in yellow and green circles, respectively. We also show the radial offset distributions  $\Delta r/R_{500c}$  (blue histograms in Fig. 4.9). The 68<sup>th</sup> percentile value for  $\Delta r/R_{500c}$  is 0.075 and 0.081 in the redshift slices and the light cone, respectively.

Following Saro et al. (2015), we model the 1-D offset distributions by fitting a double Rayleigh function of the form

$$P(x) = 2\pi x \left( \frac{\rho_0}{2\pi\sigma_0^2} e^{-\frac{x^2}{2\sigma_0^2}} + \frac{1-\rho_0}{2\pi\sigma_1^2} e^{-\frac{x^2}{2\sigma_1^2}} \right), \quad (4.12)$$

where  $x = \Delta r/R_{500c}$ ,  $\rho_0$  is the fraction of distribution in the first component, and  $\sigma_0$  and  $\sigma_1$  are the widths of the two components, respectively. The first component indicates the relatively relaxed cluster population with small offsets, whereas the second component with larger offsets represents those systems that have undergone mergers recently. To reduce the degeneracy between  $\sigma_0$  and  $\sigma_1$ , we define  $\sigma_1 = \Delta\sigma + \sigma_0$  and adopt  $\Delta\sigma$  as the free parameter in the fit. The best fit parameters and associated uncertainties are presented in Table 4.5 along with results from Saro et al. (2015). The reasonably good agreement between our results and the observational results suggests that the observed optical-SZE offset may well reflect the expected offsets between the SZE signal and cluster center due to the ongoing growth and evolution of clusters. In Fig. 4.9 we show these offsets as 1-D histograms for clusters in redshift slices as well as in light cones. The red curves over the 1-D histograms are the best fit models.

In a recent simulation study, Cui et al. (2016) showed that the BCG position correlates more strongly with the center of the gravitational potential than does the X-ray defined

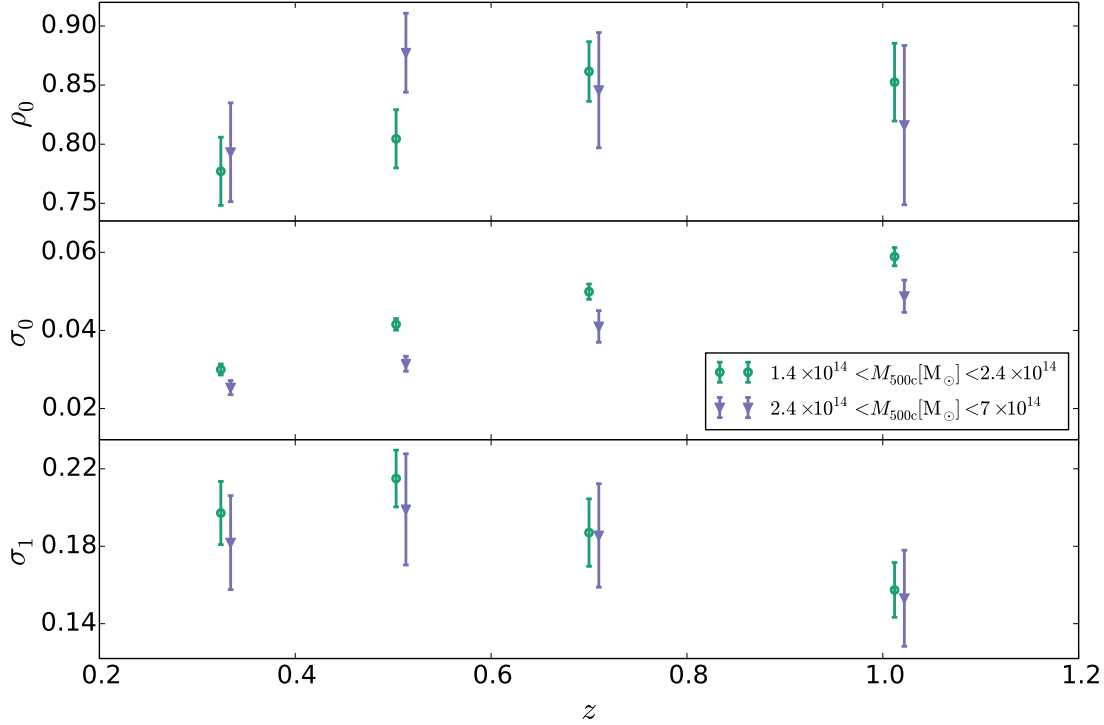


Figure 4.10: The best fit parameters of the double Rayleigh function in equation (4.12) that model the radial offset distribution of the light cones for different cluster subsamples. While the fraction of large offset or disturbed clusters remains at  $\sim 20$  percent for all subsamples and the characteristic offset of this sample is  $\sim 0.18R_{500c}$ , the characteristic offset for the more relaxed subset is larger for lower mass systems and grows with redshift.

center. In addition, the X-ray offset is enhanced by AGN feedback. Interestingly, the X-ray offsets presented in that study are comparable to those we find here for the SZE.

Next we examine the variation in the offset distributions with redshift and mass by dividing the sample into two mass and four redshift bins. We fit the double Rayleigh function (equation 4.12) to clusters in light cones for each of these bins. The best fit parameters and uncertainties are presented in Fig. 4.10. The fraction of clusters ( $\rho_0$ ) in the small offset population is always consistent with the best fit value in Table 4.5 for the full sample, suggesting that the fraction of merging or disturbed clusters remains at  $1 - \rho_0 \sim 20$  percent, independent of the mass and redshift ranges of the sample. Indeed, this large offset fraction is consistent with the large offset distributions seen between BCG and X-ray/SZE centers in samples of nearby X-ray selected clusters and SZE selected samples spanning a broad range of redshift (Lin & Mohr, 2004; Song et al., 2012).

The characteristic offset for the disturbed population in units of  $R_{500c}$  is also consistent with the best fit value from all clusters indicating that the impact of the merging clusters on the offset distribution is similar for all mass and redshift bins. In a recent study of

Table 4.5: The best fit parameters of the double Rayleigh function (see equation 4.12) fit to the radial offset distribution between the gravitational potential center and the  $Y_{\text{SZE}}$  peak for clusters in the redshift slices and in the light cones. In the last column we compare these numbers from an observational study by Saro et al. (2015).

Parameter	$z$ -slice	Light cone	Saro15
$\rho_0$	$0.838 \pm 0.013$	$0.802 \pm 0.013$	$0.63^{+0.15}_{-0.25}$
$\sigma_0$	$0.043 \pm 0.001$	$0.044 \pm 0.001$	$0.07^{+0.03}_{-0.02}$
$\sigma_1$	$0.163 \pm 0.006$	$0.184 \pm 0.006$	$0.25^{+0.07}_{-0.06}$

the X-ray morphology of samples of X-ray and SZE-selected clusters from ROSAT and SPT (Nurgaliev et al., 2016), no statistically significant redshift evolution in the X-ray morphology, over the range  $0.3 < z < 1$  was found. This is largely consistent with our result; however, the width of the relaxed population ( $\sigma_0$ ) shows clear trends with mass and redshift. The width is larger for low mass and more distant systems. This motivates us to include mass and redshift dependence in this parameter. We discuss a more sophisticated model in appendix 4.9.

Finally, we also explore a possible correlation between the mean bias in pressure evaluated assuming HSE ( $\langle P_{\text{th}}/P_{\text{eff}} \rangle$  within cluster  $R_{500c}$  and/or up to  $3R_{500c}$ ) and central offsets for clusters in lightcones. We find these quantities to be un-correlated (with a typical correlation coefficient  $\sim 0.08$ ) independent of the redshift of clusters.

## 4.7 Conclusions

For the past few years observations of large scale structure at millimeter wavelengths have been exploited and a large sample of galaxy clusters out to high redshifts has been selected using the SZE. The counts of clusters as a function of mass and redshift provide a wealth of information about the evolution of the universe. The current cluster cosmology is, however, reliant on the calibration of mass–observable scaling relations, which enables accurate modeling of the selection and comparison to the expected mass function for each cosmology.

In this study we analyze the  $Y$ -mass scaling relation using the *Magneticum* Pathfinder hydrodynamical simulations (see section 4.3.1). These simulations allow us to predict SZE signals from galaxy clusters and study the large scale structure projection effects for a large set of simulated clusters.

We study the thermal gas pressure profiles for high mass clusters out to high redshift using a generalized-NFW model and allowing for departures from self-similar trends in the pressure normalization  $P_{500}$  (see section 4.4.1). Never before such a large parameter space has been explored in studies of the cluster pressure profile. We compare our best fit pressure profile and the measured variance among profiles as a function of radius to observed profiles and find reasonable agreement. We study the variation in the shape of the pressure profile with cluster mass and redshift, finding large variations, with the most

significant differences in the inner and outer parts of the cluster. Thus, our analysis of these simulated clusters demonstrates that a universal pressure profile is not expected. We present an extended version of the GNF<sub>W</sub> model that includes the trends with mass and redshift that we find (see appendix 4.8).

We explore the deviation from self-similar trends with mass and redshift of the pressure normalization  $P_{500}$ , finding deviations from self-similarity that are statistically highly significant but nonetheless quite modest. The mass dependence of the pressure normalization is inconsistent with the self-similar value at  $\sim 2$  percent and the redshift trend at  $\sim 5$  percent.

We study the effective cluster pressure deduced from the true cluster mass obtained from the simulations using the HSE approximation (see section 4.4.2). The effective pressure is larger than the thermal gas pressure due to the presence of non-thermal pressure in clusters. We find  $\sim 20$  percent bias between HSE derived effective pressure and the thermal gas pressure around  $R_{500c}$ . This implies a bias in the X-ray derived hydrostatic masses of galaxy clusters at the same level, and provides additional evidence that hydrostatic masses are not adequate for cluster cosmological studies unless this bias can be properly accounted for.

The  $Y_{\text{SZE}}$ -mass relation is analyzed for different mass overdensity definitions. The cluster  $Y$  is extracted from the virial sphere  $Y_{\text{sph}}$ , from a cylinder within narrow redshift shells  $Y_{\text{cyl}}$  and from a full light cone  $Y_{\text{lc}}$  (see section 4.5). We find the  $Y_{\text{sph}}$  scaling relation with overdensity 500c to have the least scatter ( $\sigma_{\ln Y} \simeq 0.087$ , see Table 4.3), to exhibit mass trends consistent with self-similarity but redshift trends weaker than the self-similar expectation. We analyze the impact of projection effects on the scaling relation using  $Y_{\text{lc}}$  from the light cones, seeing a mass and redshift dependent increase in the cluster SZE signal and a mass dependent scatter going as  $\sigma_{\ln Y} \propto M_{500c}^{-0.38 \pm 0.05}$ . The SZE signal from uncorrelated structures along the line of sight can be explained through the contributions of SZE signal from halos with masses between  $10^{12}$  and  $10^{15} M_{\odot}$ . The  $Y_{\text{lc}}$ -mass relation is decidedly non-self-similar in its redshift and mass trends (see Table 4.4). The scatter distributions about the best fit relations are log-normal.

Finally, we analyze the central offset between the  $Y_{\text{SZE}}$  signal peak and the center of the gravitational potential, modeling it as a double Rayleigh distribution (see section 4.6). We find  $\sim 20$  percent of the population in the broader offset distribution, which is an indication of recent merging, while the rest exhibit small characteristic offsets of  $\sim 0.04 R_{500c}$ . A study of trends in the Rayleigh distribution with mass and redshift shows that the relaxed population remains at  $\sim 80$  percent while exhibiting an increase in its characteristic offsets with decreasing mass and increasing redshift. We present a revised offset model that includes the trends with cluster mass and redshift (see appendix 4.9).

## Acknowledgements

We thank Eiichiro Komatsu, Daisuke Nagai and David Rapetti for suggestions that improved the analysis and discussion. We also thank I-Non Chiu, Adam Mantz, Raffaella

Capasso, Corvin Stern, Sebastian Bocquet and Alfredo Zentano for their help in improving the final manuscript. We acknowledge the support by the Faculty Fellowship program at the Max Planck Institute for Extraterrestrial Physics, the International Max Planck School for Astrophysics, the DFG Cluster of Excellence “Origin and Structure of the Universe”, the Transregio program TR33 “The Dark Universe” and the Ludwig-Maximilians-Universität. The data processing has been carried out on the computing facilities of the Computational Center for Particle and Astrophysics (C2PAP), located at the Leibniz Supercomputer Center (LRZ). The *Magneticum* Pathfinder simulations have been performed at the Leibniz-Rechenzentrum with CPU time assigned to the Project pr86re.

## Appendix

### 4.8 Additional pressure profile modeling

#### Profile fitting

In section 4.4.1, we find clear trends in the shape of the pressure profile with cluster mass and redshift. The variation is most significant in the inner and outer regions of clusters. This motivates the modification of the model by including the mass and redshift dependencies to the inner and outer slopes of the GNFw profile to get an extended or e-GNFw profile written as

$$P_{\text{mod}}(r, M, z) = P_{500}(M, z) \frac{c_{500}^{\gamma'} (1 + c_{500}^{\alpha})^{(\beta' - \gamma')/\alpha}}{(c_{500} x)^{\gamma'} [1 + (c_{500} x)^{\alpha}]^{(\beta' - \gamma')/\alpha}}, \quad (4.13)$$

where  $\gamma'$  and  $\beta'$  are the modified inner and outer slopes

$$\begin{aligned} \gamma' &= \gamma_0 \left[ \frac{M_{500c}}{3 \times 10^{14} M_{\odot}} \right]^{\gamma_1} E(z)^{\gamma_2}, \\ \beta' &= \beta_0 \left[ \frac{M_{500c}}{3 \times 10^{14} M_{\odot}} \right]^{\beta_1} E(z)^{\beta_2}. \end{aligned} \quad (4.14)$$

Thus, the e-GNFw profile is parametrized with 4 more parameters as compared to the GNFw model. We fit this extended model to the pressure profile from our simulations, taking advantage of the statistical power of MPS to constrain the complex high dimensional parameter space using the same methodology as described in section 4.4.1. We verify that the intrinsic scatter deduced from the most likely extended model is consistent with the intrinsic scatter shown in Fig. 4.2. The best fit parameters along with  $1\text{-}\sigma$  uncertainties are presented in Table 4.6.

The marginalized posteriors are presented in Fig. 4.11 in the form of a triangle plot, which shows the joint confidence contours for different parameter pairs as well as the fully marginalized constraints for each single parameter. Interestingly, the additional covariances do not degrade the constraints on our model as the size of the cluster sample is very large.

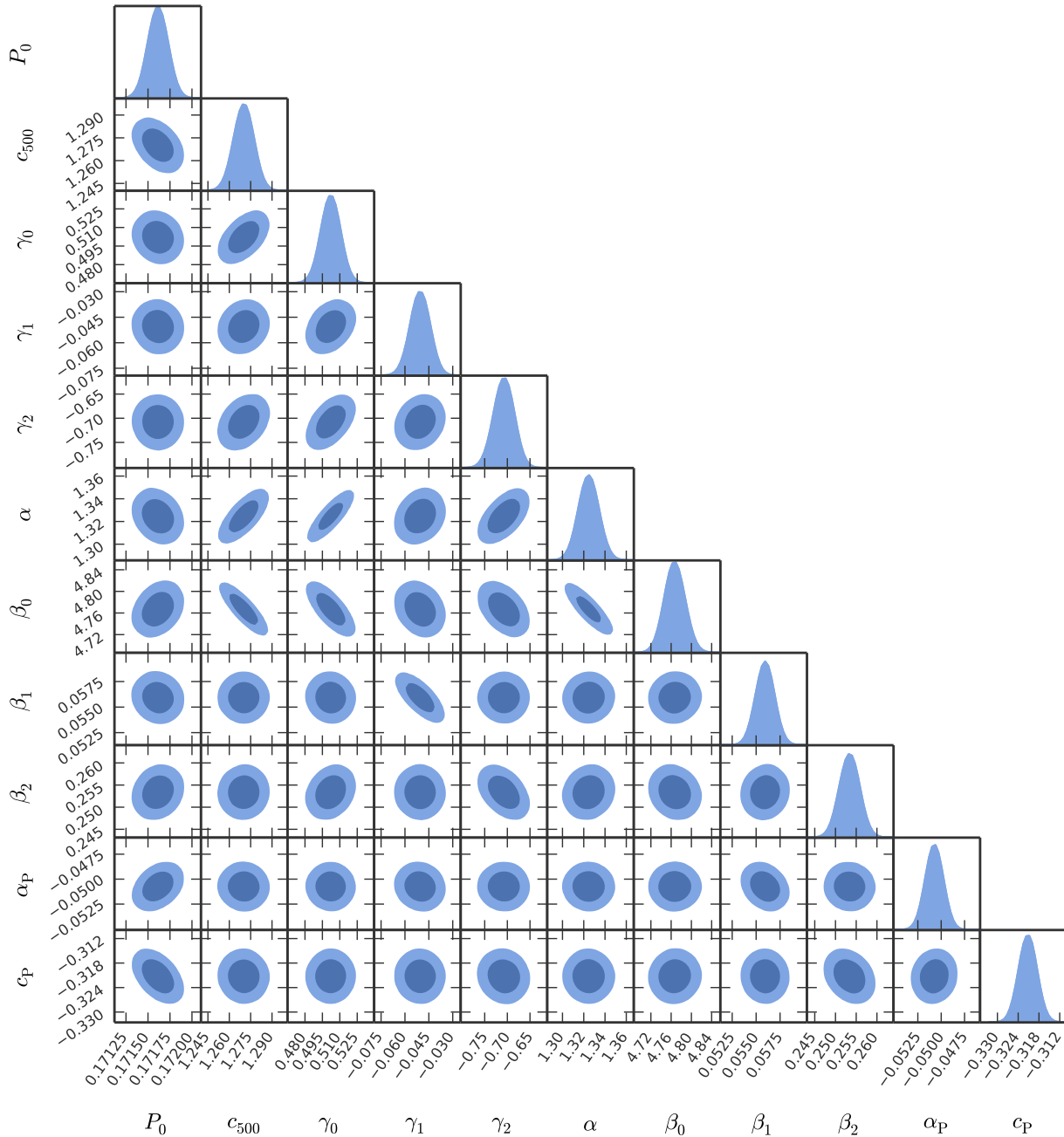


Figure 4.11: Constraints on the e-GNFW model parameters from the simulated pressure profiles in the MPS. Shading from center to outside indicate the 1 and 2  $\sigma$  joint parameter confidence intervals, and the fully marginalized constraints for each parameter are at the right end of each row (Bocquet & Carter, 2016).

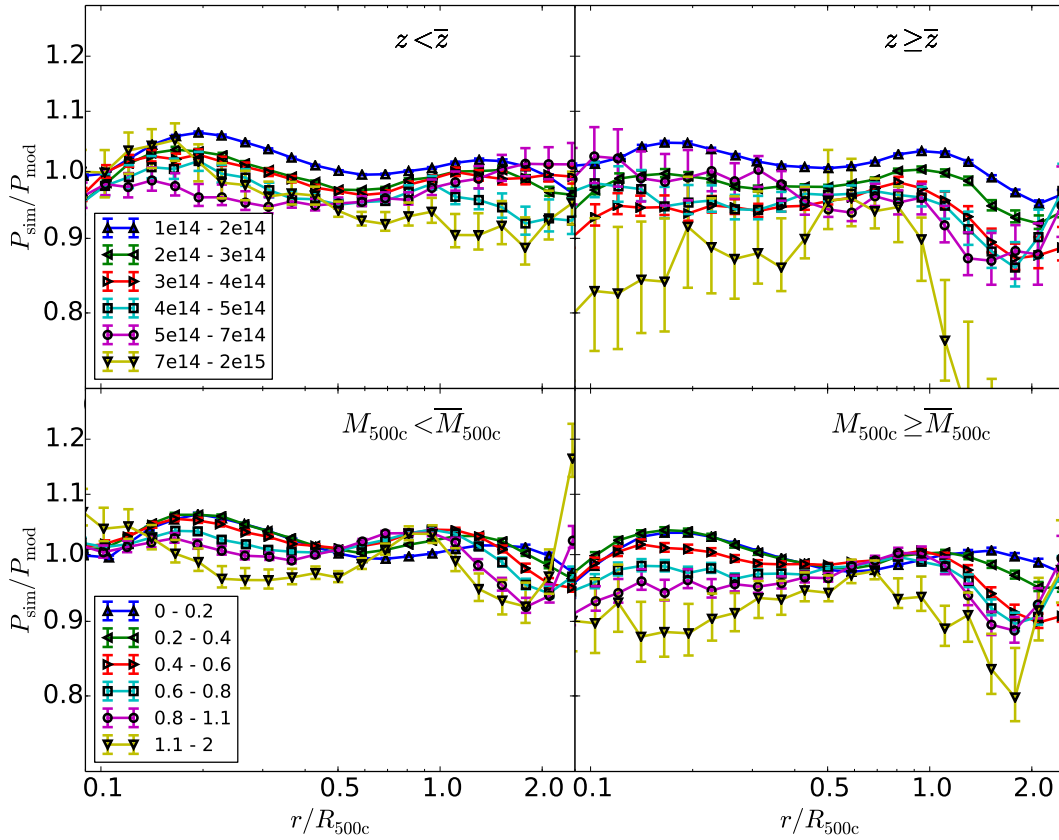


Figure 4.12: Cluster pressure comparison in bins of mass ( $M_{500c}$ , upper panels) and redshift (lower panels) with respect to the best fit e-GNFW profile (see Fig. 4.3 for further details). Clearly, the extended model is a much better fit to the whole range of clusters in the sample.

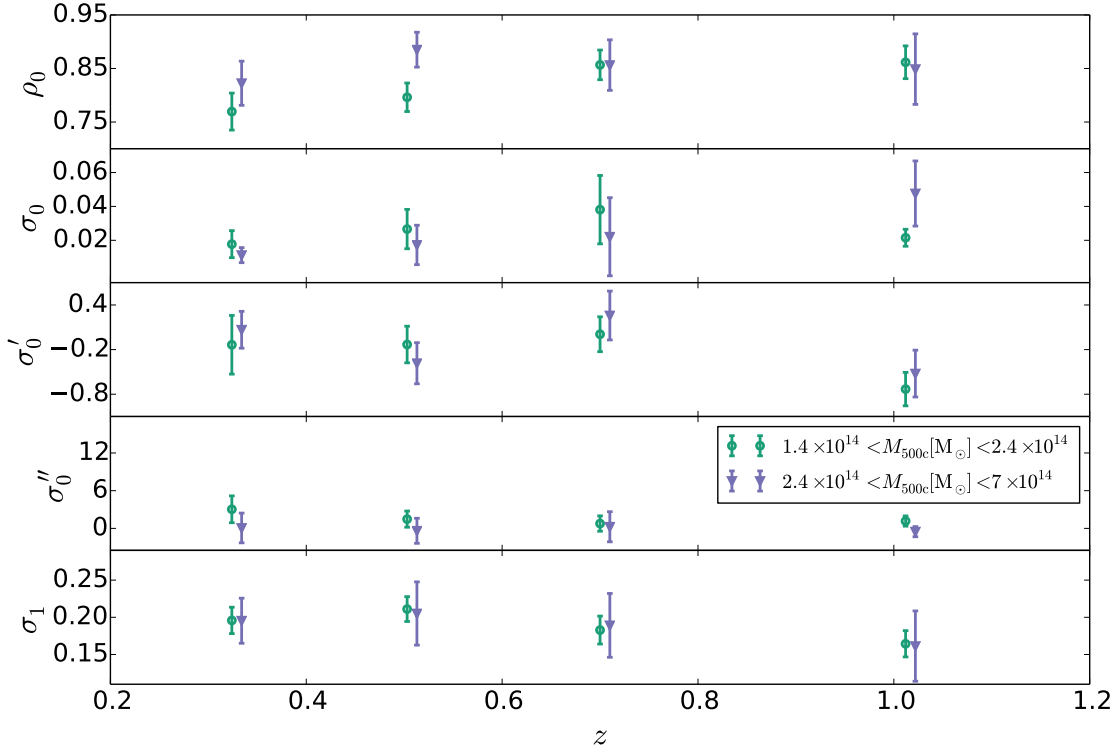


Figure 4.13: Offset trends showing the consistency of the parameters with mass and redshift.

Battaglia et al. (2012b) use a similar functional form to fit pressure profiles for a set of simulated clusters and show similar trends in  $\beta$  with mass ( $\beta_1 = 0.039$  for  $z = 0$  clusters) but find larger evolution with redshift ( $\beta_2 = 0.415$  for  $1.1 \times 10^{14} M_\odot < M_{200c} < 1.7 \times 10^{14} M_\odot$ ) as compared to our findings. In an observational work, Sayers et al. (2016) measure SZE signal toward a set of 47 clusters with a median mass of  $9.5 \times 10^{14} M_\odot$  and a median redshift of 0.4 using data from Planck and the ground-based Bolocam receiver. They find  $\beta_1 = 0.077 \pm 0.026$ , which is consistent with our results. However, they find no evolution in  $\beta$  with redshift, which as they imply, could be a result of sample selection, as their sample is biased toward relaxed cool-core systems at low- $z$  and toward disturbed merging systems at high- $z$ . We caution the reader while interpreting these results as different set of parameters are varied in these studies.

## Variations in extended profile shape with mass and redshift

Next we re-examine the systematic shape variations in pressure profiles with cluster mass and redshift and with respect to the e-GNFW model presented here. The clusters are selected from the full simulation box in the same manner as described in section 4.4.1. The ratios between the pressure and the best fit e-GNFW model are shown in Fig. 4.12 for

Table 4.6: Constraints on the e-GNFW model parameters from fits to the simulated pressure profiles. These results are from clusters in the full simulation box with  $\langle M_{500c} \rangle = 2.3 \times 10^{14} M_{\odot}$  and  $\langle z \rangle = 0.31$ .

Parameter	values
$P_0$	$0.1716 \pm 0.0001$
$c_{500}$	$1.270 \pm 0.006$
$\gamma_0$	$0.502 \pm 0.008$
$\gamma_1$	$-0.050 \pm 0.005$
$\gamma_2$	$-0.71 \pm 0.02$
$\alpha$	$1.33 \pm 0.01$
$\beta_0$	$4.77 \pm 0.02$
$\beta_1$	$0.056 \pm 0.001$
$\beta_2$	$0.254 \pm 0.002$
$\alpha_P$	$-0.051 \pm 0.001$
$c_P$	$-0.321 \pm 0.002$

Table 4.7: The best fit parameters of the extended double Rayleigh function (see equation (4.15)) fit to the radial offset distribution between the gravitational potential center and the  $Y_{\text{SZE}}$  peak for clusters in the in the light cones for a revised model.

Parameter	Light cone
$\rho_0$	$0.769 \pm 0.035$
$\sigma_0$	$0.018 \pm 0.008$
$\sigma'_0$	$-0.14 \pm 0.39$
$\sigma''_0$	$3.037 \pm 2.137$
$\sigma_1$	$0.195 \pm 0.017$

different sub-samples. For cluster sub-sample with  $z < \bar{z}$  (upper left panel), the model is within 5 percent of the simulations for the whole radial range and different mass bins. The sample with  $z < \bar{z}$  is also consistent with best fit model within 10 percent (upper right panel), except for the last mass bin ( $7 \times 10^{14} < M_{500c} < 2 \times 10^{15}$ ), which is because of very small number of clusters (25 clusters) in this range that has a small weight in the best fit model. Similarly, the model is consistent with clusters in different redshift bins, except for the last redshift bin ( $1.1 < z < 2$ ) in the lower right panel.

## 4.9 Additional offset modeling

In section 4.6, we described the variation in the offset distributions with mass and redshift and concluded that the relaxed cluster population show trends in the width of the Rayleigh distribution both with mass and redshift. In order to contain this evolution within the model, we extend the Rayleigh function by including mass and redshift dependencies to

the width of the first component of the distribution as

$$P(x) = 2\pi x \left( \frac{\rho_0}{2\pi\sigma_R^2} e^{-\frac{x^2}{2\sigma_R^2}} + \frac{1-\rho_0}{2\pi\sigma_1^2} e^{-\frac{x^2}{2\sigma_1^2}} \right), \quad (4.15)$$

where  $\sigma_R$  is the extended width written as

$$\sigma_R = \sigma_0 \left[ \frac{M_{500c}}{3 \times 10^{14} M_\odot} \right]^{\sigma'_0} E(z)^{\sigma''_0}. \quad (4.16)$$

The best fit model parameters and  $1-\sigma$  uncertainties are presented in Table 4.7 for all clusters in the light cone.

Next, we study the variation in the revised model parameters in the same range of cluster masses and redshifts as examined in section 4.6. The best fit parameters and uncertainties are shown in Fig. 4.13, which clearly indicates that the trends in the width of the relaxed population is captured within the framework of this extended model.



# Conclusions

This thesis work is based on the studies of statistical and structural properties of the Universe in the framework of both large scale structure observations and large hydrodynamical simulations. In this chapter, I will summarize the scientific results presented in this thesis and discuss some interesting aspects for future analyses.

In chapter 2, we present a study of cluster radio galaxies observed at high frequencies. We use radio sources selected from the SUMSS catalog at 843 MHz and measure the fluxes of these sources in SPT-SZ maps at 95, 150 and 220 GHz to study the overdensity of radio galaxies associated with the X-ray selected galaxy clusters from MCXC catalog. We examine SPT maps at the locations of the SUMSS sources, extracting the high frequency fluxes and correcting for the cluster SZE flux at 95 and 150 GHz. The SZE flux biases are significant for high redshift and for higher mass clusters that have stronger SZE signatures. The MCXC systems in the SPT-SZ and SUMSS regions have a median redshift  $z \sim 0.1$ , and the highest redshift system is at  $z = 0.686$ . There are 139 and 333 MCXC objects in the SPT-SZ and the SUMSS regions, respectively, spanning the mass range from groups to clusters with a median mass  $M_{500c} = 1.5 \times 10^{14} M_{\odot}$  and  $1.7 \times 10^{14} M_{\odot}$  in SPT-SZ and SUMSS regions, respectively. We construct radial profiles and luminosity functions (LFs) for these cluster radio galaxies. We find that the radial profile is centrally concentrated, consistent with an NFW model with concentration  $c = 108_{-48}^{+107}$ . We construct the LFs assuming the overdensity of radio galaxies towards a cluster is at the redshift of the cluster. The amplitude of the 843 MHz LF is approximately one order of magnitude higher than the amplitude of the high frequency LFs. We use the measured high frequency cluster radio galaxy LFs to examine the effect of the contaminating flux on the SZE signatures of galaxy clusters. We estimate the impact of cluster radio galaxies on the cluster sample from the SPT-SZ 2500 deg<sup>2</sup> survey at 150 GHz, using the theoretically predicted mass function to produce 100 mock cluster samples. We then compare the  $\xi > 4.5$  cluster samples with and without cluster radio galaxies. We find that around  $1.8 \pm 0.7$  percent of clusters would be lost from the sample in a redshift range of 0.25 to 1.55 in the 2500 deg<sup>2</sup> SPT-SZ survey. We note that with the MCXC sample, we cannot place strong constraints on the redshift evolution of the high frequency radio galaxy LF. A larger sample of non-SZE selected clusters with accurate mass estimates and spanning a larger redshift range is needed to resolve the issues of redshift evolution of the radio galaxy LF and to improve the constraints on the LFs at 150 and 95 GHz.

In chapter 3, we present an extension of the analysis from chapter 2 using a sample

of galaxy clusters that extends to high redshift. We use the redMaPPer catalog from the Dark Energy Survey first year observations and look for the excess of the sources in the direction of these clusters. The median redshift of these clusters is 0.46 with the highest redshift system at  $z \sim 0.77$ . The mass of these clusters is estimated using a richness-mass relation with median mass  $M_{200c} = 1.8 \times 10^{14} M_{\odot}$ . We find that the radial distribution of the radio AGN within the cluster sample is highly concentrated with NFW concentration  $c \sim 170, 600$  and  $450$  at  $0.843, 95$  and  $150$  GHz, respectively. We construct the LFs using a similar approach to that described in chapter 2 and extend the model to constrain the redshift trends in cluster radio galaxies. The pure luminosity  $(1+z)^{\gamma_P}$  and density  $(1+z)^{\gamma_D}$  evolution parameters at  $0.843$  GHz are  $\gamma_P = 2.21 \pm 0.46$  and  $\gamma_D = 2.32 \pm 0.41$ , respectively. At higher frequencies we find consistent but larger evolution with  $\gamma_D = 6.7 \pm 3.5$  and  $\gamma_D = 6.3 \pm 2.8$  for  $95$  and  $150$  GHz samples, respectively. We find that around  $10.7 \pm 2.4$  percent of clusters would be lost from the sample in a redshift range of  $0.25$  to  $1.55$  in a  $2500 \text{ deg}^2$  SPT-SZ like survey. We find the bias in the parameters of the observable  $\zeta$ -mass relation due to radio galaxy contamination to not be important to for our cosmological analysis, given the posterior constraints on these parameters as presented in de Haan et al. (2016). The impact of the incompleteness in the cluster sample is expected to introduce shifts comparable to the statistical uncertainties in our present cluster sample, given that the Poisson noise on the full sample is at the 5 percent level. Quantification of these impacts awaits results from ongoing analyses.

In chapter 4, we analyze a large sample of galaxy clusters using the *Magneticum* Pathfinder hydrodynamical simulations. These simulations allow us to predict SZE signals from galaxy clusters and study the large scale structure projection effects for a large set of simulated clusters. We present the thermal gas pressure profiles for high mass clusters out to high redshift using a generalized-NFW (GNFW) model. We find reasonable agreement between the observed and simulated pressure profiles. We study the variation in the shape of the pressure profile with cluster mass and redshift and demonstrate that a universal pressure profile is not expected. We present an extended version of the GNFW model that includes the trends with mass and redshift. We study the effective cluster pressure deduced from the true cluster mass obtained from the simulations using the Hydrostatic equilibrium (HSE) approximation (see section 3.2). The effective pressure is larger than the thermal gas pressure due to the presence of non-thermal pressure in clusters. We find  $\sim 20$  percent bias between HSE derived effective pressure and the thermal gas pressure around  $R_{500c}$ . This implies a bias in the X-ray derived hydrostatic masses of galaxy clusters at the same level, and provides additional evidence that hydrostatic masses are not adequate for cluster cosmological studies unless this bias can be properly accounted for. Further, we analyze the  $Y_{\text{SZE}}$ -mass relation for different mass overdensity definitions finding least scatter ( $\sigma_{\ln Y} \simeq 0.087$ ) for scaling relation with overdensity  $500c$ . We study SZE scaling relations with  $Y$  extracted from the virial sphere  $Y_{\text{sph}}$ , from a cylinder within narrow redshift shells  $Y_{\text{cyl}}$  and from a full light cone  $Y_{\text{lc}}$ . We analyze the impact of projection effects on the scaling relation using  $Y_{\text{lc}}$  from the light cones, seeing a mass and redshift dependent increase in the cluster SZE signal and a mass dependent scatter going as  $\sigma_{\ln Y} \propto M_{500c}^{-0.38 \pm 0.05}$ . We analyze the central offset between the  $Y_{\text{SZE}}$  signal peak and the

---

center of the gravitational potential. We find  $\sim 20$  percent of the population in the broader offset distribution, which is an indication of recent merging. A study of trends with mass and redshift shows that the relaxed population remains at  $\sim 80$  percent while exhibiting an increase in its characteristic offsets with decreasing mass and increasing redshift. We present a revised offset model that includes the trends with cluster mass and redshift.

The motivation behind this thesis work is to study the systematics in cluster selection and cluster mass estimation for SZE detected galaxy cluster samples. As mentioned in the last section of chapter 1, for SPT and Planck SZE selected cluster samples there is a preference for higher cluster masses when these masses are calibrated in conjunction with external cosmological constraints (e.g. Planck Collaboration et al., 2015b) in comparison to direct calibration using weak lensing, velocity dispersions, CMB lensing or X-ray hydrostatic masses see Fig. 7 in chapter 1 (also see fig. 2 in Bocquet et al., 2015).

Given the results of our high frequency cluster radio galaxy study, the incompleteness in the cluster sample is significant and this can affect our cluster cosmology. We find that the incompleteness increases with redshift as the the mean number density of cluster radio galaxies is larger at higher redshifts. Also, the contamination due to these radio sources is larger for low mass clusters. Thus, inevitably for future and ongoing surveys where more low mass and high redshift systems are expected, a suitable correction for this incompleteness will be important. In our future work, we plan to estimate the impact of radio contamination on cluster cosmology using mock cluster samples resembling the catalogs from surveys like SPT-SZ, SPTpol, SPT-3G and CMB-S4.

The upcoming eROSITA X-ray survey (Merloni et al., 2012; Predehl et al., 2014) is expected to observe a large number of clusters up to redshifts  $z \sim 1$ . Also, upcoming large radio surveys such as MeerKLASS (MeerKAT Large Area Synoptic Survey; Santos et al., 2017) will produce a large continuum galaxy sample down to a depth of about  $5 \mu\text{Jy}$  in  $4000 \text{ deg}^2$  of southern sky, which is quite unique over such large areas and will allow studies of the large-scale structure of the Universe out to high redshifts. We are looking forward to examining this population of galaxies in the eROSITA X-ray detected galaxy clusters. This will provide us with the tightest constraints yet on the redshift trends in cluster and field radio galaxies.

## Bibliography

- Abazajian K. N., et al., 2015, *Astroparticle Physics*, 63, 66
- Aihara H., et al., 2011, *ApJS*, 193, 29
- Annis J., et al., 2014, *ApJ*, 794, 120
- Arnaud M., Pratt G. W., Piffaretti R., Böhringer H., Croston J. H., Pointecouteau E., 2010, *A&A*, 517, A92+
- Arthur J., et al., 2017, *MNRAS*, 464, 2027
- Avestruz C., Nagai D., Lau E. T., 2016, preprint, ([arXiv:1605.01723](https://arxiv.org/abs/1605.01723))
- Barnes D. J., Kay S. T., Henson M. A., McCarthy I. G., Schaye J., Jenkins A., 2017, *MNRAS*, 465, 213
- Bartelmann M., 1996, *A&A*, 313, 697
- Battaglia N., Bond J. R., Pfrommer C., Sievers J. L., Sijacki D., 2010, *ApJ*, 725, 91
- Battaglia N., Bond J. R., Pfrommer C., Sievers J. L., 2011, *ArXiv:1109.3711*,
- Battaglia N., Bond J. R., Pfrommer C., Sievers J. L., 2012a, *ApJ*, 758, 74
- Battaglia N., Bond J. R., Pfrommer C., Sievers J. L., 2012b, *ApJ*, 758, 75
- Beck A. M., et al., 2016, *MNRAS*, 455, 2110
- Becker R. H., White R. L., Helfand D. J., 1995, *ApJ*, 450, 559
- Benson B. A., et al., 2013, *ApJ*, 763, 147
- Benson B. A., et al., 2014, in *Millimeter, Submillimeter, and Far-Infrared Detectors and Instrumentation for Astronomy VII*. p. 91531P ([arXiv:1407.2973](https://arxiv.org/abs/1407.2973)), doi:10.1117/12.2057305
- Best P. N., Heckman T. M., 2012, *MNRAS*, 421, 1569
- Biesiadzinski T., McMahon J. J., Miller C. J., Nord B., Shaw L., 2012, preprint, ([arXiv:1201.1282](https://arxiv.org/abs/1201.1282))
- Biffi V., Dolag K., Böhringer H., 2013, *MNRAS*, 428, 1395
- Biffi V., et al., 2016, *ApJ*, 827, 112
- Birkinshaw M., Gull S. F., Hardebeck H., 1984, *Nature*, 309, 34
- Birzan L., Rafferty D. A., Brüggén M., Intema H. T., 2017, *MNRAS*, 471, 1766

- Bleem L., et al., 2012, *Journal of Low Temperature Physics*, p. 196
- Bleem L. E., et al., 2015, *ApJS*, 216, 27
- Bock D. C.-J., Large M. I., Sadler E. M., 1999, *AJ*, 117, 1578
- Bocquet S., Carter F. W., 2016, *The Journal of Open Source Software*, 1
- Bocquet S., et al., 2015, *ApJ*, 799, 214
- Bocquet S., Saro A., Dolag K., Mohr J. J., 2016a, *MNRAS*, 456, 2361
- Bocquet S., Saro A., Dolag K., Mohr J. J., 2016b, *MNRAS*, 456, 2361
- Böhringer H., et al., 2000, *ApJS*, 129, 435
- Böhringer H., et al., 2004, *A&A*, 425, 367
- Böhringer H., et al., 2007, *A&A*, 469, 363
- Bonaldi A., Tormen G., Dolag K., Moscardini L., 2007, *MNRAS*, 378, 1248
- Borgani S., et al., 2004, *MNRAS*, 348, 1078
- Boyle B. J., Shanks T., Peterson B. A., 1988, *MNRAS*, 235, 935
- Branchesi M., Gioia I. M., Fanti C., Fanti R., Perley R., 2006, *A&A*, 446, 97
- Brown M. J. I., Webster R. L., Boyle B. J., 2001, *AJ*, 121, 2381
- Burenin R. A., Vikhlinin A., Hornstrup A., Ebeling H., Quintana H., Mescheryakov A., 2007, *ApJS*, 172, 561
- Burns J. O., Skillman S. W., O'Shea B. W., 2010, *ApJ*, 721, 1105
- Capasso et al. in prep., preprint ([arXiv:9999.9999](https://arxiv.org/abs/9999.9999))
- Carlstrom J. E., Holder G. P., Reese E. D., 2002, *ARA&A*, 40, 643
- Carlstrom J. E., et al., 2011, *PASP*, 123, 568
- Cash W., 1979, *ApJ*, 228, 939
- Chiu I.-N. T., Molnar S. M., 2012, *ApJ*, 756, 1
- Chiu I., et al., 2016, *MNRAS*, 457, 3050
- Coble K., et al., 2007, *AJ*, 134, 897
- Condon J. J., 1992, *ARA&A*, 30, 575

- Condon J. J., Cotton W. D., Greisen E. W., Yin Q. F., Perley R. A., Taylor G. B., Broderick J. J., 1998, *AJ*, 115, 1693
- Condon J. J., Cotton W. D., Broderick J. J., 2002, *AJ*, 124, 675
- Cooray A. R., Grego L., Holzzapfel W. L., Joy M., Carlstrom J. E., 1998, *AJ*, 115, 1388
- Cruddace R., et al., 2002, *ApJS*, 140, 239
- Cui W., et al., 2016, *MNRAS*, 458, 4052
- DES Collaboration 2005, preprint, ([arXiv:astro-ph/0510346](https://arxiv.org/abs/astro-ph/0510346))
- Da Silva A. C., Kay S. T., Liddle A. R., Thomas P. A., Pearce F. R., Barbosa D., 2001, *ApJ*, 561, L15
- Davis M., Efstathiou G., Frenk C. S., White S. D. M., 1985, *ApJ*, 292, 371
- De Zotti G., Massardi M., Negrello M., Wall J., 2010, *A&ARv*, 18, 1
- Dehnen W., Aly H., 2012, *MNRAS*, 425, 1068
- Dolag K., Stasyszyn F., 2009, *MNRAS*, 398, 1678
- Dolag K., Jubelgas M., Springel V., Borgani S., Rasia E., 2004, *ApJ*, 606, L97
- Dolag K., Vazza F., Brunetti G., Tormen G., 2005a, *MNRAS*, 364, 753
- Dolag K., Vazza F., Brunetti G., Tormen G., 2005b, *MNRAS*, 364, 753
- Dolag K., Borgani S., Murante G., Springel V., 2009, *MNRAS*, 399, 497
- Dolag K., Komatsu E., Sunyaev R., 2016, *MNRAS*, 463, 1797
- Dolag et al. in prep., preprint ([arXiv:9999.9999](https://arxiv.org/abs/9999.9999))
- Donnert J., Dolag K., Brunetti G., Cassano R., 2013, *MNRAS*, 429, 3564
- Dressler A., Shectman S. A., 1988, *AJ*, 95, 985
- Du W., Fan Z., 2014, *ApJ*, 785, 57
- Duffy A. R., Schaye J., Kay S. T., Dalla Vecchia C., 2008, *MNRAS*, 390, L64
- Ebeling H., Edge A. C., Bohringer H., Allen S. W., Crawford C. S., Fabian A. C., Voges W., Huchra J. P., 1998, *MNRAS*, 301, 881
- Ebeling H., Edge A. C., Allen S. W., Crawford C. S., Fabian A. C., Huchra J. P., 2000, *MNRAS*, 318, 333

- Ebeling H., Edge A. C., Henry J. P., 2001, *ApJ*, 553, 668
- Ebeling H., Mullis C. R., Tully R. B., 2002, *ApJ*, 580, 774
- Eisenstein D. J., Hu W., 1998, *ApJ*, 496, 605
- Elahi P. J., et al., 2016, *MNRAS*, 458, 1096
- Ensslin T. A., Biermann P. L., Kronberg P. P., Wu X.-P., 1997, *ApJ*, 477, 560
- Everett et al. in prep., preprint ([arXiv:9999.9999](https://arxiv.org/abs/9999.9999))
- Evrard A. E., 1990, *ApJ*, 363, 349
- Fabjan D., Tornatore L., Borgani S., Saro A., Dolag K., 2008, *MNRAS*, 386, 1265
- Fabjan D., Borgani S., Tornatore L., Saro A., Murante G., Dolag K., 2010, *MNRAS*, 401, 1670
- Fang T., Humphrey P., Buote D., 2009, *ApJ*, 691, 1648
- Fassbender R., et al., 2011, *New Journal of Physics*, 13, 125014
- Foreman-Mackey D., Hogg D. W., Lang D., Goodman J., 2013, *PASP*, 125, 306
- Fowler J. W., et al., 2007, *Appl. Opt.*, 46, 3444
- Gazzola L., Pearce F. R., 2007, in Böhringer H., Pratt G. W., Finoguenov A., Schuecker P., eds, *Heating versus Cooling in Galaxies and Clusters of Galaxies*. p. 412 ([arXiv:astro-ph/0611715](https://arxiv.org/abs/astro-ph/0611715)), doi:10.1007/978-3-540-73484-0\_76
- Geller M. J., Beers T. C., 1982, *PASP*, 94, 421
- George M. R., et al., 2012, *ApJ*, 757, 2
- Gioia I. M., Luppino G. A., 1994, *ApJS*, 94, 583
- Gladders M. D., Yee H. K. C., 2005, *ApJS*, 157, 1
- Gottloeber S., Yepes G., Wagner C., Sevilla R., 2006, *ArXiv Astrophysics e-prints*,
- Gralla M. B., Gladders M. D., Yee H. K. C., Barrientos L. F., 2011, *ApJ*, 734, 103
- Green T. S., et al., 2016, *MNRAS*, 461, 560
- Gregory P. C., Scott W. K., Douglas K., Condon J. J., 1996, *ApJS*, 103, 427
- Griffith M. R., Wright A. E., 1993, *AJ*, 105, 1666
- Gupta N., et al., 2017a, *MNRAS*, 467, 3737

- Gupta N., et al., 2017b, MNRAS, 467, 3737
- Haiman Z., Mohr J. J., Holder G. P., 2001, ApJ, 553, 545
- Hasselfield M., et al., 2013, J. Cosmology Astropart. Phys., 7, 008
- Hennig C., et al., 2016, preprint, ([arXiv:1604.00988](https://arxiv.org/abs/1604.00988))
- Henry J. P., 2004, ApJ, 609, 603
- Henry J. P., Mullis C. R., Voges W., Böhringer H., Briel U. G., Gioia I. M., Huchra J. P., 2006, ApJS, 162, 304
- Hirschmann M., Dolag K., Saro A., Bachmann L., Borgani S., Burkert A., 2014, MNRAS, 442, 2304
- Hoekstra H., Herbonnet R., Muzzin A., Babul A., Mahdavi A., Viola M., Cacciato M., 2015, MNRAS, 449, 685
- Högbom J. A., 1974, A&AS, 15, 417
- Horner D. J., Perlman E. S., Ebeling H., Jones L. R., Scharf C. A., Wegner G., Malkan M., Maughan B., 2008, ApJS, 176, 374
- Iverson R. J., et al., 2007, MNRAS, 380, 199
- Janssen R. M. J., Röttgering H. J. A., Best P. N., Brinchmann J., 2012, A&A, 541, A62
- Johnston D. E., et al., 2007, preprint, ([arXiv:0709.1159](https://arxiv.org/abs/0709.1159))
- Kaiser N., Silk J., 1986, Nature, 324, 529
- Kauffmann G., Heckman T. M., Best P. N., 2008, MNRAS, 384, 953
- Kay S. T., Thomas P. A., Jenkins A., Pearce F. R., 2004, MNRAS, 355, 1091
- Kay S. T., Peel M. W., Short C. J., Thomas P. A., Young O. E., Battye R. A., Liddle A. R., Pearce F. R., 2012, MNRAS, 422, 1999
- Kocevski D. D., Ebeling H., Mullis C. R., Tully R. B., 2007, ApJ, 662, 224
- Koester B. P., et al., 2007a, ApJ, 660, 221
- Koester B. P., et al., 2007b, ApJ, 660, 239
- Komatsu E., et al., 2011, ApJS, 192, 18
- Korngut P. M., et al., 2011, ApJ, 734, 10
- Kravtsov A. V., Nagai D., Vikhlinin A. A., 2005, ApJ, 625, 588

- Kravtsov A. V., Vikhlinin A., Nagai D., 2006, *ApJ*, 650, 128
- LSST Science Collaboration 2009, preprint, ([arXiv:0912.0201](https://arxiv.org/abs/0912.0201))
- Lau E. T., Kravtsov A. V., Nagai D., 2009, *ApJ*, 705, 1129
- Lau E. T., Nagai D., Avestruz C., Nelson K., Vikhlinin A., 2015, *ApJ*, 806, 68
- Laureijs R., et al., 2011, preprint, ([arXiv:1110.3193](https://arxiv.org/abs/1110.3193))
- Le Brun A. M. C., McCarthy I. G., Schaye J., Ponman T. J., 2014, *MNRAS*, 441, 1270
- Le Brun A. M. C., McCarthy I. G., Schaye J., Ponman T. J., 2017, *MNRAS*, 466, 4442
- Ledlow M. J., Owen F. N., 1996, *AJ*, 112, 9
- Lin Y.-T., Mohr J. J., 2004, *ApJ*, 617, 879
- Lin Y.-T., Mohr J. J., 2007, *ApJS*, 170, 71
- Lin Y., Mohr J. J., Stanford S. A., 2004, *ApJ*, 610, 745
- Lin Y., Partridge B., Pober J. C., Boucheffry K. E., Burke S., Klein J. N., Coish J. W., Huffenberger K. M., 2009, *ApJ*, 694, 992
- Lin Y.-T., Shen Y., Strauss M. A., Richards G. T., Lunnan R., 2010, *ApJ*, 723, 1119
- Lin H. W., McDonald M., Benson B., Miller E., 2015, *ApJ*, 802, 34
- Lin Y.-T., et al., 2017, preprint, ([arXiv:1709.04484](https://arxiv.org/abs/1709.04484))
- Machalski J., Godlowski W., 2000, *A&A*, 360, 463
- Majumdar S., Mohr J. J., 2003, *ApJ*, 585, 603
- Mantz A., Allen S. W., Ebeling H., Rapetti D., Drlica-Wagner A., 2010, *MNRAS*, 406, 1773
- Marriage T. A., et al., 2011, *ApJ*, 737, 61
- Massardi M., et al., 2008, *MNRAS*, 384, 775
- Mauch T., Murphy T., Buttery H. J., Curran J., Hunstead R. W., Piestrzynski B., Robertson J. G., Sadler E. M., 2003, *MNRAS*, 342, 1117
- McAlpine K., Jarvis M. J., Bonfield D. G., 2013, *MNRAS*, 436, 1084
- McCarthy I. G., Babul A., Holder G. P., Balogh M. L., 2003, *ApJ*, 591, 515
- McDonald M., et al., 2014, *ApJ*, 794, 67

- Melchior P., et al., 2017, MNRAS, 469, 4899
- Melin J.-B., Bartlett J. G., Delabrouille J., 2006, A&A, 459, 341
- Meneghetti M., Rasia E., Merten J., Bellagamba F., Ettori S., Mazzotta P., Dolag K., Marri S., 2010, A&A, 514, A93
- Merloni A., et al., 2012, preprint, ([arXiv:1209.3114](https://arxiv.org/abs/1209.3114))
- Mills B. Y., 1981, Proceedings of the Astronomical Society of Australia, 4, 156
- Mocanu L. M., et al., 2013, ApJ, 779, 61
- Mohr J., Evrard A., 1997, ApJ, 491, 38
- Mohr J. J., Evrard A. E., Fabricant D. G., Geller M. J., 1995, ApJ, 447, 8+
- Mohr J. J., Mathiesen B., Evrard A. E., 1999, ApJ, 517, 627
- Monaghan J. J., Lattanzio J. C., 1985, A&A, 149, 135
- Mortonson M. J., Hu W., Huterer D., 2011, Phys. Rev. D, 83, 023015
- Motl P. M., Hallman E. J., Burns J. O., Norman M. L., 2005, ApJ, 623, L63
- Mullis C. R., et al., 2003, ApJ, 594, 154
- Murphy T., Mauch T., Green A., Hunstead R. W., Piestrzynska B., Kels A. P., Sztajer P., 2007, MNRAS, 382, 382
- Nagai D., 2006, ApJ, 650, 538
- Nagai D., Kravtsov A. V., Vikhlinin A., 2007, ApJ, 668, 1
- Navarro J. F., Frenk C. S., White S. D. M., 1997, ApJ, 490, 493
- Nelson K., Lau E. T., Nagai D., 2014, ApJ, 792, 25
- Nurgaliev D., et al., 2016, preprint, ([arXiv:1609.00375](https://arxiv.org/abs/1609.00375))
- Ostriker J. P., Vietri M., 1990, Nature, 344, 45
- Perlman E. S., Horner D. J., Jones L. R., Scharf C. A., Ebeling H., Wegner G., Malkan M., 2002, ApJS, 140, 265
- Pfrommer C., 2008, MNRAS, 385, 1242
- Piffaretti R., Arnaud M., Pratt G. W., Pointecouteau E., Melin J.-B., 2011, A&A, 534, A109

- Plagge T., et al., 2010, ApJ, 716, 1118
- Planck Collaboration 2011, A&A, 536, A10
- Planck Collaboration et al., 2011, A&A, 536, A13
- Planck Collaboration et al., 2013b, preprint, (arXiv:1303.5080)
- Planck Collaboration et al., 2013a, preprint, (arXiv:1303.5089)
- Planck Collaboration et al., 2013c, A&A, 550, A131
- Planck Collaboration et al., 2013d, A&A, 557, A52
- Planck Collaboration et al., 2015b, preprint, (arXiv:1502.01589)
- Planck Collaboration et al., 2015a, preprint, (arXiv:1502.01597)
- Planck Collaboration et al., 2016a, A&A, 594, A15
- Planck Collaboration et al., 2016b, A&A, 594, A24
- Planck Collaboration et al., 2016c, A&A, 594, A27
- Pracy M., et al., 2016, preprint, (arXiv:1604.04332)
- Predehl P., et al., 2014, in Space Telescopes and Instrumentation 2014: Ultraviolet to Gamma Ray. p. 91441T, doi:10.1117/12.2055426
- Rasia E., Tormen G., Moscardini L., 2004, MNRAS, 351, 237
- Rasia E., et al., 2006, MNRAS, 369, 2013
- Rasia E., et al., 2012, New Journal of Physics, 14, 055018
- Reichardt C. L., et al., 2013, ApJ, 763, 127
- Rephaeli Y., 1995, ARA&A, 33, 541
- Robertson J. G., 1991, Australian Journal of Physics, 44, 729
- Romer K., Viana P. T. P., Liddle A. R., Mann R. G., 2000, in Large Scale Structure in the X-ray Universe, Proceedings of the 20-22 September 1999 Workshop, Santorini, Greece, eds. Plionis, M. & Georgantopoulos, I., Atlantis Sciences, Paris, France, p.409. p. 409, [http://adsabs.harvard.edu/cgi-bin/nph-bib\\_query?bibcode=2000lssx.proc..409R&db\\_key=AST](http://adsabs.harvard.edu/cgi-bin/nph-bib_query?bibcode=2000lssx.proc..409R&db_key=AST)
- Rozo E., Rykoff E. S., 2014a, ApJ, 783, 80
- Rozo E., Rykoff E. S., 2014b, ApJ, 783, 80

- Rozo E., et al., 2010, *ApJ*, 708, 645
- Rozo E., Rykoff E. S., Bartlett J. G., Evrard A., 2014a, *MNRAS*, 438, 49
- Rozo E., Evrard A. E., Rykoff E. S., Bartlett J. G., 2014b, *MNRAS*, 438, 62
- Rykoff E. S., et al., 2012, *ApJ*, 746, 178
- Rykoff E. S., et al., 2014, *ApJ*, 785, 104
- Rykoff E. S., et al., 2016, *ApJS*, 224, 1
- Rykoff et al. in prep., preprint ([arXiv:9999.9999](https://arxiv.org/abs/9999.9999))
- Sanderson A. J. R., Edge A. C., Smith G. P., 2009, *MNRAS*, 398, 1698
- Santos M. G., et al., 2017, preprint, ([arXiv:1709.06099](https://arxiv.org/abs/1709.06099))
- Saro A., et al., 2014, *MNRAS*, 440, 2610
- Saro A., et al., 2015, *MNRAS*, 454, 2305
- Saro A., et al., 2017, *MNRAS*, 468, 3347
- Sayers J., et al., 2016, *ApJ*, 832, 26
- Schaffer K. K., et al., 2011, *ApJ*, 743, 90
- Schaye J., et al., 2010, *MNRAS*, 402, 1536
- Schechter P., 1976, *ApJ*, 203, 297
- Schrabback T., et al., 2016, preprint, ([arXiv:1611.03866](https://arxiv.org/abs/1611.03866))
- Sehgal N., Bode P., Das S., Hernandez-Monteagudo C., Huffenberger K., Lin Y., Ostriker J. P., Trac H., 2010, *ApJ*, 709, 920
- Sehgal N., et al., 2011, *ApJ*, 732, 44
- Sehgal N., et al., 2013, *ApJ*, 767, 38
- Shaw L. D., Holder G. P., Bode P., 2008, *ApJ*, 686, 206
- Shi X., Komatsu E., 2014, *MNRAS*, 442, 521
- Shi X., Komatsu E., Nelson K., Nagai D., 2015, *MNRAS*, 448, 1020
- Short C. J., Thomas P. A., 2009, *ApJ*, 704, 915
- Sijacki D., Pfrommer C., Springel V., Enßlin T. A., 2008, *MNRAS*, 387, 1403

- Soergel B., et al., 2016, MNRAS, 461, 3172
- Sommer M. W., Basu K., Pacaud F., Bertoldi F., Andernach H., 2011, A&A, 529, A124
- Song J., et al., 2012, ApJ, 761, 22
- Springel V., 2005, MNRAS, 364, 1105
- Springel V., Hernquist L., 2002, MNRAS, 333, 649
- Springel V., Hernquist L., 2003, MNRAS, 339, 289
- Springel V., White S. D. M., Tormen G., Kauffmann G., 2001, MNRAS, 328, 726
- Staniszewski Z., et al., 2009, ApJ, 701, 32
- Stoeckel J. T., Perlman E. S., Gioia I. M., Harvanek M., 1999, AJ, 117, 1967
- Stott J. P., et al., 2012, MNRAS, 422, 2213
- Strazzullo V., Pannella M., Owen F. N., Bender R., Morrison G. E., Wang W.-H., Shupe D. L., 2010, ApJ, 714, 1305
- Sun M., Sehgal N., Voit G. M., Donahue M., Jones C., Forman W., Vikhlinin A., Sarazin C., 2011, ApJ, 727, L49+
- Sunyaev R. A., Zel'dovich Y. B., 1970, Comments on Astrophysics and Space Physics, 2, 66
- Sunyaev R. A., Zel'dovich Y. B., 1972, Comments on Astrophysics and Space Physics, 4, 173
- Tegmark M., de Oliveira-Costa A., 1998, ApJ, 500, L83
- Teklu A. F., Remus R.-S., Dolag K., Beck A. M., Burkert A., Schmidt A. S., Schulze F., Steinborn L. K., 2015, ApJ, 812, 29
- Tescari E., Viel M., Tornatore L., Borgani S., 2009, MNRAS, 397, 411
- The Planck Collaboration 2006, ArXiv:astro-ph/0604069,
- Tinker J., Kravtsov A. V., Klypin A., Abazajian K., Warren M., Yepes G., Gottlöber S., Holz D. E., 2008, ApJ, 688, 709
- Tornatore L., Borgani S., Springel V., Matteucci F., Menci N., Murante G., 2003, MNRAS, 342, 1025
- Tornatore L., Ferrara A., Schneider R., 2007a, MNRAS, 382, 945
- Tornatore L., Borgani S., Dolag K., Matteucci F., 2007b, MNRAS, 382, 1050

- 
- Tucci M., Toffolatti L., de Zotti G., Martínez-González E., 2011, *A&A*, 533, A57
- Vanderlinde K., et al., 2010, *ApJ*, 722, 1180
- Vieira J. D., et al., 2010, *ApJ*, 719, 763
- Vikhlinin A., et al., 2009, *ApJ*, 692, 1033
- White M., Hernquist L., Springel V., 2002, *ApJ*, 579, 16
- Wiersma R. P. C., Schaye J., Smith B. D., 2009, *MNRAS*, 393, 99
- de Haan T., et al., 2016, preprint, ([arXiv:1603.06522](https://arxiv.org/abs/1603.06522))
- de Zotti G., Ricci R., Mesa D., Silva L., Mazzotta P., Toffolatti L., González-Nuevo J., 2005, *A&A*, 431, 893
- von der Linden A., et al., 2014a, *MNRAS*, 439, 2
- von der Linden A., et al., 2014b, *MNRAS*, 443, 1973

# Acknowledgments

I would like to thank my supervisor Joe Mohr for giving me this opportunity to start my research career in the most comfortable environment. I thank you for your patience and invaluable guidance throughout these years. Everytime I meet you, I learn something new and exciting. Your trust in me always motivated me to try new things and your suggestions in innumerable matters is the reason behind my success today. Thanks a-lot for everything!

I would also like to thank my colleagues and group members: Jiayi, Sebastian B., Christina, Corvin, Klaus, Matthias, Veronika, Maurilio, Joerg, Shantanu, Martin, Holger, David, Xingjian, Steffen, Georgia, Tea, Matteo, Ben, Kerstin, Luiz, Antonio, most amazing I-Non, majestic Raffaella, creative Sebastian G., visionary Thomas and thoughtful Maria. It was a pleasure to work with you. Thank you for all the discussions, laughters, lunch talks, coffee-coffee talks, movie nights, dinners, barbeques and amazing travel times. Special thanks to Alex (the Rocco Cinghiale) for being a big brother in this journey. It was amazing to work with you and thanks for all those after-work amazing times in Munich.

I would like to thank Uta for helping me out in numerous administrative and personal necessities, thanks a-lot for being so kind to me. I would also like to thank my Master thesis supervisor Cristiano for introducing me to this amazing research field of Cosmology. It's because of you that I gained interest in this field and I could achieve this milestone. Thanks a-lot for your help in all professional as well as critical personal problems.

I would like to extend my gratitude to all my friends in India and in Germany for all those wonderful times (can't write all names but you know that I'm talking about you). It was impossible to achieve this milestone without your love and support. My special thanks to wonderful Helen for doing nothing (as she says) but everything (as I say) to help me finish my doctoral studies.

Finally, I would like to thank my sister Ruhi, my cousins, brother in-law Gaurav and my grandmother for supporting me in every possible way and special thanks to my mother Savita and father Ravinder for all their sacrifices, endless love and blessings.